UNIVERSITY OF CALIFORNIA
RIVERSIDE

Mathematical and Experimental Studies of Pollen Tube Tip Growth and Guidance

A Dissertation submitted in partial satisfaction
of the requirements for the degree of

Doctor of Philosophy

in

Plant Biology

by

Nan Luo

March 2016

Dissertation Committee:
Dr. Zhenbiao Yang, Chairperson
Dr. Guanshui Xu
Dr. Venugopala Reddy Gonehal

The Dissertation of Nan Luo is approved:

_____

_____

_____

Committee Chairperson

University of California, Riverside

ACKNOWLEDGEMENTS

First of all, I would like to thank my advisor, Dr. Zhenbiao Yang, from whom I learnt so much. He is a brilliant scientist and a gracious mentor. Without his constant guidance, support and encouragement, this work would not have been possible. I am also deeply grateful to Dr. Guanshui Xu, who taught and helped me so much with great patience. I would also like to thank Dr. Venugopala Reddy Gonehal for his constructive advice and kind help. My gratitude also goes to the members of my Qualifying Exam Committee, Dr. Xuemei Chen, Dr. Natasha Raikhel, and Dr. Julia Bailey-Serres for their guidance and critical advice.

I wish to thank all the members of the Yang lab for their help and support and for all the great time we spent together that will be missed. My special thanks go to An Yan for teaching and training me, for giving me directions and inspiration at the beginning of my PhD study. I would also like to thank Gang Liu and Shingo Nagawa for sharing their knowledge and expertise, for helping me with difficulties in my research. I would like to thank Augusta Jamin, Ornusa Khamsuk, Deshu Lin, Jisheng Chen, Jinghua Shi, Irene Lavagi, Christian Craddock, Hui Li, Geoffrey Harlow, Tiantian Zhu, Duoyan Rong, Fei Wang, and Jingzhe Guo for their friendship, for the great discussions and for their constant help.

I have also got a lot of help from people outside the Yang lab. I thank Dr. Xinping Cui and Zhen Xiao for the fruitful collaboration in the modeling of ROP polarization and oscillation.

I thank Asong Tambo for developing tools for analyzing confocal images of pollen tubes. I also thank Dr. David Carter for providing training and assistance in confocal microscopy. I wish to thank the entire Department of Botany and Plant Sciences and the Institute for Integrative Genome Biology (IIGB) at UC Riverside for providing a most pleasant and inspiring academic environment.

Finally, my deepest gratitude goes to my parents and my husband for being there, for caring, for their patience and love that supported me throughout these years.

ABSTRACT OF THE DISSERTATION

Mathematical and Experimental Studies of Pollen Tube Tip Growth and Guidance

by

Nan Luo

Doctor of Philosophy, Graduate Program in Plant Biology
University of California, Riverside, March 2016
Dr. Zhenbiao Yang, Chairperson

Tip growth is an extreme form of polar growth and involves highly polarized cellular activities, such as vesicular trafficking and cell surface extension. In the presence of environmental signals, tip-growing cells are able to reestablish the axis of polarity and growth in a process called growth guidance. Previous studies show that in various cell systems, tip growth and growth guidance depend on polarized Rho GTPase signaling and exocytosis. In this study, we combined mathematical modeling and biological experimentation to study the molecular mechanisms underlying the tip growth and guidance of *Arabidopsis* pollen tubes. Firstly, a mathematical model integrating the intracellular signaling and the cell surface mechanics in pollen tube tip growth is presented. The predictions of the model were confirmed by phenotypic characterization of mutants defective in the ROP1 signaling, exocytosis or cell wall modification. The results supported the hypothesis that in pollen tube tip growth, exocytosis is the central player that couples ROP1 GTPase signaling pathways with cell wall mechanical properties. Secondly, a

mathematical model of pollen tube guidance was developed based on the framework of the tip growth model using the Finite Element Method. In this model, the distribution of active ROP1 is biased by the gradient of the extracellular guidance signal, leading to asymmetric growth towards the source of the guidance signal. This model is validated by observing the dynamics of ROP1 activity and cell morphology in pollen tube guidance using the semi-*in vitro* assay. Finally, a novel method of measuring the exocytosis rate of cell membrane or cell wall proteins is presented. In this method, the protein-of-interest is tagged with Dendra2, a photo-convertible fluorescent protein. Following photoconversion, both exocytosis and other processes that affect fluorescence recovery such as endocytosis and cell surface extension can be tracked simultaneously. We developed an algorithm for data processing and calculation, and applied this method to measuring the exocytosis rate of PRK1 in *Arabidopsis* pollen tubes. Overall, this study provided a platform for the application of mathematics in the study of plant cell signaling and morphogenesis.

Table of Contents

List of Figures

List of Tables

Introduction

Tip growth is an extreme form of polarized growth found across eukaryotic kingdoms, and is involved in various physiological processes, such as nutrient uptake and host invasion (Cole and Fowler, 2006; Lee and Yang, 2008). Pollen tubes of angiosperms are able to travel a long distance to deliver sperm cells to ovules by extensive tip growth and highly efficient growth guidance. During these processes, a wide range of cellular activities including Rho GTPase signaling, cytoskeleton dynamics, vesicular trafficking and mechanical changes in cell wall are coupled together and form a tightly coordinated network to sustain rapid and robust tip growth while remaining highly responsive to extracellular guidance cues.

ROP1 signaling in pollen tubes

In pollen tubes, the dynamics of the actin filaments and the polarized exocytosis are controlled by an intricate signaling network at its apex. The molecular switches ROP GTPases (Rho-related GTPase of plants) are the key players in this network (ROP1, 3 and 5 function redundantly in pollen tubes and will be hitherto referred to as ROP1). Rho GTPases are highly conserved signaling proteins found in all eukaryotic organisms. They are often called molecular switches since they can switch between a GDP-bound inactive state and a GTP-bound active state. In the active state, they bind with various downstream effectors that generally participate in cytoskeleton and trafficking based processes.

In pollen tubes, active ROP1 is distributed on the plasma membrane (PM) of the cell apex (Lin et al., 1996). This polar distribution is maintained by two opposing types of upstream regulation: ROP1 is activated locally at the tip by the guanine nucleotide exchange factors (GEFs) (Gu et al., 2006), and is deactivated by GTPase-activating proteins (GAPs) in a global manner to prevent its invasion to the shank (Hwang et al., 2008).

The active ROP1 at the tip of pollen tubes regulates the apical filamentous actin (F-actin) network through its activation of RIC4 and RIC3, which are two members of the RIC (ROP-interactive CRIB motif-containing proteins) family, a family of plant specific Rho effectors (Wu et al., 2001). RIC4 promotes the assembly of apical F-actin while RIC3 promotes the disassembly of this F-actin through Ca^{2+} signaling (Gu et al., 2005). The check and balance between these two pathways results in the oscillation of actin between polymerized and de-polymerized forms (Fu et al., 2001). RIC4-mediated polymerization of F-actin is required for the exocytic vesicles to be delivered to the tip, and RIC3-mediated de-polymerization of F-actin leads to the fusion of vesicles with the PM and releasing of the cargos (Lee et al., 2008). As a result, active ROP1 maintains a highly polarized pattern of exocytosis at the apex of pollen tubes.

Exocytosis in pollen tubes

Polarized exocytosis delivers newly synthesized cell wall materials and cell wall modifying enzymes to the tip and thereby is expected to link ROP signaling to the mechanical properties of the cell wall (McKenna et al., 2009; Rojas et al., 2011). Exocytosis has also

been shown to be involved in the regulation of ROP1 activity by delivering the regulators of ROP1 to the apical PM. Receptor-like kinases and their secreted peptide ligands are expected to be targeted to the PM by exocytosis (Huang et al., 2014; Chang et al., 2012; Zhang and McCormick, 2007; Tang et al., 2004). It is proposed that through the ROP1 activator RopGEFs, ROP1 is locally activated by tip-localized receptor-like kinases (Chang et al., 2012; Zhang and McCormick, 2007). On the other hand, exocytosis is required for the targeting of the major RhoGAP in pollen tubes, REN1, to the apical PM (Hwang et al., 2008). In Chapter 1, we developed and tested a model in which exocytosis couples ROP1 signaling to the mechanics of the cell wall.

Exocytosis is highly dynamic in tip-growing cells. The accurate measurement of exocytosis rate is critical to understanding how it is regulated temporally and spatially and how it affects the localization and function of the cargo molecules. A variety of methods have been developed to monitor or measure exocytosis (Keighron et al., 2012; Allersma et al., 2004; Willig et al., 2006; Betz and Bewick, 1992; Zonia and Munnik, 2008). However, many of these methods require specialized equipment, and the results obtained are often interfered by exocytosis-independent trafficking processes such as endocytosis. In Chapter 2, we presented an optical method performed on a regular laser scanning microscope to measure exocytosis-dependent and independent trafficking events simultaneously and accurately determine exocytosis rate.

Cell wall mechanics of pollen tubes

The expansion of the cell wall of pollen tubes is driven by turgor pressure, which is maintained by intricate regulation of water and ion fluxes at a nearly constant level during the growth of pollen tubes (Benkert et al., 1997). The deformation of the cell wall under the turgor pressure is determined by its mechanical properties, which is mainly contributed by the major components of pollen tube cell wall, the pectin polymers (Parre and Geitmann, 2005; Jiang et al., 2005; Bosch and Hepler, 2005; Fayant et al., 2010). Newly synthesized pectin is methylated and has fewer crosslinks, and thus are more extensible (Willats, 2001). This "soft" form of pectin is de-esterified by pectin methylesterases (PMEs) in the cell wall (Rockel et al., 2008; Bosch et al., 2005), and the demethylated pectin form crosslinks through Ca^{2+} bridges and becomes structurally rigid (Willats, 2001). PME is inactivated by PME inhibitors (PMEIs), which are distributed exclusively at the apex of pollen tubes (Rockel et al., 2008). The distribution of these two types of pectins determines the mechanical properties of the pollen tube cell wall.

The application of mathematical modeling in studying cell tip growth and guidance

The application of mathematical modeling to biological research is still a developing field, but offers great potential for the understanding of complex biological systems with its power of quantification. In the study of cell tip growth and guidance, various components and pathways intertwined with each other, making predictions of the system under different conditions by intuition very difficult. Mathematical models not only can explain complex experimental data, but also allow us to develop new theories and design new experiments

by making predictions from “virtual experiments”. If the model is able to predict experimental observations, our hypotheses are supported. It is equally useful when the model does not initially support the hypothesis since it gives us clues to revise our theory.

Chapter 1 Exocytosis Couples Cell Polarity Signaling With Wall Mechanics in the Control of Pollen Tube Tip Growth

Abstract

As an extreme form of polar cell growth, tip growth efficiently generates highly elongated cells for long-distance targeting, nutrient foraging or host invasion. Rapid tip growth invariably requires robust exocytosis and polarized Rho-family GTPase signaling, both occurring at the dome-shaped cell apex. Rapid tip growth in walled cells also requires turgor pressure, suggesting a tight spatiotemporal control of the cell wall mechanics in this process. However, how these subcellular processes are coordinated is unknown. Combined modeling and experiments demonstrate that exocytosis is at the core of the circuitry linking the polar activation of the ROP1 Rho GTPase to the deformation of the cell wall during the tip growth of *Arabidopsis* pollen tubes. Through exocytosis-based positive and negative feedbacks and lateral diffusion, active ROP1 is distributed as a polar apical dome in the plasma membrane of pollen tubes. ROP1-dependent exocytosis delivers to the apex the deformable methylated pectic wall materials and pectin methylesterase converts them to less deformable demethylated pectin, which is displaced to the shank behind the growing apical dome. Thus exocytosis generates the mechanical properties of cell wall necessary for tip growth as well as the maintenance of the pollen tube shape. Experimental perturbations of the key factors in this system alter the shape of pollen tubes as predicted by modeling, revealing the requirement for exocytosis-based tight coupling between intracellular signaling and mechanical changes in the cell wall during tip growth.

Introduction

Fast tip growth is found in various cell types, which have evolved diverse physiological functions in reproduction and growth. For example, root hairs of plants and hyphae of filamentous fungi maximize the effective area for nutrient and water uptake by fast tip growth. Human and plant pathogen are able to transform from spores or yeast forms to tip-growing hyphae for effective host invasion (Nett and Andes, 2006; Giraldo and Valent, 2013). In response to female guidance cues, pollen tubes elongate rapidly and directionally to deliver sperms to the ovules for double fertilization during sexual reproduction in higher plants. Cultured pollen tubes in the absence of directional cues grow uni-directionally much like fungal hyphae (Fan et al., 2001; Li et al., 1999), and serve as an excellent model system for the investigation of mechanisms behind rapid tip growth (Yang, 2008; Qin and Yang, 2011; Cheung and Wu, 2008; Hepler et al., 2013). Despite of the differences in physiological functions, mechanisms underlying the fast tip growth share several common essential properties: localized distribution of Rho-family GTPases in the plasma membrane (PM) as an apical cap, polarized exocytosis to the apical cap region and polarized distribution of the cell wall materials so that the apical wall is expandable under turgor pressure while the basal wall is not (Lee et al., 2008; Qin and Yang, 2011; Guan et al., 2013; Riquelme, 2013; Mendrinna and Persson, 2015). In rapidly tip-growing cells, these polarized activities are tightly correlated both spatially and temporally (McKenna et al., 2009; Bou and Geitmann, 2011; Hwang et al., 2005), but the mechanisms behind the coordination remain largely unknown. In particular, how intracellular regulation and organization coordinates with the differential cell wall mechanics is a “black box”.

Several computational models have been built to simulate the cell wall mechanical properties required for the morphogenesis of tip-growing cells (Kroeger and Geitmann, 2012; Kroeger and Geitmann, 2012). These models revealed that the observed geometry of a tip-growing cell requires a polarized pattern of cell wall mechanical properties, which is related to intracellular chemical kinetics and the deposition of new wall materials via exocytosis (Kroeger et al., 2008; Fayant et al., 2010; Dumais et al., 2006). A recent study shows that the distribution pattern of exocytic machinery and the cell wall mechanics reliably predict the cell shape of slow-growing fission yeast, but the underlying mechanism is unresolved (Abenza et al., 2015). Our previous studies show that polarized exocytosis in pollen tubes is controlled by the signaling network of active ROP1 Rho GTPase, which is distributed as an apical cap in the PM (Gu et al., 2005; Lee et al., 2008). On one hand, robust exocytosis targeted to the predetermined apical surface of tip-growing cells provides nascent cell wall materials that alter the cell wall mechanics, allowing the yielding of the apical wall to turgor pressure, while the subapical wall maintains the stiffness needed to counteract the pressure (Lee et al., 2008; McKenna et al., 2009). On the other hand, the rapid insertion of nascent membrane by vesicle trafficking would displace the molecular machinery that defines the cell apex (Layton et al., 2011). Previous models of pollen tube growth has only addressed the function of exocytosis in the deposition of the structural components of the cell wall (Kroeger et al., 2008; Fayant et al., 2010; Campas and Mahadevan, 2009; Rojas et al., 2011; Hill et al., 2012), but what is the significance of these paradoxical roles for exocytosis and how the tip-growing cells resolve these paradoxes remain enigmatic. In our current study using combined computational and experimental

approaches, we have uncovered a unifying exocytosis-centered design principle that integrates the intracellular signaling and the cell wall deformation during rapid tip growth.

Results

Modeling the exocytosis-centered coupling of polarity signaling with wall mechanics

Here we propose a conceptual model for the control of rapid tip growth: Exocytosis controls the shape formation and polar growth of rapidly tip-growing cells by coupling intracellular signaling with extracellular cell wall mechanics, as depicted in Figure 1-1. We hypothesize that the self-organizing generation and maintenance of the active ROP1 apical cap is achieved by positive and negative feedback loops interlinked by ROP1-dedpendent exocytosis, which further controls cell wall mechanics to allow rapid tip growth. To theoretically investigate this hypothesis we formulate a two-module mathematical model.

The first module, the Exocytosis-ROP1 Polarization Module, describes the generation and maintenance of polarized ROP1 activity and exocytosis at the pollen tube apex. Since exocytosis is locally activated by active ROP1 (Lee et al., 2008), the rate of exocytosis along the cell periphery, $E(s,t)$, as a function of position (s) and time (t), is determined by the concentration of active ROP1, $R(s,t)$:

$$E = k_E R^{\alpha}$$

where k_E is a constant linking ROP1 activity to the local rate of exocytosis and α represents the degree of nonlinearity. Active ROP1 distribution is described by

$$\frac{\partial R}{\partial t} = k_a R_{in}\left(1 - \frac{R}{R_{max}}\right) - k_d R + D\frac{\partial^2 R}{\partial s^2}$$

where the spatiotemporal dynamics of active ROP1 is determined by three processes: ROP1 activation, deactivation and diffusion. Slow lateral diffusion in the PM is an intrinsic property of ROP1 itself as a PM-associated protein. The amount of activated ROP1 per unit time is proportional to the amount of inactive ROP1 (R_{in}), the rate of ROP1 activation (k_a), and saturated by the local highest ROP1 possible (R_{max}); while the reduction of active ROP1 per unit time is determined by the concentration of active ROP1 and the ROP1 deactivation rate (k_d). The inactive form of ROP1 (R_{in}) is maintained as a cytosolic pool by RhoGDIs (Klahre et al., 2006; Cherfils and Zeghouf, 2013), thus is expressed as a term independent of the membrane location:

$$R_{in} = R_{total} - \int R\, ds$$

k_a and k_d represents the concentration of ROP1 activators and deactivators in the PM. If they are constants, or in other words, the activators and deactivators are evenly distributed independent of exocytosis, we find this model is not able to generate polarized ROP1 distribution (Figure 1-2A).

Based on previous reports, we propose that ROP1-dependent exocytosis regulates both the activation and the deactivation of ROP1, forming feedback loops. The apical cap of the active ROP1 promotes tip-targeted exocytosis via at least two counteracting pathways and subsequent dynamics of the apical actin microfilaments (F-actin) (Gu et al., 2005; Lee et al., 2008). In yeast, both exocytosis-dependent and independent feed-forward mechanisms

have been proposed to generate the polarization of Cdc42 (Kozubowski et al., 2008; Woods et al., 2015; Wedlich-Soldner et al., 2003). In pollen tubes, the tip-localized F-actin is required for polar exocytosis, which may positively regulate ROP1 activity (Lee et al., 2008; Yan et al., 2009). Polar exocytosis is anticipated to target receptor-like kinases (such as PRK2) (Chang et al., 2012; Zhang and McCormick, 2007) and their secreted peptide ligands (Huang et al., 2014; Tang et al., 2004) to the tip. The PM-localized receptor-like kinases directly interact with the ROP1 activator RopGEFs to activate ROP1 (Chang et al., 2012; Zhang and McCormick, 2007). We hypothesize that this feed-forward activation of ROP1 together with the lateral diffusion in the apical PM generates the apical cap of the active ROP1 by lateral amplification. Therefore, the rate of ROP1 activation, k_a, is not homogeneous along the cell periphery, and its local value is proportional to the rate of exocytosis, $E(s,t)$:

$$k_a = k_{pf}E$$

where k_{pf} reflects the strength of the positive feedback.

On the other hand, ROP1-mediated polar exocytosis is required for the targeting of the REN1 RhoGAP to the apical PM, which inactivates ROP1 and limits the lateral amplification of the active ROP1 to the apical cap (Hwang et al., 2008). This exocytosis-based feed-forward and negative feedback regulations of the apical ROP1 presumably allows the establishment and maintenance of polarized ROP1 signaling and exocytosis. Two modes of negative feedback are possible: global inhibition and local inhibition. In

local inhibition, the local concentration or activity of the deactivators of ROP1 is determined by the local exocytosis rate:

$$k_d = k_{nf}E$$

While in global inhibition, the concentration or the activity of the deactivators is homogenous along the PM (Levchenko and Iglesias, 2002; Skupsky et al., 2005), possibly due to their rapid lateral diffusion or diffusive cytosolic mediators of the negative feedback pathway such as calcium ion (Yan et al., 2009). Therefore, the rate of ROP deactivation is a constant, which is proportional to the overall level of exocytosis:

$$k_d = k_{nf}k_E$$

Similarly, k_{nf} is the strength of the negative feedback. Computer simulation shows that only global inhibition, but not local inhibition, is able to generate the tip-localized ROP1 distribution (Figure 1-2B, C), agreeing with the diffusive distribution of REN1 RhoGAP in the tip of pollen tubes (Hwang et al., 2008).

In the second module (Cell Wall Extension Module) of our model, we hypothesize that the tip surface extension is linked to ROP1 signaling through ROP1-dependent exocytosis. The mechanical properties of pollen tube cell wall at the growing tip are mainly determined by its major component, pectin (Parre and Geitmann, 2005; Jiang et al., 2005; Bosch and Hepler, 2005; Fayant et al., 2010). Pectin polymers in the methylated ester form are synthesized in the Golgi body, secreted and inserted into the existing apical wall structure via exocytosis of vesicles carrying these polymers (McKenna et al., 2009; Sterling et al., 2001). These newly secreted pectins lack cross-linking by calcium bridges and thus are

"soft" and extensible (Willats, 2001). However, exocytosis also secretes pectin methylesterases (PMEs) into the apical cell wall, which de-esterify methylated pectin molecules (Rockel et al., 2008; Bosch et al., 2005). The demethylated pectin polymers form crosslinks through Ca^{2+} bridges and become structurally rigid, and thus are considered as "hard" pectin (Willats, 2001). Accordingly, the distribution of these two forms of pectins in the cell wall (P_s, soft pectin and P_h, hard pectin) is described by

$$\frac{\partial P_s}{\partial t} = k_{sec}E - k_{pme}P_s - \frac{\partial (v_s P_s)}{\partial s}$$

and

$$\frac{\partial P_h}{\partial t} = k_{pme}P_s - \frac{\partial (v_s P_h)}{\partial s}$$

which include the secretion of soft pectin, the conversion of soft pectin to hard pectin by PMEs and the displacement of pectins due to cell growth (here v_s is the local tangent growth velocity of the cell wall).

Pollen tube growth and shape formation is the result of turgor pressure-driven cell wall deformation, which has been simulated using the viscoplasticity theory (Dumais et al., 2006; Lockhart, 1965). The rate of deformation, or the strain rate ($\dot{\varepsilon}$), of a viscoplastic material under stress (σ) is proportional to the extensibility of the material (Φ):

$$\dot{\varepsilon} = \Phi(\sigma - \sigma_y)$$

where σ_y is the yield stress. For simplification, the extensibility of the cell wall, $\Phi(s,t)$, in our model is proportional to the local concentration of soft pectin. We use the equations previously established by Dumais and Shaw et al., 2006 to calculate the stresses, strain

rates and the cell geometry. An algorithm for solving these equations numerically was developed with the MatLab (The MathWorks) software.

Measurements and estimation of parameters

We sought to construct a realistic and robust model that not only will be applicable to a wide range of walled tip-growing cells, but also can accurately simulate the tip growth behavior for pollen tubes from a particular species. Such models will have a robust predictive power for further mechanistic understanding of the system (Mogilner et al., 2012). This requires accurate measurement of key parameters and selection of other parameters that fit our data and allow robust predictions.

We first determined parameters in the Exocytosis-ROP1 Polarization Module. We experimentally determined the rate constant of ROP1 lateral diffusion in the PM (D) using Fluorescence Recovery After Photo-bleaching (FRAP) analysis (Marco et al., 2007) in *Arabidopsis* pollen tubes expressing GFP-ROP1 (Figure 1-3A). We suppressed F-actin-dependent exocytosis in pollen tubes by F-actin polymerization inhibitor Latrunculin B (LatB) and photo-bleached a small region of the apical PM. Using the distribution curves of GFP-ROP1, we estimated the diffusion constant of GFP-ROP1 on the apical PM of pollen tubes to be 0.2 ± 0.05 $\mu m^2/s$ (n = 5, Ave ± SD, Figure 1-3B).

Other parameters of the Exocytosis-ROP1 Polarization Module are difficult to measure experimentally, and we estimated them firstly by trial-and-error method: repeated

simulation with different combinations of parameters until the predicted distribution of ROP1 is close enough to the measurement. Since this simple method is inefficient and does not provide the optimal solution of the entire parameter space, we developed a statistical algorithm to estimate the two key parameters in this module: the strength of the positive and the negative feedback loops, k_{pf} and k_{nf}. From the parameter space, this algorithm efficiently screens for the set of parameters with which the simulation of active ROP1 distribution fits best with the experimental data. To experimentally quantify ROP1 activity at the apical PM of *Arabidopsis* pollen tubes, we used GFP-tagged CRIB motif of RIC4 (CRIB4-GFP) as an active ROP1 marker. RIC4 is an effector of ROP1 and binds preferentially with the active form of ROP1 by the CRIB (Cdc42/Rac-interactive binding) motif (Wu et al., 2001; Gu et al., 2005). Previously, we used the PM distribution of GFP-RIC4ΔC, which lacks the C terminal domain for its effector function but retains the capability to bind with active ROP1, to report ROP1 activity at the tip of tobacco pollen tubes (Hwang et al., 2005). However, GFP-RIC4ΔC exhibited very weak PM distribution in *Arabidopsis* pollen tubes, possibly due to additional regulations on the other domains of the protein. We found that the RIC4 CRIB domain alone exhibited identical distribution to that of GFP-RIC4ΔC in tobacco pollen tubes but has much stronger PM signal in *Arabidopsis* pollen tubes, displaying a cap-like distribution with the peak value at the cell apex (Figure 1-4A, Figure 1-5A). FRET (Förster Resonance Energy Transfer) analysis shows that CRIB4-GFP also specifically interacts with active ROP1 (Figure 1-4B) and the expression of CRIB4-GFP in *Arabidopsis* does not induce pollen tube depolarization (Figure 1-4C). Based on the distribution curves of CRIB4-GFP in 32 *Arabidopsis* pollen

tubes, we obtained the best-fitting k_{pf} and k_{nf} which enable the model to accurately reproduce the distribution pattern of active ROP1 in wild-type pollen tubes of *Arabidopsis* (Figure 1-5B).

Parameters in the Cell Wall Extension Module are either adopted from literature or estimated by trial-and-error method to fit simulations of the distribution of pectins and the cell shape of wild-type *Arabidopsis* pollen tubes with experimental data. The soft and hard pectins are immunostained using JIM7 and JIM5 antibodies (Knox et al., 1990; Vandenbosch et al., 1989). The JIM7-stained soft pectin preferentially localizes to the growing pollen tube apex, while the JIM5-stained hard pectin displays a complementary pattern, primarily distributed to the shank of pollen tubes and nearly absent from the growing apex (Figure 1-5C), consistent with previous reports (Bosch and Hepler, 2005; Fayant et al., 2010; Dardelle et al., 2010). Using the estimated parameters, the simulation of pectin distribution and cell shape matches well with observations (Figure 1-5D, E).

Our simulation shows that our model is robust against minor fluctuations of parameters. Varying the major parameters by 5% still results in stable-growing pollen tubes with constant width (Figure 1-6A). Interestingly, varying parameters that are likely differ among different plant species generates tip-growing pollen tubes with various widths. Figure 1-6B shows the width of simulated pollen tubes with different combinations of exocytosis-independent coefficients for ROP1 activation (k_{pf}) and inactivation (k_{nf}), reflecting a wide range of pollen tube widths one can find in nature, such as narrow *Arabidopsis* pollen tubes

(6.0 ± 0.2 μm) and wide tobacco and lily pollen tubes (about 9 μm and 15 μm, respectively) (Gu et al., 2005; Wilsen and Hepler, 2007).

The model explains how changes in ROP1 activation affects pollen tube growth polarity

To test the robustness of our model, we used the model with the parameters obtained based on wild-type data to predict the phenotypes of mutants by altering the corresponding parameters. We experimentally tested the robustness of our model by manipulating k_{nf}. The REN1 RhoGAP has been suggested to play a key role in the negative feedback. The model predicted that when the global inhibition of ROP1 activity is compromised (reducing the ROP1 inactivation coefficient k_{nf} to 20%), the active ROP1 cap will be greatly expanded, leading to broader distribution of soft pectin and depletion of hard pectin from a larger region of the tip. Consequently, the growth of pollen tube is depolarized (Figure 1-5D). These predictions are validated by the observations of *ren1-1,* a loss-of-function mutant of *REN1,* incubated for 2 to 3 hours (Hwang et al., 2008). The active ROP1 cap in *ren1-1* pollen tubes shown by the RIC4CRIB-GFP marker is enlarged with the average peak width at half height increased from 5.8 μm (in wild-type) to 19.6 μm. By immunostaining, we found that JIM7 stained soft pectin show much broader distribution whilst JIM5 stained hard pectin is absent from a larger region at the tip comparing to wild-type. Correspondingly, the average width of *ren1-1* pollen tubes increases to 17.5 ± 0.8 μm comparing with 6.0 ± 0.2 μm of wild-type pollen tubes at 2 hours after germination (Figure 1-5). However, when *ren1* pollen tubes are incubated for more than 3 hours, they become balloon-like and the cytoplasm becomes highly vacuolated, indicating complete

depolarization. At this stage, though the distribution of ROP1 activity does not change much, pectin distribution become almost homogenized and the width of the cell is much larger than the model's prediction. Therefore, though the model is robust for cells that maintain polar growth mode, it is not applicable to non-polar cells, as anticipated.

Exocytosis plays an important role in the modulation of growth polarity in pollen tubes

Due to the versatile roles of exocytosis in pollen tube tip growth, it is difficult to make intuitive predictions of how the system will change when exocytosis is compromised. But with the aid of the computational model, we found that different levels of exocytosis lead to distinct phenotypes. The model predicts that when exocytosis is severely reduced (k_E reduced below 44%), the active ROP1 cap is abolished. However, a moderate reduction of exocytosis results in broader distribution of active ROP1 (Figure 1-7A). Therefore, in the former case the growth of the cells will stop, while in the latter case, the soft pectin will expand and the pollen tubes will become wider (Figure 1-8).

We experimentally tested these predictions using pollen tubes show different levels of exocytosis. The rate of exocytosis in pollen tubes is measured using Corrected Fluorescence Recovery After Photo-conversion analysis (cFRAPc), which is discussed in Chapter 3. Firstly, we tested the predictions for severe reduction of exocytosis by treating pollen tubes expressing CRIB4-GFP with high concentration of LatB (50 nM). After 30min treatment with LatB, active ROP1 cap and the growth of pollen tubes are abolished (Figure 1-8A). Interestingly, LatB treated pollen tubes often show bulging tips, which is also

reproduced by the model (Figure 1-8B). According to the model, this phenotype is resulted from temporary depolarized growth caused by the residual but expanded ROP1 activity. Next, we used *sec8-4*, a weak mutant of *SEC8*, to test the predictions for moderate reduction of exocytosis. *SEC8* gene is expressed in pollen tubes and encodes a subunit of the exocyst complex, which is important for exocytosis in plant cells (Hala et al., 2008). We estimated that in *sec8-4* pollen tubes, exocytosis rate is reduced to 57% of that in wild-type (Figure 1-9). Both the active ROP1 and the pectin distribution profile agree with the simulation results very well. Consistent with the model, *sec8-4* pollen tubes show broader distribution of active ROP1 and soft pectin, and the shape of the cells are significantly wider with the width increased to $8.4 \pm 0.3\mu m$ (Figure 1-8, 1-10).

Pectin Methylesterase levels regulates the polarity of pollen tube growth

The last link in the shape control of pollen tubes is the heterogeneous extensibility of the cell wall, which is resulted from the exocytosis-mediated deposition of soft pectin to the cell apex and the conversion of soft pectin to hard pectin by PME. With the same level of exocytosis, changes in the amount of PME affect the distribution of pectins: low concentration of PME, or low pectin de-esterification rate (k_{pme}), increases the range of soft pectin at the tip and reduces the amount of hard pectin at the sub-apical region, generating wider pollen tubes (Figure 1-11B, C). To test these predictions, we performed pectin immunostaining using plant lines with various levels of VANGUARD1 (VGD1), a major PME in *Arabidopsis* pollen tubes (Jiang et al., 2005). As expected, the distribution of soft pectin in *vgd1-1* is much broader and the area absent of hard pectin at the tip is

wider comparing to wild-type. The partial complementary line of *vgd1-1*, *vgd1-1* LAT52::VGD1-GFP, shows similar but alleviated phenotypes (Figure 1-11A, B). Corresponding to the differences in pectin distribution, *vgd1-1* pollen tubes with the broadest extensible region at the tip are the widest, followed by *vgd1-1*-Com pollen tubes, and bursting of growing pollen tubes is often observed (Figure 1-11A, C).

Discussion

Among computational models of tip-growing cells, our model is the first one that combines intracellular signaling with cell surface mechanics. It captured the mechanism underlying rapid tip growth of pollen tube, namely exocytosis-based coordination of ROP1 polarization and local cell wall extension, a fundamental characteristic for rapid tip growth system. In symmetric round-like cells without rapid tip growth such as budding yeast, Rho GTPase (Cdc42) polarization can be achieved by reaction-diffusion Turing type mechanism without intensive local exocytosis (Mogilner et al., 2012; Savage et al., 2012). In the case of budding yeast, the local positive feedback via autocatalytic Cdc42 activation mediated by Bem1 can function independently of the positive feedback via Cdc42 guided exocytosis mediated by actin cytoskeleton. However, in cells undergo fast tip growth, the growing end is far away from the geometrical center of the cell, therefore, Rho GTPases, the regulators and various downstream targets of Rho GTPases, and exocytosis-mediated deposition of cell surface material need to be intricately coordinated to ensure sustained Rho GTPase polarity and tip extension. On one hand, exocytosis participates in both positive and negative regulation of ROP1 GTPase activity control, maintaining the

polarized active ROP1 cap in pollen tubes. On the other hand, ROP1-dependent exocytosis controls the mechanical properties of cell wall via targeting of new cell wall material. In conclusion, exocytosis is essential for Rho GTPase pattern formation and subsequent cell growth in the pollen tubes, a rapid tip growth system.

Other essential regulators of pollen tube tip growth could be incorporated into our current model. Firstly, GDI is a class of negative regulators for Rho GTPase activity which limits the total functional free Rho GTPase in the cytoplasmic pool (Klahre et al., 2006; Hwang et al., 2010). Secondly, calcium ion plays a key role in pollen tube growth by participating in cytoskeleton dynamics, vesicle trafficking and the crosslinking of pectin in the cell wall (Brewbaker and Kwack, 1963; Hepler and Winship, 2010; Steinhorst and Kudla, 2012). Our previous study revealed that calcium ion is also involved in the negative feedback regulations of ROP1 activity in pollen tubes (Yan et al., 2009). The roles of other important players in pollen tube growth including endocytosis, phosphoinositides and reactive oxygen species (Cheung and Wu, 2008; Heilmann and Ischebeck, 2015; Moscatelli and Idilli, 2009) are still not well understood, and further study is needed to integrate them into the current model to achieve a more comprehensive picture of pollen tube tip growth. Finally, pollen tube growth *in vivo* is precisely guided by chemical signals released from the female gametophyte (Takeuchi and Higashiyama, 2012; Okuda et al., 2009). Our model can serve as a starting platform for modeling the extracellular signal-directed tip growth during pollen tube guidance.

Given the highly conserved nature of tip growth phenomenon, our model will shed light onto a general mechanism for walled tip growth cell systems such as root hair and filamentous fungi. Similar to pollen tubes, the growing tips of root hairs and fungal hyphae display rapid cytoplasmic streaming and exocytosis, which are supported by cytoskeleton (Mendrinna and Persson, 2015; Riquelme, 2013). How the polarized exocytosis is regulated in these cells is not fully understood, but may also involve Rho GTPases (Molendijk et al., 2001; Jones et al., 2002; Brand et al., 2014). Since their cell wall composition is different from that of pollen tubes, the mechanical bases of cell morphogenesis in these systems may be distinct. In root hairs, exocytosis delivers cellulose synthases to the PM for biosynthesis of cellulose in the apical cell wall (Park et al., 2011). The orientation of newly synthesized cellulose microfibrils at the tip of root hairs is highly anisotropic, while at the shank where the secondary cell wall starts to form, they are parallel to the growth axis, providing resistance to the longitudinal stress (Akkerman et al., 2012). The major structural components of the fungal cell wall, chitin and β-glucan, are synthesized by chitin synthases and glucan synthase, which are inserted to the apical PM through exocytosis (Riquelme, 2013; Riquelme et al., 2007). The subsequent crosslinking of the polysaccharide in the mature cell wall contributes to the increased stiffness at the shank (Kopecek and Raclavsky, 1999). Other mechanisms to regulate the mechanical properties of cell wall including pH and wall modification molecules such as expansins (Cosgrove, 2005) also have to be considered in the future efforts of modeling walled cell growth.

Materials and Methods

Mathematical modeling and simulation

The model of pollen tube tip growth consists of two parts: the ROP1 and Exocytosis Polarization module and the Cell Surface Extension module.

I. ROP1 and Exocytosis Polarization

The definitions and values of the parameters in this module are listed in Table 1-1.

The dynamics of active ROP1 distribution is described by

$$\frac{\partial R}{\partial t} = k_a R_{in}\left(1 - \frac{R}{R_{max}}\right) - k_d R + D\frac{\partial^2 R}{\partial s^2}, \quad [1]$$

where R is the local concentration of active ROP1 on the PM. The three terms on the right represents the rates of ROP1 activation, deactivation and diffusion, respectively. The ROP1 activation rate is proportional to the amount of inactive ROP1, R_{in}, and

$$R_{in} = R_{total} - \int R\, ds, \quad [2]$$

while ROP1 inactivation rate is proportional to the amount of active ROP1. The term $(1 - R/R_{max})$ is a restriction of ROP1 activation by the saturation concentration of active ROP1 on the PM.

The distribution of exocytosis rate is determined by active ROP1:

$$E = k_E R^{\alpha}, \quad [3]$$

where k_E is a constant linking ROP1 activity with the local exocytosis rate, representing the intrinsic strength of the exocytic system.

The coefficients k_a and k_d are determined by the local activity of GEF and GAP, which are dependent on the exocytosis rate. In our hypothesis, the polarization of ROP1 is due to local activation and global inhibition, therefore, both k_a and k_d are proportional to the level of exocytosis, while a nonlinear term, R^{α}, is required for the local feedback loop mediated by ROP1. k_{pf} and k_{nf} are exocytosis-independent constants determined by the enzyme activity and expression levels of GEF and GAP, respectively.

$$k_a = k_{pf}E, \quad [4]$$

$$k_d = k_{nf}k_E, \quad [5]$$

II. Cell Surface Extension

The definitions and values of the parameters in this module are listed in Table 1-2.

(1) Pectin Distribution and Cell Wall Extensibility

PME is evenly distributed on the cell membrane with the concentration proportional to the level of exocytosis:

$$C_{PME} = E_t$$

On the other hand, PME is inhibited by PMEI, which is tip localized:

$$C_{PMEI} = k_{pmei}E$$

Therefore, the distribution of functional PME, or effective PME, is

$$C_{EP} = C_{PME} - C_{PMEI}$$

Soft pectin is delivered to the cell wall via exocytosis and at the same time converted to hard pectin by the effective PME; both soft and hard pectins are affected by local cell wall elongation. Therefore, the distributions of soft and hard pectins are described by

$$\frac{\partial P_s}{\partial t} = k_{sec}E - k_{pme}C_{EP}P_s - \frac{\partial(v_s P_s)}{\partial s}, \quad [6]$$

$$\frac{\partial P_h}{\partial t} = k_{pme}C_{EP}P_s - \frac{\partial(v_s P_h)}{\partial s}, \quad [7]$$

where v_s is the local tangent growth velocity of the cell wall.

To simplify the problem, the extensibility of hard pectin is considered to be 0 so that the extensibility of the cell wall is determined by the distribution of soft pectin:

$$\Phi = \Phi_s P_s^*$$

Where P_s^* is the distribution of "effective" soft pectin and

$$P_s^* = P_s - k_s P_s(s = 0)$$

(2) Cell Surface Extension

The following equations for cell surface extension are previously described by Dumais et al., 2006.

Equilibrium equations:

$$\sigma_s = \frac{P}{2\delta\kappa_\theta}, \quad [11]$$

$$\sigma_\theta = \frac{P}{2\delta\kappa_\theta}\left(2 - \frac{\kappa_s}{\kappa_\theta}\right), \quad [12]$$

Constitutive equations:

$$\dot{\varepsilon}_s = \Phi(\sigma_s - \nu\sigma_\theta), \quad [13]$$

$$\dot{\varepsilon}_\theta = \Phi(\sigma_\theta - \nu\sigma_s), \quad [14]$$

Kinetic equations:

$$\dot{\varepsilon}_s = v_n\kappa_s + \frac{\partial v_s}{\partial s}, \quad [15]$$

$$\dot{\varepsilon}_\theta = v_n \kappa_\theta + \frac{v_s \cos\varphi}{r}, \quad [16]$$

Numerical simulation of this model was performed in MatLab software.

Plant materials and plasmids

All the mutants and transgenic lines of *Arabidopsis thaliana* used are in the Columbia-0 ecotype background. The transgenic *Arabidopsis* lines were generated using the Agrobacterium-mediated floral-dip method (Clough and Bent, 1998).

ren1-1 was described in (Hwang et al., 2008) and was verified by screening with BASTA. *sec8-4* (SALK 118129) and *vgd1-1* (SALK_011816) were obtained from the SALK Institute. The genotypes of *sec8-4* and *vgd1-1* lines were verified by PCR using the following primers: *sec8-4*-F (5'-GTGGCAGTAGAAAGCACGAAG-3') and *sec8-4*-R (5'-GAACTGCTTTTGCGAGATGAC-3'); *vgd1-1*-F (5'-AACCTGCAGTTGAAGATC-ACG-3') and *vgd1-1*-R (5'-CTGATCAAGGCTTTCATGCTC-3').

The CDS of a fragment of RIC4 (AT5G16490) containing the CRIB domain (CRIB4, amino acid 64-130 of RIC4) was fused with GFP at the C terminus and subcloned into a binary vector, pCL, which was constructed by inserting the pollen tube specific LAT52 promoter into pCAMBIA1300 using SalI and XbaI restriction sites. The pCL-CRIB4-GFP construct was introduced into *Arabidopsis* wild-type, *ren1-1* and *sec8-4* background. The CDS of VGD1 was fused with GFP at the C terminus and subcloned into the pCL vector to generate the pCL-VGD1-GFP construct. pCL-VGD1-GFP was introduced into *vgd1-1*

background. The pCL-PRK1-Dendra2 construct was described in (Luo et al., 2016) and was introduced into *Arabidopsis* wild-type and *sec8-4* background. GFP-ROP1 described in (Li et al., 1999) was subcloned into pCL and introduced into *Arabidopsis* wild-type background. The CDS of SEC8 was kindly provided by Dr. John Fowler (Cole et al., 2005) and was fused with GFP at the N terminus and subcloned into pCL to make the pCL-GFP-SEC8 construct. pCL-GFP-SEC8 was introduced into *sec8-4* background for the complementation experiment.

The CRIB4 fragment was subcloned into pLat52, a vector for transient expression described in (Fu et al., 2001), to generate pLat52-CRIB4-YFP construct. The pLat52-CFP-ROP1 and the pLat52-CFP-DNrop1 constructs were obtained by replacing GFP in pLat52-GFP-ROP1 or pLat52-GFP-DNrop1 described in (Li et al., 1999) by CFP. The pLat52-mCherry-RIC4ΔC construct was generated by replacing the GFP of GFP-RIC4ΔC (Hwang et al., 2005) by mCherry. The DNA of these plasmids for transient expression was introduced into tobacco (*Nicotiana tabacum*) pollen grains by particle bombardment using a PDS-1000/He particle delivery system (Bio-Rad Laboratories) as described previously (Fu et al., 2001).

Plant and pollen tube growth conditions

Arabidopsis thaliana plants were grown at 22°C in growth rooms under a light regime of 16 h of light and 8 h of dark. Tobacco plants were grown at 25°C in growth rooms under a light regime of 12 h of light and 12 h of dark. *Arabidopsis* pollen tubes were germinated

on a solid medium containing 18% (w/v) sucrose, 0.01% (w/v) boric acid, 1 mM $CaCl_2$, 1 mM $Ca(NO_3)_2$, 1 mM $MgSO_4$, and 0.5% (w/v) agar. Tobacco pollen tubes were germinated in a liquid medium containing 18% (w/v) sucrose, 0.01% (w/v) boric acid, 5 μM $CaCl_2$, 5 μM $Ca(NO_3)_2$, and 1 mM $MgSO_4$. Pollen tubes were incubated at 28 ℃ for 3-4 hours before observation under microscope.

For LatB treatment of *Arabidopsis* pollen tubes, LatB dissolved in DMSO was added to a liquid *Arabidopsis* pollen tube medium (same as the solid medium except without agar) to a final concentration of 5 nM or 20 nM. The liquid medium with LatB was then added to pollen tubes 45 minutes or 10-15 minutes before observation, respectively.

Immunostaining of pectin in pollen tubes

Pollen tubes grown on a solid medium were treated with fixative (4% paraformaldehyde, 3 mM $MgSO_4$, 2mM $CaCl_2$, 18% Sucrose, 50 mM PIPES buffer, pH 6.9) for 1 hour. After washing gently with PBS buffer 3 times for 5 minutes each, pollen tubes were incubated with the purified JIM5 and JIM7 polyclonal antibodies (1:300 and 1:600 dilution in PBS respectively) at 4°C over night. After washing three times for 10 minutes each in PBS buffer, pollen tubes were incubated with secondary antibody, FITC-conjugated rabbit anti-rat IgG or TRITC-conjugated goat anti-rat IgG (1:250 dilution for JIM5 and 1:500 dilution for JIM7 in PBS) at room temperature for 2 hours. After three washes with PBS buffer, pollen tubes were observed under a confocal microscope.

Confocal microscopy and image analysis

Pollen tubes expressing fluorescently-labeled protein were imaged by Leica SP2 or Leica SP5 laser scanning confocal microscope. Conditions for imaging were set as 488 nm excitation and 500-535 nm emission for GFP; 514 nm excitation and 525–640 nm emission for YFP; 458 nm excitation and 465–490 nm emission for CFP; 543 nm excitation and 555–664 nm emission for mCherry; 488 nm excitation and 500-540 nm emission for FITC; 543 nm excitation and 555–620 nm emission for TRITC. The median planes of pollen tube tips were taken for analyzing the distribution of fluorescent signals. Image quantification was performed using the ImageJ software (version 1.45s). A segmented line was drawn along the cell periphery to measure the distribution of fluorescent signal on the PM.

For FRAP analysis to measure the diffusion constant of proteins on the PM, GFP-ROP1 overexpression pollen tubes were treated with 20 nM Lat B for 10-15 minutes to suppress F-actin dependent exocytosis. GFP-ROP1 signal in a small region at the apical PM was photobleached with 100% laser power (488 nm), and time-lapse videos were taken with 6 s time interval between frames. The distribution curves of GFP-ROP1 was used to fit with the diffusion equation of protein on the PM and to estimate the diffusion constant.

The exocytosis rates of PRK1-Dendra2 in pollen tubes were measured using Corrected Fluorescence Recovery After Photoconversion (cFRAPc) (Luo et al., 2016). The green form of Dendra2 was excited by 488 nm laser with 5% laser power and detected at 500-535nm; the red form was excited by 543 nm laser with 40% laser power and detected at

555-620 nm. Photoconversion of Dendra2 was performed by scanning the region-of-interest with 3% UV laser twice. Post-conversion time-lapse videos were taken immediately after photoconversion, with 5.16 s time interval between frames. Data analysis was performed in MatLab software.

For FRET analysis, pLat52-CFP-ROP1 or pLat52-CFP-DNrop1 was transiently coexpressed with pLat52-CRIB4-YFP in tobacco pollen tubes, while pollen tubes expressing pLat52-CRIB4-YFP, pLat52-CFP-ROP1 or pLat52-CFP-DNrop1 alone served as controls to calculate the bleed-through ratio. CFP and YFP images were acquired using the settings specified above. FRET signals were acquired simultaneously using 458 nm for excitation and 525–640 nm for emission. The FRET index normalized by the intensity of the donor was calculated using the ImageJ plug-in “FRET and Colocalization Analyzer” (Hachet-Haas et al., 2006).

Figures and Tables

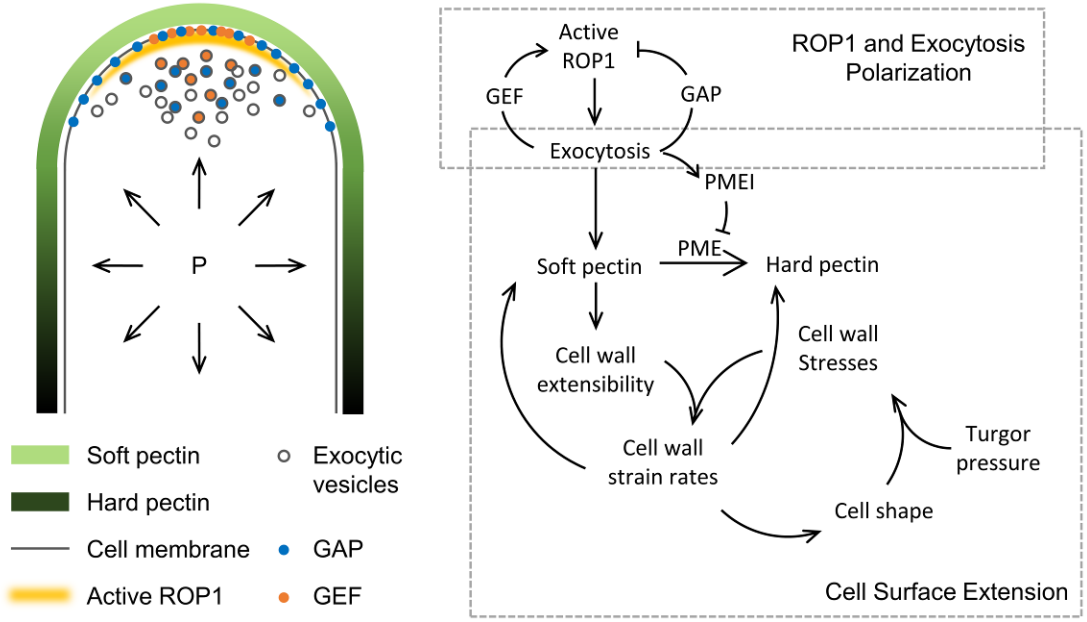

Figure 1-1. A conceptual model of ROP1-regulated pollen tube tip growth.
The model consists of the ROP1 and Exocytosis Polarization Module and the Cell Surface Extension Module. Active ROP1 localizes to the PM of the pollen tube apex through positive and negative feedback loops involving exocytosis. Polarized exocytosis induced by active ROP1 couples the ROP1 signaling to the composition and mechanics of the cell wall. Newly synthesized soft pectin is delivered to the pollen tube apex by exocytic vesicles and converted to hard pectin on the shank. The resulted asymmetric cell wall extensibility together with turgor pressure ("P" and arrows) determine the strain rates and thereby the geometry of the cell wall.

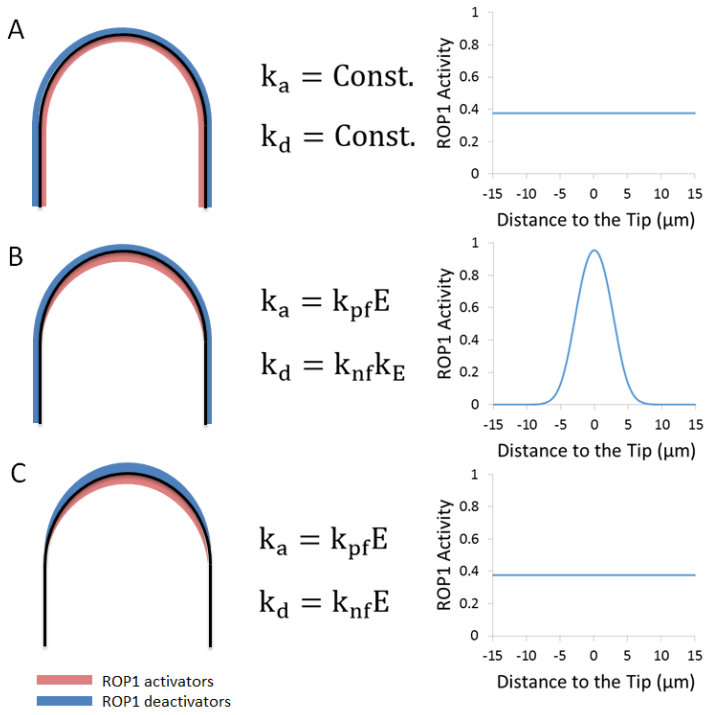

Figure 1-2. Computational simulation testing different modes of feedback for ROP1 polarization.

(A) When the distribution of the activators and the deactivators of ROP1 are independent of exocytosis, the model is not able to generate polarized active ROP1. **(B)** Active ROP1 polarizes when the activators are concentrated on the tip by local positive feedback through exocytosis and the deactivators are evenly distributed by global inhibition. **(C)** With local inhibition, active ROP1 is not able to polarize either.

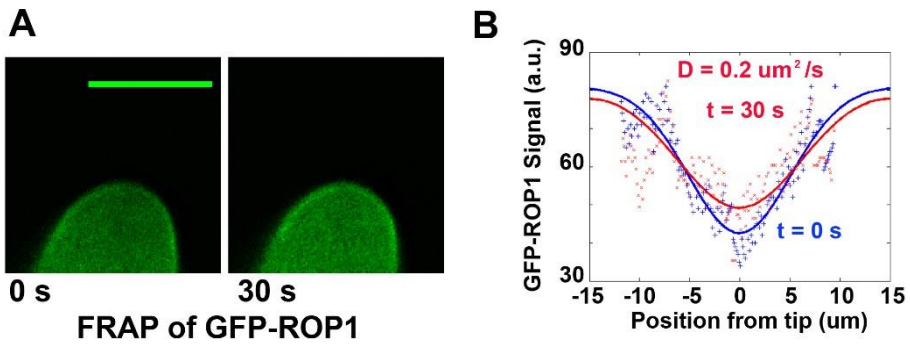

Figure 1-3. Measuring the diffusion constant of membrane ROP1 in pollen tubes by FRAP.

(A) Representing confocal microscopy images of FRAP. *Arabidopsis* pollen tubes expressing GFP-ROP1 were treated by liquid pollen tube growth medium containing 50nM LatB for 30min. Control pollen tubes treated by 0.2% DMSO displayed no growth defects and were not shown. The cell membrane at the tip of pollen tubes is photobleached by high intensity 488nm laser light, and time-lapse images were taken for 30s. Scale bar: 5 μm. **(B)** Distribution of GFP-ROP1 along the cell periphery immediately after photobleaching (t = 0s) and 30s after photobleaching (t = 30s).

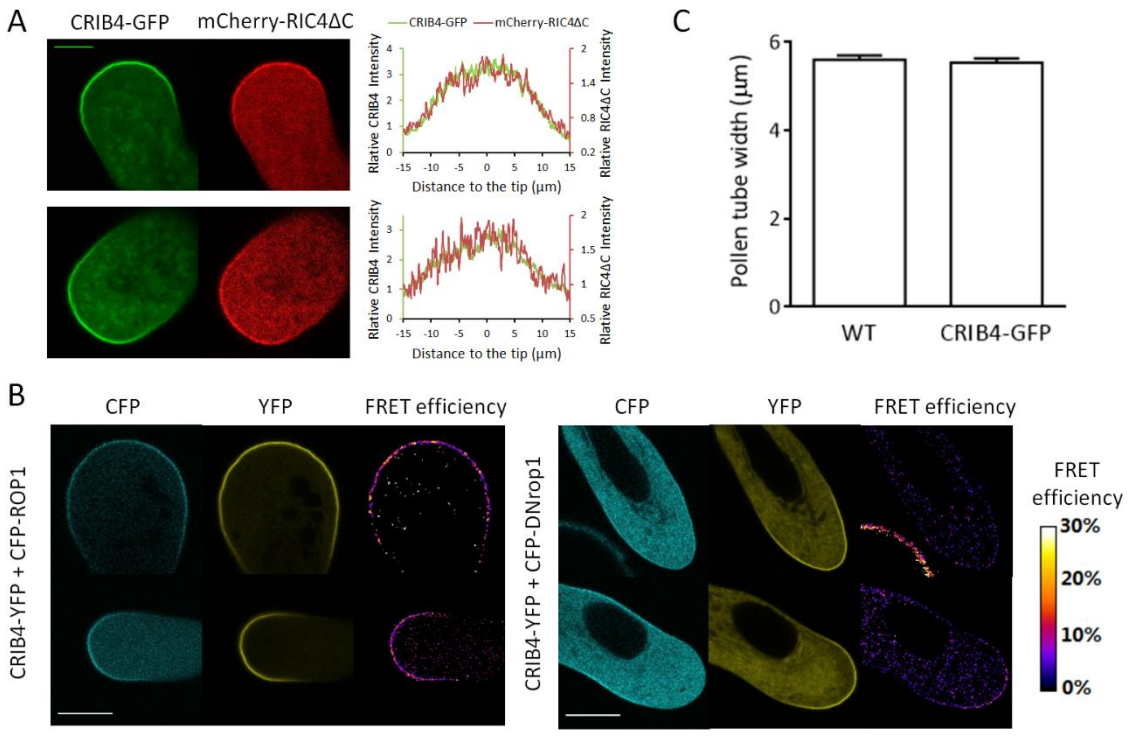

Figure 1-4. CRIB4 is a specific marker for active ROP1
(A) CRIB4-GFP co-localizes with mCherry-RIC4ΔC in tobacco pollen tubes. Scale bar: 5 μm. **(B)** FRET between CRIB4-YFP and CFP-ROP1/DNrop1 shows that CRIB4 preferentially binds with active ROP1. Scale bar: 5 μm. **(C)** Expressing CRIB4-GFP in *Arabidopsis* pollen tubes does not affect the shape of pollen tubes. Error bars show S.E.M..

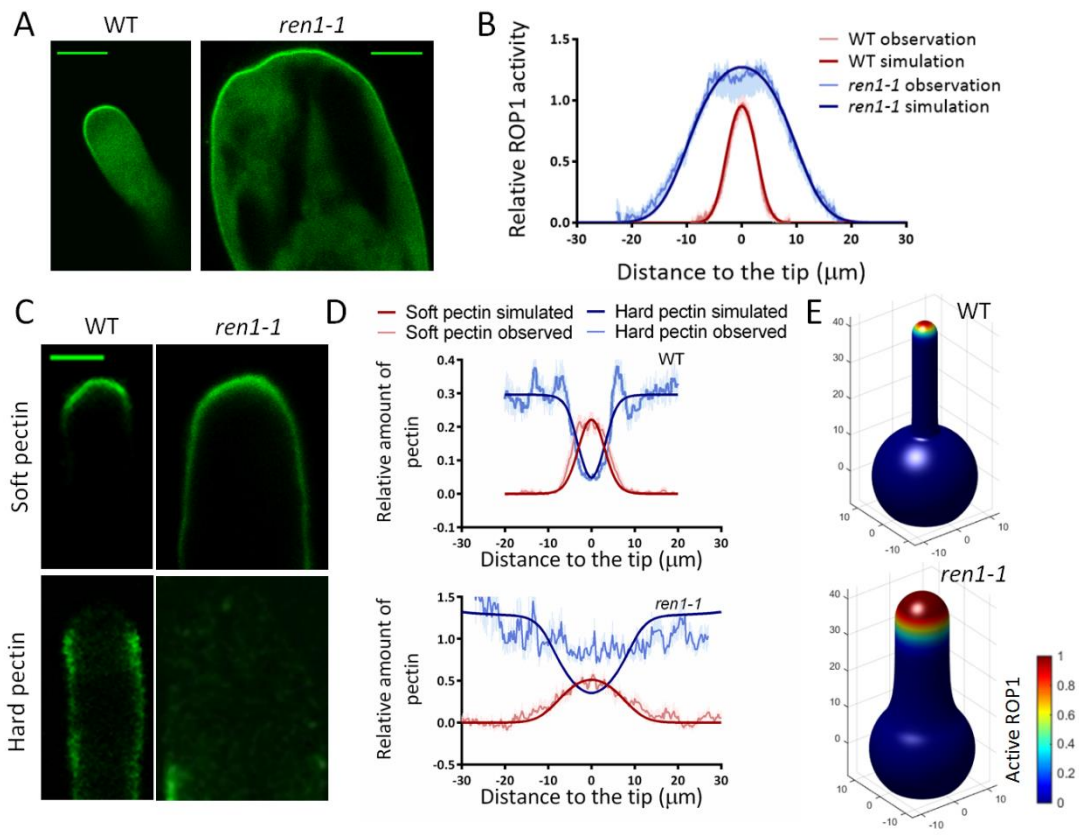

Figure 1-5. Modeling the growth of pollen tubes defective in ROP1 signaling.
(A) Confocal microscopy images of WT and *ren1-1 Arabidopsis* pollen tubes expressing CRIB4-GFP which shows the distribution of active ROP1. Scale bar: 5 μm. **(B)** Comparison of observed and simulated distribution of active ROP1 in WT and *ren1-1* pollen tubes. The curves of observed distribution are the average curves measured from 24 WT and 14 *ren1-1* pollen tubes. **(C)** Confocal microscopy images of pectin immunostaining of WT and *ren1-1* pollen tubes with JIM7 and JIM5. Scale bar: 5 μm. **(D)** Observed and simulated distribution of pectins in WT and *ren1-1* pollen tubes. **(E)** Simulation of WT and *ren1-1* pollen tube shape. The sphere represents the pollen grain. Color indicates the level of active ROP1 in the PM. Unit of axes: μm. Error bars show S.E.M..

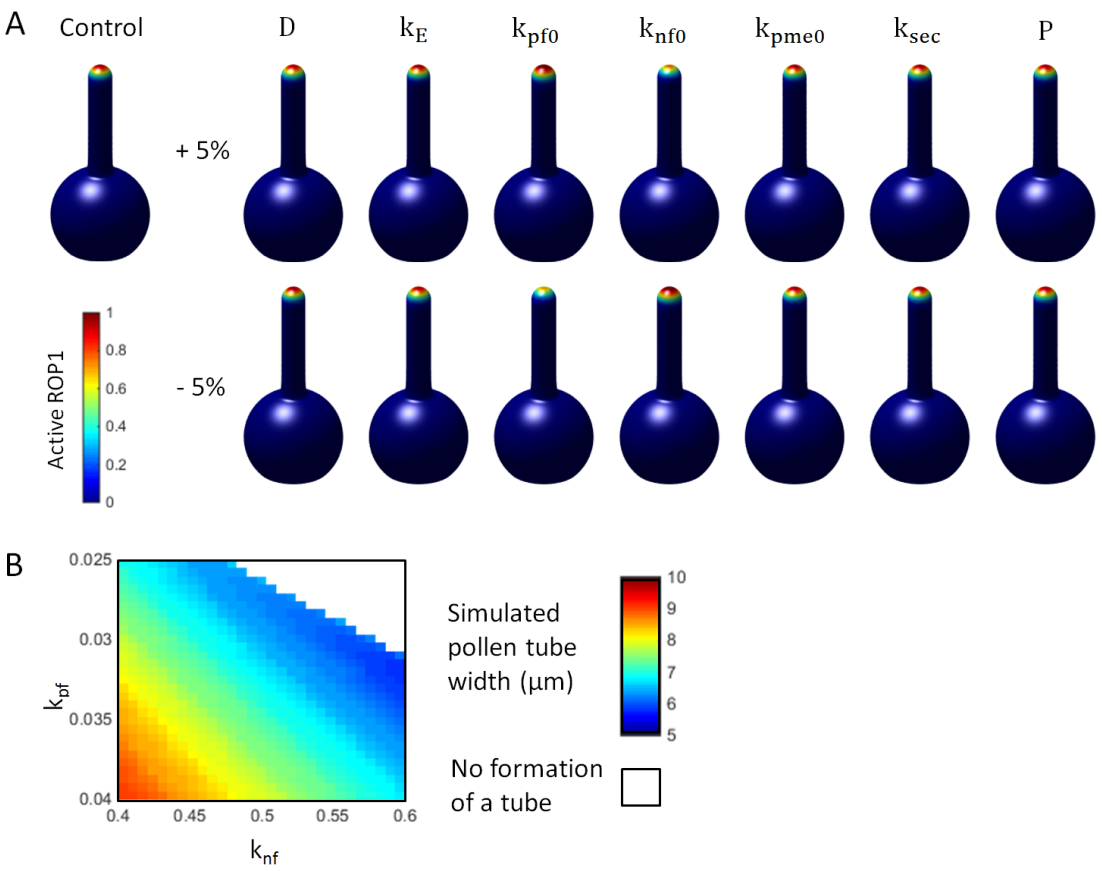

Figure 1-6. Testing the robustness of the model
(A) The model is able to generate stable growing pollen tubes when different parameters are altered by 5%. Color shows the level of ROP1 activity. **(B)** Altering k_{pf} and k_{nf} results in pollen tubes with different width.

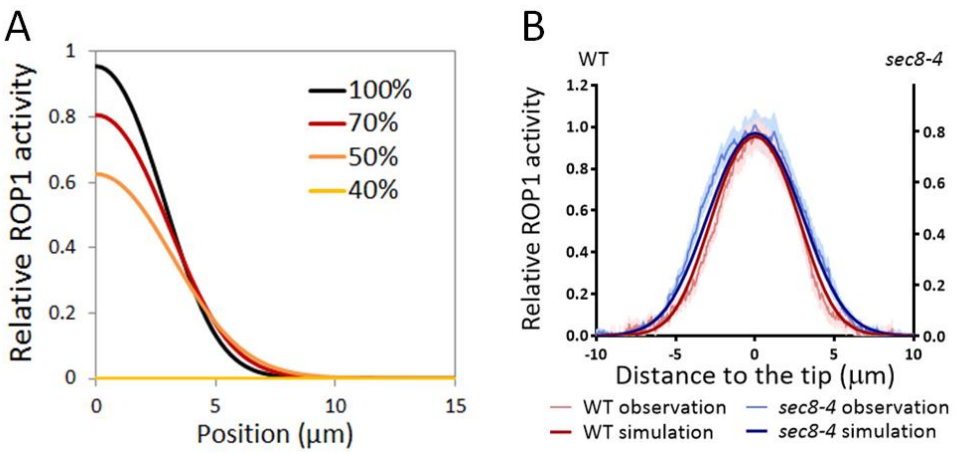

Figure 1-7. Simulation of active ROP1 distribution in pollen tubes with different levels of exocytosis.

(A) Simulation of active ROP1 distribution in pollen tubes with different levels (percentage of WT level) of exocytosis. **(B)** Comparison of observed and simulated distribution of active ROP1 in WT and *sec8-4* pollen tubes.

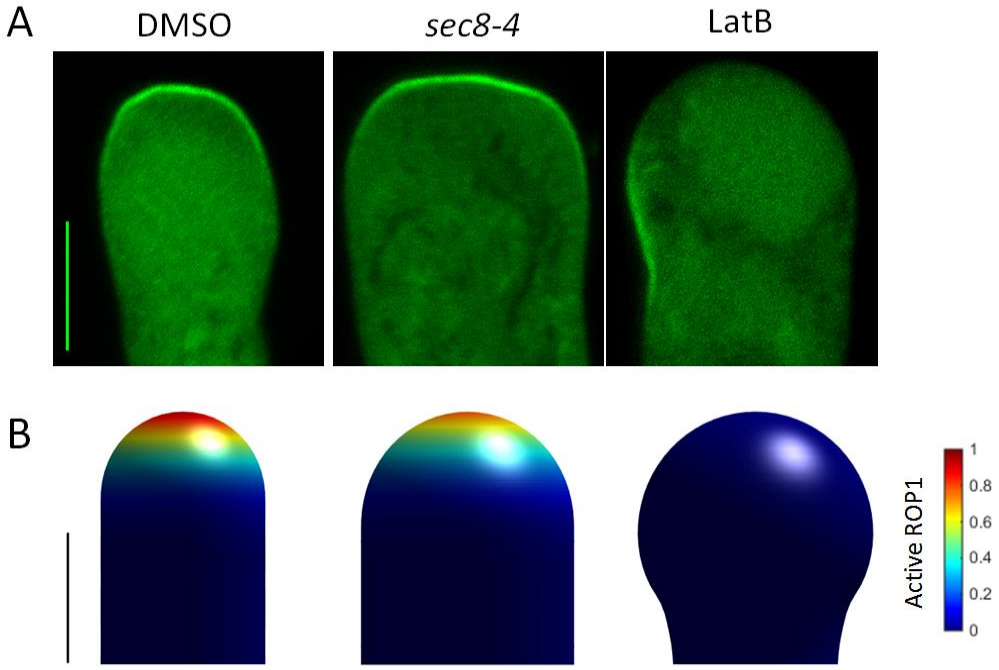

Figure 1-8. Modeling the growth of pollen tubes defective in exocytosis.
(A) Confocal microscopy images of WT, *sec8-4* and LatB treated pollen tubes expressing CRIB4-GFP. Scale bar: 5 μm. **(B)** Simulation of WT, *sec8-4* and LatB treated pollen tubes. Only the tip region of pollen tubes was shown. Color indicates the level of active ROP1 on the PM. Scale bar: 5 μm.

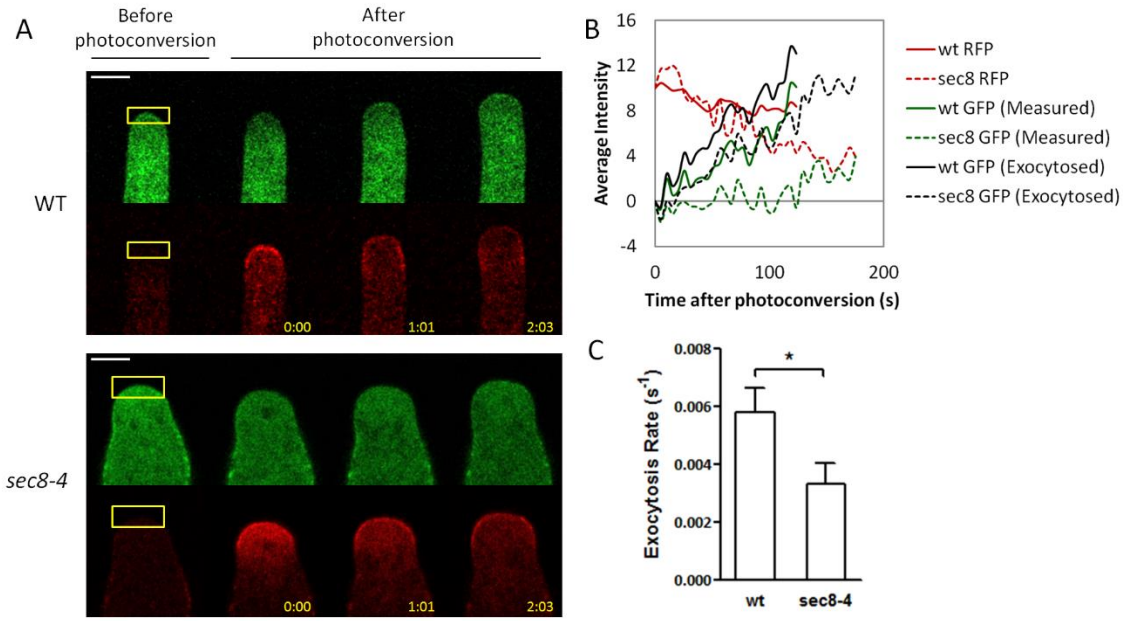

Figure 1-9. Measuring the exocytosis rate of *sec8-4* pollen tubes by Corrected Fluorescence Recovery after Photoconversion (cFRAPc)

(A) Representative cFRAPc images of WT and *sec8-4* pollen tubes expressing PRK1-Dendra2. In each panel both green and red channels were shown. Yellow boxes indicate the photoconverted regions. Numbers show time after photoconversion (min:sec). Scale bar: 5 μm. **(B)** Time-courses of average fluorescent intensity in the photoconverted regions of the two example pollen tubes shown in (A). Green and red curves are the green and the red fluorescent intensity measured from the images. The reduction rate of the red fluorescence was used to correct the measured green fluorescence curves and obtain the actual exocytosed green fluorescence which was shown by the black curves. **(C)** Average exocytosis rate of WT (n=15) and *sec8-4* (n=15) pollen tubes. Error bars show S.E.M.. * $P \leq 0.05$ (unpaired Student's t-test).

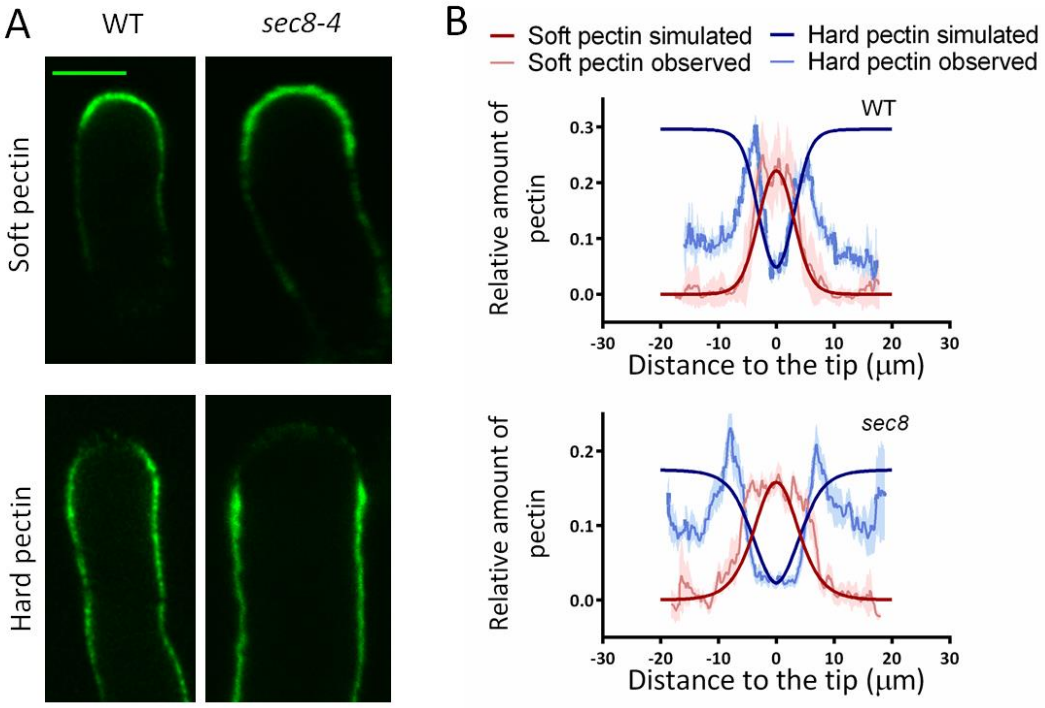

Figure 1-10. Simulation of the pectin distribution in *sec8-4* pollen tubes.
(A) Confocal microscopy images of pectin immunostaining of WT and *sec8-4* pollen tubes with JIM7 and JIM5. Scale bar: 5 μm. **(B)** Observed and simulated distribution of pectins in WT and *sec8-4* pollen tubes. Error bars show S.E.M..

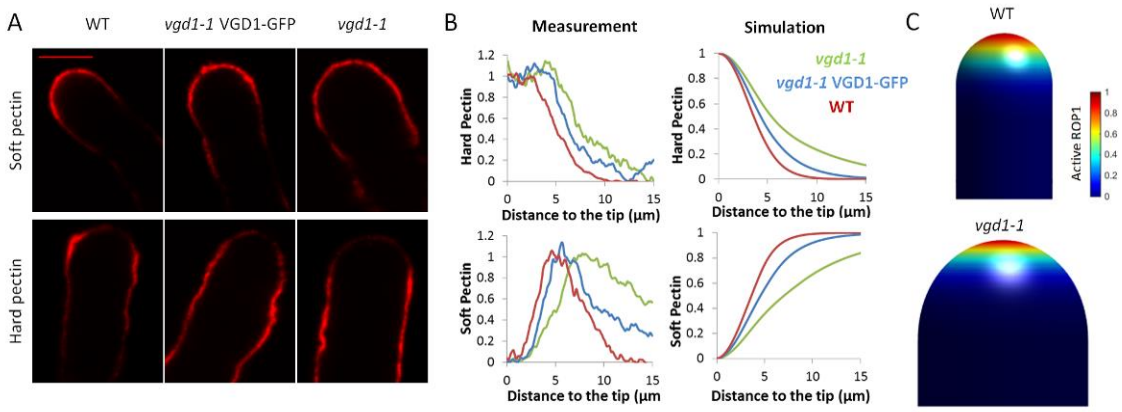

Figure 1-11. Simulation of the pectin distribution in *vgd1-1* pollen tubes.
(A) Confocal microscopy images of pectin immunostaining of WT, *vgd1-1* and *vgd1-1* VGD1-GFP pollen tubes with JIM7 and JIM5. Scale bar: 5 μm. **(B)** Observed and simulated distribution of pectins in WT, *vgd1-1* and *vgd1-1* VGD1-GFP pollen tubes. Error bars show S.E.M.. **(C)** Simulation of WT and *vgd1-1* pollen tubes. Only the tip region of pollen tubes was shown. Color indicates the level of active ROP1 on the PM. Scale bar: 5 μm.

Table 1-1. Parameter setting for the ROP1 and Exocytosis Polarization module

Variables	Definition	Unit
s	Meridional position on the PM	μm
t	Time	s
R	The concentration of active ROP1 in the PM	1
R_{in}	The concentration of inactive ROP1 in the cytoplasm	1
k_a	ROP1 activation coefficient	1/s
k_d	ROP1 deactivation coefficient	1/s
E	Exocytosis rate	1
Constants	**Definition**	**Value**
R_{max}	Maximum active ROP1 concentration on the PM	5
R_{total}	Total ROP1 (including active and inactive ROP1)	30
D	Diffusion coefficient of ROP1 on the PM	0.2 $\mu m^2/s$
k_E	Coefficient linking ROP1 activity with exocytosis rate	1
α	Coefficient representing the degree of nonlinearity in the positive feedback	1.25
k_{pf}	Strength of exocytosis-mediated positive feedback	0.0280/s
k_{nf}	Strength of exocytosis-mediated negative feedback	0.5081/s

Table 1-2. Parameter setting for the Cell Surface Extension module

Variables	Definition	Unit
s	Meridional position on the PM	μm
t	Time	min
C_{PME}	The concentration of PME on the PM	1
C_{PMEI}	The concentration of PMEI on the PM	1
P_s	The concentration of soft (methyl esterified) pectin	1
P_h	The concentration of hard (de-esterified) pectin	1
E	Exocytosis rate	1
v_s	Local velocity on the meridional direction	μm/min
Φ	Relative cell wall extensibility	1/(MPa·min)
P_s^*	The concentration of effective soft pectin	1
E_t	Exocytosis rate at the tip, $E(s = 0)$	1
σ_s	Normal stress on the meridional direction	MPa
σ_θ	Normal stress on the circumferential direction	MPa
κ_s	Curvature of the cell wall on the meridional direction	1/μm
κ_θ	Curvature of the cell wall on the circumferential direction	1/μm
$\dot{\varepsilon}_s$	Strain rate on the meridional direction	1/min
$\dot{\varepsilon}_\theta$	Strain rate on the circumferential direction	1/min
v_n	Local velocity on the normal direction	μm/min
v_s	Local velocity on the meridional direction	μm/min
r	Cross-sectional radius of the cell	μm
φ	The angle between the normal to the surface and the cell axis	rad
Constants	**Definition**	**Value**
k_{pmei}	Coefficient linking exocytosis rate with the concentration of PMEI	0.9
k_{sec}	Coefficient of soft pectin secretion by exocytosis	0.1/min
k_{pme}	Pectin de-esterification rate	0.8/min
Φ_s	Extensibility of soft pectin	20/(MPa·min)
k_s	Thresholding coefficient for effective soft pectin	0.38
P	Turgor pressure	0.2 MPa [1]
δ	Thickness of the cell wall	0.2 μm [2]
ν	The Poisson's ratio	0.5

[1] Benkert et al., 1997.
[2] Chebli et al., 2012.

Chapter 2 Mathematical Modeling of Pollen Tube Guidance

Abstract

Various tip-growing cells are able to grow toward a target in response to extracellular guidance signals. The association of growth guidance and tip growth suggests an underlying mechanistic connection between these two processes. During the tip growth of *Arabidopsis* pollen tubes, the tip-localized ROP1 signaling controls the polar extension of the cell wall through its regulation of the polarized exocytosis at the tip of the cell. We hypothesize that ROP1 signaling is also the key player that controls the growth direction by responding to the gradient of the guidance signals. Based on this hypothesis, we developed a 3-dimensional mathematical model for growth guidance of pollen tubes. In this model, the dynamics of active ROP1 is modulated by the distribution of an extracellular guidance signal, and the distribution of ROP1 on the cell surface determines the mechanical properties of the cell wall and thereby the geometry of the cell. The model reproduced the shifting of ROP1 distribution in response to a guidance signal gradient and the turning of pollen tubes, which are validated by experimental observations. Altering different parameters in the model changes the behavior of pollen tubes and the guidance efficiency, revealing the roles of different factors in pollen tube guidance.

Introduction

Growth guidance is a process by which cells direct their growth according to external signals, enabling cells to respond rapidly to the environment and accomplish their biological functions. Growth guidance is found across eukaryotic kingdoms: amoebae

migrating towards food sources, hyphae of fungus attracted by reproductive units, and axons in the animal nervous system that follows precise paths to reach their targets. In plants, pollen tube, the male gametophyte of angiosperm, is an ideal model system to study growth guidance. Attracted by diffusive signals from the female tissues, pollen tubes are able to travel through the pistil and find the ovules in a highly precise and efficient manner.

Cells exhibiting growth guidance are always tip-growing cells, suggesting a mechanistic association between these two processes. Here we propose that the mechanisms of pollen tube guidance are connected with the signaling of pollen tube tip growth: the ROP1 signaling network controls the turnings of pollen tube in guidance. Like other model systems showing growth guidance, pollen tubes perceive external signal by membrane-bound receptor-like kinases (RLKs) (Wengier et al., 2003; Tang et al., 2004; Guyon et al., 2004; Takeuchi and Higashiyama, 2016; Wang et al., 2016). RLKs have been shown to interact with GEFs, the positive regulators of ROPs (Takeuchi and Higashiyama, 2016; Zhang and McCormick, 2007). These findings support a potential link between external signals and the ROP1 signaling. In the presence of an asymmetrically distributed guidance signal, ROP1 distribution will shift due to biased positive feedback. Shifted active ROP1 retargets exocytosis and changes the pattern of cell wall extensibility and thereby resulting in the change in the tip growth direction. The redistribution of exocytic vesicles prior to pollen tube turning has already been observed (Bou and Geitmann, 2011).

Many previous studies have presented mathematical models of chemotaxis using bacteria, amoebas or axons as the model system. Most of these models focused on simulating the sensing of the chemoattractant and the attractant-induced polarization of intracellular signaling (Onsum and Rao, 2007; Levine et al., 2006; Narang, 2006; Sakumura et al., 2005; Skupsky et al., 2005; Levchenko and Iglesias, 2002), only a few of them coupled the signaling mechanisms to cell morphology (Arrieumerlou and Meyer, 2005). Attempts had also been made to model pollen tube guidance: a model that links the gradient of the guidance signal to the growth direction of the pollen tube reproduced the trajectory of pollen tubes during guidance (Stewman et al., 2010), but molecular mechanism of how the guidance signal regulates the growth direction is not discussed. Here we present a mathematic model that integrates the polarity of ROP1 signaling with the deformation of cell surface to simulate the growth of pollen tubes in the presence of a guidance signal applied in vitro.

Results

A mathematical model of pollen tube guidance

The model of pollen tube guidance consists of three interconnecting parts, representing the major steps in pollen tube guidance: the perception of the diffusive guidance signal through the GEF-mediated positive feedback loop, the redistribution of the active ROP1 on the PM in response to the signal, and the changes in cell wall mechanics and cell morphology. The position and the shape of the cell, in turn, determine the local concentration of the guidance signal along the cell periphery. The structure of this model is depicted in Figure 2-1.

Firstly, we established the distribution of the guidance signal. Guidance signal molecules are constantly released from the ovules and diffuse over the surface of the medium with diffusion rate D_S and degradation rate k_S. At the stable stage, the distribution of the signal, S, is obtained by

$$D_S\left(\frac{\partial^2 S}{\partial x^2}+\frac{\partial^2 S}{\partial y^2}\right)-k_S S=0$$

$$S(x,y)=S_0, \qquad x,y\in\Omega$$

$$S(x,y)=0, \qquad x,y\in\Gamma$$

where S_0 is the concentration of the guidance signal at the source, Ω is the location of the signal source and Γ is the boundary of the field. The steepness of the signal gradient increases with higher S_0, and the broadness of the signal distribution increases with higher diffusion rate (D_S) (Figure 2-2).

We propose that ROP1 signaling, the key regulator of pollen tube tip growth, also controls pollen tube guidance. Based on this hypothesis, the spatiotemporal distribution of active ROP1, R, in the guidance model is described by similar equations as in the tip growth model, but on the three-dimensional surface of the PM:

$$\frac{\partial R}{\partial t}=k_{pf}R^{\alpha}\left(R_{total}-\int R\,d\Omega\right)\left(1-\frac{R}{R_{max}}\right)-k_{nf}R+D\nabla_A^2 R$$

Similarly, k_{pf} and k_{nf} are the strength of the positive and the negative feedbacks, respectively. R_{total} is the total amount of active ROP1 on the cell surface, R_{max} is the local maximum active ROP1, and D is the diffusion rate of ROP1 on the PM. ∇_A^2 is the Laplace–Beltrami operator for the surface of the PM, A. Figure 2-3A shows the formation of a stable

"cap" of active ROP1 on the surface of a semi-sphere. As expected, with higher k_{pf} or lower k_{nf}, the ROP1 cap becomes broader and its peak intensity becomes higher.

Guidance signal locally activates ROP1 through its positive regulator, GEF. Therefore, in the presence of the guidance signal, the local k_{pf} is positively correlated with the signal concentration:

$$k_{pf} = k_{pf0}(1 + S)$$

where k_{pf0} is the basal strength of the positive feedback when the guidance signal is absent. When the guidance signal forms a gradient along the width of a pollen tube, the distribution of active ROP1 will shift towards the side with higher signal concentration due to the asymmetric kpf (Figure 2-3B).

The cell wall of pollen tube is approximated as a thin layer of viscoplastic material (Dumais et al., 2006). The extensibility of the cell wall is determined by the local ROP1 activity.

$$\Phi = \Phi_0 R$$

Using the thin shell theory, assuming the plane stress condition ($\sigma_z = \tau_{yz} = \tau_{zx} = 0$), the strain rate field is

$$\dot{\boldsymbol{\varepsilon}} = \begin{Bmatrix} \dot{\varepsilon}_x \\ \dot{\varepsilon}_y \\ \dot{\gamma}_{xy} \end{Bmatrix} = \begin{Bmatrix} \dfrac{\partial \dot{u}}{\partial x} \\ \dfrac{\partial \dot{v}}{\partial x} \\ \dfrac{\partial u}{\partial y} + \dfrac{\partial v}{\partial x} \end{Bmatrix} + \begin{Bmatrix} -z\dfrac{\partial^2 \dot{w}}{\partial x^2} \\ -z\dfrac{\partial^2 \dot{w}}{\partial y^2} \\ -2z\dfrac{\partial^2 \dot{w}}{\partial x \partial y} \end{Bmatrix}$$

where $\dot{u}$, $\dot{v}$ and $\dot{w}$ are the displacement velocities.

The stress field is

$$\boldsymbol{\sigma} = \begin{Bmatrix} \sigma_x \\ \sigma_y \\ \tau_{xy} \end{Bmatrix} = \frac{1}{\Phi(1-\nu^2)} \begin{bmatrix} 1 & \nu & 0 \\ \nu & 1 & 0 \\ 0 & 0 & \frac{1-\nu}{2} \end{bmatrix} \begin{Bmatrix} \dot{\varepsilon}_x \\ \dot{\varepsilon}_y \\ \dot{\gamma}_{xy} \end{Bmatrix}$$

where ν is the Poisson's ratio. The equilibrium equation is derived based on the Principle of Virtual Work. We used the Finite Element Method (FEM) to solve the equations numerically (Onate, 2013; Logan, 2012). The surface of the pollen cell wall is discretized into small triangular elements, which are interconnected at their vertices, the nodes (Figure 2-4A), and each element is approximated as a thin plate. The geometry of the deformed cell wall after a small time period is obtained by calculating the displacements of each node (Figure 2-4B). The mesh is refined by inserting new nodes at the midpoint of edges exceeding a certain threshold (Figure 2-4C).

Simulation of the dynamics of active ROP1 and cell morphology in pollen tube guidance

The ROP1 signaling equations and the cell wall mechanical equations are combined to simulate the morphogenesis of pollen tube with polarized ROP1. When guidance signals are absent, given an initial stimulation at the surface of a spherical pollen grain, active ROP1 polarizes spontaneously, enhancing the local extensibility of the cell wall and leading to axisymmetric cell growth (Figure 2-5A). In this case, the shape of the simulated pollen tube is identical with that generated by the tip growth model.

At the presence of an asymmetrically distributed guidance signal, active ROP1 accumulates to a location on the cell surface that is closest to the signal source, producing

a pollen tube growing towards the source (Figure 2-5B). When the source of the signal moves, ROP1 distribution shifts at the tip of the tube, and the pollen tube makes turnings to follow the signal, as observed in previous studies (Okuda et al., 2009; Okuda and Higashiyama, 2010).

In our model, the simulated pollen tube is very sensitive to low concentration of guidance signal. We reduced the concentration of guidance signal at the source from 1 to 0.05 and increased the distance of the source to the tip of the pollen tube (Figure 2-6A). At the beginning of growth, the values of k_{pf} at the two sides of the pollen tube only have a difference of 0.03%, which is already sufficient to bias the distribution of the active ROP1 at the tip of the pollen tube, leading to a tendency of the tube to lean towards the side of the signal source. When the pollen tube gets closer to the source, it begins to make a gradual turning and grow straight to the target, while the values of k_{pf} at the two sides of the pollen tube differ only for 0.09% (Figure 2-6A).

The sensitivity of the model may compromise its robustness against environmental noises. Therefore, we tested whether the simulated pollen tube is able to maintain its polarity when exposed to random fluctuation of guidance signal. In the presence of noises that makes k_{pf} fluctuate from 100% to 140% k_{pf0}, the pollen tube waves slightly but the general direction of growth is relatively stable (Figure 2-6B). Furthermore, the pollen tube is able to efficiently discern a gradient of guidance signal overlaid with the noises (Figure 2-6C).

Therefore, our model shows that the ROP1-signaling based system captures the balance of stability and responsiveness of real pollen tubes.

Analysis of factors that affect the guidance efficiency of pollen tubes

To investigate the role of different factors in pollen tube guidance, we altered parameters in the guidance signal equations, the ROP1 distribution equations or the cell wall mechanics of the model, and observed the behavior of pollen tubes during turnings when exposed to a gradient of guidance signal.

Firstly, when the concentration of the guidance signal at the source (S_0) is high, producing a steep gradient, the active ROP1 distribution shifts quickly and the pollen tube makes a sharp turning. On the other hand, with a low S_0 and therefore, a shallow gradient, the pollen tube can also efficiently sense it, but the shifting of ROP1 and the turning are much slower and smoother (Figure 2-7A). A sharper turning allows a shorter path to the source of the guidance signal, so the sharpness of the turning indicates the efficiency of guidance. Therefore, as anticipated, a higher concentration of guidance signal released from the ovules attracts pollen tubes more efficiently.

Secondly, we altered parameters in the ROP1 distribution equations to change the level of active ROP1 at the tip of pollen tubes. For example, when the basal strength of the positive feedback of ROP1, k_{pf0}, is increased, ROP1 activity becomes higher and broader, and consequently, the pollen tube grows faster and wider. However, the speed of ROP1 shifting

and the sharpness of the turning show no obvious difference (Figure 2-7B). Therefore, although the distribution of ROP1 affects the shape and the growth rate of pollen tubes, it has little effect on the efficiency of pollen tube guidance.

Finally, we altered Φ_0, the coefficient linking ROP1 activity to cell wall extensibility. Altering this coefficient does not affect ROP1 distribution, therefore, ROP1 shifts at the same rate in response to the guidance signal. But when Φ_0 is increased, the cell wall of the pollen tube is more expansible so that the pollen tube grows faster. As a result, during the same period of time for ROP1 to redistribute and the growth to change direction, the cell grows a longer distance, so that the turning is smoother (Figure 2-7C). Therefore, in terms of finding the shortest path to the source of guidance signal, slow growing pollen tubes are more efficient, agreeing with previous modeling results (Stewman et al., 2010) and the experimental observation that pollen tubes tend to grow slower when exposed to guidance signals.

Experimental validation for the model

To test the guidance model, we observed the dynamics of ROP1 and the cell morphology of pollen tubes in pollen tube guidance. Pollen tubes are competent to respond to guidance signals only when they have grown through the pistils (Higashiyama et al., 1998). However, it is difficult to observe pollen tubes unless they are growing in vitro. To study pollen tube guidance, a "semi-in vitro" assay was developed (Higashiyama et al., 1998; Palanivelu and Preuss, 2006). In this assay, pollinated stigmas are cut off and placed on a

solid medium. When pollen tubes emerge from the cut end of the stigmas, they are attracted to ovules that are placed nearby. This assay reproduces much of the behavior of in vivo pollen tube guidance. Using this method, we observed the cell morphology of pollen tubes when exposed to guidance signals released from the ovules (Figure 2-8). An ovule was placed on one side of the pollen tube under observation. The micropyle of the ovule was at about 50 μm distance to the tip of the pollen tube. Usually 70%-80% pollen tubes were efficiently attracted by the micropyle or the funiculus of the ovules. As shown by the model, both sharp and smooth turnings were observed (Figure 2-8). As a negative control, none out of 8 pollen tubes were attracted to non-ovule tissue such as petal placed at the same location.

Using CRIB4-GFP as a marker, we observed the distribution of active ROP1 in pollen tube guidance using a confocal laser scanning microscope. Among 17 pollen tubes, in 12 of them we observed the redistribution of active ROP1 to a new position that predicts the new growth direction (Figure 2-9). Consistent with the predictions of the model (Figure 2-7), in most of these pollen tubes, we also observed an overall enhancement of ROP1 activity during the turning caused by the promoted positive feedback of ROP1. However, in real pollen tubes, ROP1 activity recovered to the previous level after the turning, while the model predicts that active ROP1 at the tip of pollen tubes will keep increasing when the cell approaches the source of the guidance signal. The discrepancy possibly indicates a negative feedback mechanism in real pollen tubes that maintains the normal level of ROP1 during pollen tube guidance.

Discussion

Our mathematical model of pollen tube guidance is a first model that is able to simulate the asymmetric growth of plant cells. It not only reproduced the stable cell growth as the tip growth model did, but also allows the cell to turn in response to guidance signals. Unlike the tip growth model in which the signaling and the mechanical modules are hierarchical, in the guidance model an interplay exists between them: ROP1 activity controls the cell wall mechanics, while the change in the cell shape and position also affects the distribution of ROP1. The model reproduced the shifting of ROP1 distribution in response to a guidance signal gradient prior to the turning of growth direction, which is validated by experimental observations. Pollen tubes are highly sensitive to guidance signals so that they are able to efficiently target to the ovules through a long distance in the pistil. The model captured the sensitivity of pollen tube guidance as the simulated pollen tube is able to respond to very shallow gradients of guidance signals.

By altering the parameters in the model, we investigated the roles of different factors in pollen tube guidance. The model predicted that a strong guidance signal and low growth rate enhance the efficiency of pollen tube guidance, while the level of ROP1 activity has little effect on the guidance efficiency providing that the cell is able to grow. Future experiments utilizing the semi-in vitro assay are needed to test these predictions. Firstly, to vary the concentration of the guidance signal, we can place ovules at different distances to the tip of pollen tubes. A more precise strategy is to use different amounts of purified small peptides that have been shown to attract pollen tubes, such as the LURE protein (Okuda et

al., 2009). Secondly, to study the relationship between the growth rate and the guidance efficiency of pollen tubes, we can perform a statistical analysis on the correlation between growth rate and the turning angles of pollen tubes in the semi-in vitro experiments. Finally, pollen tubes of mutants defective in the ROP1 signaling, including *ren1-1* and *sec8-4*, will be tested for their guidance efficiency.

Other mechanisms that may play important roles in pollen tube guidance can be integrated into the model in the future. For example, it is proposed that pollen tubes can respond to not only attractive signals secreted by the ovules, but also repellent signals released by other pollen tubes, ensuring that only one pollen tube enter one ovule. The inclusion of this repellence mechanism in the model will allow us to simulate the competition among multiple pollen tubes. Another mechanism that may contribute to the balance between the responsiveness and the stableness of pollen tube growth during guidance is the oscillation of ROP1 signaling. A previous study in fission yeast suggested that the oscillation of Rho GTPase activity promotes the switching from a monopolar to a bipolar distribution of Rho GTPase. It will be interesting to investigate whether the oscillation of ROP1 can enhance the mobility of its distribution, and therefore, increase the sensitivity of pollen tube during guidance.

Materials and Methods

Finite Element Model for the mechanical analysis of the cell wall

First of all, the cell wall is discretized into triangular elements, interconnecting at vertices, the nodes. Each element is approximated as a thin plate and has its own local axes (x', y', z'), where z' is the normal to the plane of the element. The three nodes of an element are i, j and k. The local coordinates of node i is $[x_i, y_i, z_i]^T$ (note that $z_i = 0$). The local displacement vector of a point in the element is

$$\boldsymbol{\varphi}' = \begin{Bmatrix} u' \\ v' \\ w' \end{Bmatrix}$$

where u', v' and w' are the displacements along the x', y' and z' axes, respectively. Define the local nodal displacement vector as

$$\boldsymbol{d'_i} = \begin{Bmatrix} u'_i \\ v'_i \\ w'_i \\ \theta_{x'_i} \\ \theta_{y'_i} \end{Bmatrix}, \quad \boldsymbol{d'} = \begin{Bmatrix} \boldsymbol{d'_i} \\ \boldsymbol{d'_j} \\ \boldsymbol{d'_k} \end{Bmatrix}$$

where

$$\theta_{x'} = \frac{\partial w'}{\partial x'}, \quad \theta_{y'} = \frac{\partial w'}{\partial y'}$$

(1) Shape functions

Each element has 15 degrees of freedom. We use linear expansions for the u' and v' displacements and a cubic expansion for the w' displacement:

$$\begin{Bmatrix} u' \\ v' \\ w' \end{Bmatrix} = \begin{bmatrix} 1 & x' & y' & 0 & 0 & 0 & 0 & 0 & 0 & 0 & 0 & 0 & 0 & 0 & 0 \\ 0 & 0 & 0 & 1 & x' & y' & 0 & 0 & 0 & 0 & 0 & 0 & 0 & 0 & 0 \\ 0 & 0 & 0 & 0 & 0 & 0 & 1 & x' & y' & x'^2 & y'^2 & x'^3 & x'^2y' & x'y'^2 & y'^3 \end{bmatrix} \begin{Bmatrix} a_1 \\ a_2 \\ a_3 \\ b_1 \\ b_2 \\ b_3 \\ c_1 \\ \vdots \\ c_9 \end{Bmatrix}$$

or

$$\boldsymbol{\varphi}' = \boldsymbol{P}\boldsymbol{a}$$

On the other hand,

$$\boldsymbol{d'_i} = \begin{bmatrix} 1 & x_i & y_i & 0 & 0 & 0 & 0 & 0 & 0 & 0 & 0 & 0 & 0 & 0 & 0 \\ 0 & 0 & 0 & 1 & x_i & y_i & 0 & 0 & 0 & 0 & 0 & 0 & 0 & 0 & 0 \\ 0 & 0 & 0 & 0 & 0 & 0 & 1 & x_i & y_i & {x_i}^2 & {y_i}^2 & {x_i}^3 & {x_i}^2 y_i & x_i {y_i}^2 & {y_i}^3 \\ 0 & 0 & 0 & 0 & 0 & 0 & 0 & 1 & 0 & 2x_i & 0 & 3{x_i}^2 & 2x_i y_i & {y_i}^2 & 0 \\ 0 & 0 & 0 & 0 & 0 & 0 & 0 & 0 & 1 & 0 & 2y_i & 0 & {x_i}^2 & 2x_i y_i & 3{y_i}^2 \end{bmatrix} \begin{Bmatrix} a_1 \\ a_2 \\ a_3 \\ b_1 \\ b_2 \\ b_3 \\ c_1 \\ \vdots \\ c_9 \end{Bmatrix}$$

$$\boldsymbol{d}' = \boldsymbol{C}\boldsymbol{a}$$

Therefore,

$$\boldsymbol{\varphi}' = \boldsymbol{P}\boldsymbol{C}^{-1}\boldsymbol{d}' = \boldsymbol{N}\boldsymbol{d}', \qquad \boldsymbol{N} = \boldsymbol{P}\boldsymbol{C}^{-1}$$

where $\boldsymbol{N}$ is the shape function matrix.

(2) Kinematic equations

Assuming the plane stress condition ($\sigma_{z'} = \tau_{y'z'} = \tau_{z'x'} = 0$), the local strain rate field is

$$\dot{\boldsymbol{\varepsilon}}' = \begin{Bmatrix} \dot{\varepsilon}_{x'} \\ \dot{\varepsilon}_{y'} \\ \dot{\gamma}_{x'y'} \end{Bmatrix} = \frac{\partial}{\partial t} \begin{Bmatrix} \dfrac{\partial u'}{\partial x'} - z' \dfrac{\partial^2 w'}{\partial x'^2} \\ \dfrac{\partial v'}{\partial x'} - z' \dfrac{\partial^2 w'}{\partial y'^2} \\ \dfrac{\partial u'}{\partial y'} + \dfrac{\partial v'}{\partial x'} - 2z' \dfrac{\partial^2 w'}{\partial x' \partial y'} \end{Bmatrix} = \boldsymbol{S} \frac{\partial \boldsymbol{\varphi}'}{\partial t}, \boldsymbol{S} = \frac{\partial}{\partial t} \begin{bmatrix} \dfrac{\partial}{\partial x'} & 0 & -z' \dfrac{\partial^2}{\partial x'^2} \\ 0 & \dfrac{\partial}{\partial y'} & -z' \dfrac{\partial^2}{\partial y'^2} \\ \dfrac{\partial}{\partial y'} & \dfrac{\partial}{\partial x'} & -2z' \dfrac{\partial^2}{\partial x' \partial y'} \end{bmatrix}$$

Therefore,

$$\dot{\boldsymbol{\varepsilon}}' = \boldsymbol{B}\frac{\partial \boldsymbol{d}'}{\partial t}, \qquad \boldsymbol{B} = \boldsymbol{SN}$$

(3) Constitutive equations

The local stress field is

$$\boldsymbol{\sigma}' = \begin{Bmatrix} \sigma_{x'} \\ \sigma_{y'} \\ \tau_{x'y'} \end{Bmatrix} = \frac{1}{\Phi(1-\nu^2)} \begin{bmatrix} 1 & \nu & 0 \\ \nu & 1 & 0 \\ 0 & 0 & \dfrac{1-\nu}{2} \end{bmatrix} \begin{Bmatrix} \dot{\varepsilon}_{x'} \\ \dot{\varepsilon}_{y'} \\ \dot{\gamma}_{x'y'} \end{Bmatrix} = \boldsymbol{D}\dot{\boldsymbol{\varepsilon}}'$$

$$\boldsymbol{D} = \frac{1}{\Phi(1-\nu^2)} \begin{bmatrix} 1 & \nu & 0 \\ \nu & 1 & 0 \\ 0 & 0 & \dfrac{1-\nu}{2} \end{bmatrix}$$

(4) Equilibrium equations and the element stiffness equation

Based on the Principle of Virtual Work, we have

$$\frac{\partial U'}{\partial \boldsymbol{d}'} = \frac{\partial \Omega'}{\partial \boldsymbol{d}'}$$

Here U' is the virtual strain energy:

$$U' = \frac{1}{2}\iiint_V \boldsymbol{\sigma}'^T \boldsymbol{\varepsilon}' \mathrm{dV} = \frac{1}{2}\iiint \dot{\boldsymbol{\varepsilon}}'^T \boldsymbol{D}\boldsymbol{\varepsilon}' \mathrm{dV} = \frac{1}{2}\iiint \frac{\partial \boldsymbol{d}'^T}{\partial t}\boldsymbol{B}^T\boldsymbol{D}\boldsymbol{B}\boldsymbol{d}' \mathrm{dV}$$

and Ω' is the virtual work of external forces:

$$\Omega' = \iint_A \boldsymbol{\varphi}'^T \begin{Bmatrix} 0 \\ 0 \\ p \end{Bmatrix} \mathrm{dA}$$

where p is the turgor pressure, V and A are the volume and the surface area of the cell wall, respectively. Therefore,

$$\iiint_V \frac{\partial}{\partial t}\boldsymbol{B}^T\boldsymbol{D}\boldsymbol{B}\boldsymbol{d}' \mathrm{dV} = \iint_A \boldsymbol{N}^T \begin{Bmatrix} 0 \\ 0 \\ p \end{Bmatrix} \mathrm{dA}$$

We define the local stiffness matrix $\boldsymbol{K'}$ and the local force vector $\boldsymbol{f'}$ as

$$\boldsymbol{K'} = \iiint_V \boldsymbol{B}^T \boldsymbol{D} \boldsymbol{B} \mathrm{dV}, \qquad \boldsymbol{f'} = \iint_A \boldsymbol{N}^T \begin{Bmatrix} 0 \\ 0 \\ p \end{Bmatrix} \mathrm{dA}$$

$$\boldsymbol{K'} = \begin{bmatrix} \boldsymbol{K'_{ii}} & \boldsymbol{K'_{ij}} & \boldsymbol{K'_{ik}} \\ \boldsymbol{K'_{ji}} & \boldsymbol{K'_{jj}} & \boldsymbol{K'_{jk}} \\ \boldsymbol{K'_{ki}} & \boldsymbol{K'_{kj}} & \boldsymbol{K'_{kk}} \end{bmatrix}, \boldsymbol{f'} = \begin{Bmatrix} \boldsymbol{f'_i} \\ \boldsymbol{f'_j} \\ \boldsymbol{f'_k} \end{Bmatrix}, \boldsymbol{f'_i} = \begin{Bmatrix} f_{x'_i} \\ f_{y'_i} \\ f_{z'_i} \\ m_{x'_i} \\ m_{y'_i} \\ m_{z'_i} \end{Bmatrix}$$

Then we have the element stiffness equation

$$\boldsymbol{K'd'} = \boldsymbol{f'}$$

As the mesh is refined in this system, singularity of the stiffness matrix may arise due to the quasi-coplanar situation of adjacent elements (Onate, 2013). To avoid the singularity, an arbitrary rotational stiffness k_{θ_z} is inserted into the diagonal of the local stiffness matrix:

$$\bar{\boldsymbol{K}}'_{\boldsymbol{ii}} = \begin{bmatrix} \boldsymbol{K'_{ii}} & \boldsymbol{0} \\ \boldsymbol{0} & k_{\theta_z} \end{bmatrix}$$

The degrees of freedom of each node becomes six instead of five:

$$\bar{\boldsymbol{d}}'_{\boldsymbol{i}} = \begin{Bmatrix} \boldsymbol{d'_i} \\ \theta_{z'_i} \end{Bmatrix} = \begin{Bmatrix} u'_i \\ v'_i \\ w'_i \\ \theta_{x'_i} \\ \theta_{y'_i} \\ \theta_{z'_i} \end{Bmatrix}, \qquad \bar{\boldsymbol{f}}'_{\boldsymbol{i}} = \begin{Bmatrix} \boldsymbol{f'_i} \\ 0 \end{Bmatrix} = \begin{Bmatrix} f_{x'_i} \\ f_{y'_i} \\ f_{z'_i} \\ m_{x'_i} \\ m_{y'_i} \\ 0 \end{Bmatrix}$$

Then we have $\theta_{z'_i} = 0$. The new element stiffness equation becomes

$$\bar{\boldsymbol{K}}' \bar{\boldsymbol{d}}' = \bar{\boldsymbol{f}}'$$

(5) Coordinate transformation

The assembly of the global stiffness equation requires that the stiffness matrix, nodal displacement vector and force vector are defined in the same global coordinate system. Denote the unit vectors of the local coordinate system by $\boldsymbol{i}$, $\boldsymbol{j}$ and $\boldsymbol{k}$, then we have the transformation matrices

$$\boldsymbol{R} = [\boldsymbol{i}, \boldsymbol{j}, \boldsymbol{k}], \qquad \boldsymbol{T_i} = \begin{bmatrix} \boldsymbol{R} & \boldsymbol{0} \\ \boldsymbol{0} & \boldsymbol{R} \end{bmatrix}, \qquad \boldsymbol{T} = \begin{bmatrix} \boldsymbol{T_i} & \boldsymbol{0} & \boldsymbol{0} \\ \boldsymbol{0} & \boldsymbol{T_i} & \boldsymbol{0} \\ \boldsymbol{0} & \boldsymbol{0} & \boldsymbol{T_i} \end{bmatrix}$$

So we have

$$\boldsymbol{d} = \boldsymbol{T}\bar{\boldsymbol{d}}'$$

$$\boldsymbol{f} = \boldsymbol{T}\bar{\boldsymbol{f}}'$$

where $\boldsymbol{f}$ is the element force vector in the global axes

Noting that $\boldsymbol{T}$ is orthogonal, we have

$$\boldsymbol{T}\bar{\boldsymbol{K}}'\boldsymbol{T}^T\boldsymbol{d} = \boldsymbol{f}$$

Therefore, the element stiffness matrix in the global axes is

$$\boldsymbol{K} = \boldsymbol{T}\bar{\boldsymbol{K}}'\boldsymbol{T}^T$$

(6) The global stiffness equation and boundary conditions

The global stiffness matrix and the global force vector are assembled in the standard manner in the FEM. The boundary of the cell wall is fixed:

$$u_i = v_i = w_i = \theta_{x_i} = \theta_{y_i} = 0$$

The implementation and simulation of this analysis are performed in the MatLab software. Parameters are listed in Table 2-1.

Plant and pollen tube growth conditions

Arabidopsis thaliana plants were grown at 22°C in growth rooms under a light regime of 16 h of light and 8 h of dark. *Arabidopsis* pollen tubes were germinated on a solid medium containing 18% (w/v) sucrose, 0.01% (w/v) boric acid, 1 mM $CaCl_2$, 1 mM $Ca(NO_3)_2$, 1 mM $MgSO_4$, and 0.5% (w/v) agar. Tobacco pollen tubes were germinated in a liquid medium containing 18% (w/v) sucrose, 0.01% (w/v) boric acid, 5 μM $CaCl_2$, 5 μM $Ca(NO_3)_2$, and 1 mM $MgSO_4$. Pollen tubes were incubated at 28℃ for 3-4 hours before observation under a microscope.

Semi-in vitro pollen tube guidance assay

Arabidopsis flowers emasculated one day before experiments were pollinated and kept in the growth room for 2-3h. The pollinated stigmas were then cut off with a scalpel, placed horizontally on the surface of a solid pollen tube medium, and kept at 28℃ for 2-3h. Pollen tubes germinated and penetrated the stigmas would emerge from the cut end of the stigmas and grow on the medium. Ovules were cut at the root of the funiculus and taken out from ovaries using a scalpel and a needle, and placed near the tip of pollen tubes (about 50-100 μm from pollen tube tip to the micropyle). To observe pollen tubes making turnings, an ovule was placed on one side of a pollen tube, and the angle between the growth direction of the pollen tube and the line connecting the micropyle and the tip of pollen tube was about 30-60 degrees. Images or videos of pollen tubes were taken right after placing the ovules.

To observe pollen tubes in the semi-in vitro assay on a confocal microscope, the stigmas, pollen tubes and ovules were cultured on a medium on the surface of a cover slide. Before imaging, the cover slide was placed upside down on a glass slide with a concavity, in order to prevent the pollen tubes and ovules being disturbed.

Confocal microscopy

Bright field images of pollen tubes were taken on a Nikon TE300 Eclipse inverted microscope. Pollen tubes expressing CRIB4-GFP were imaged by Leica SP2 laser scanning confocal microscope using 488 nm excitation and 500-535 nm emission. The median planes of pollen tube tips were taken for analyzing the distribution of fluorescent signals.

Figures and Tables

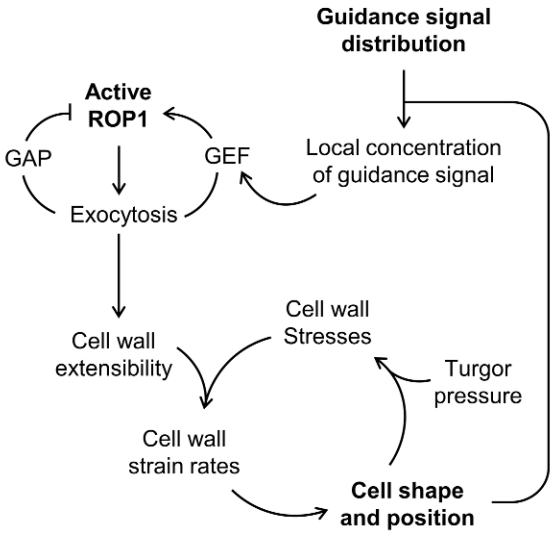

Figure 2-1. A conceptual model of pollen tube growth guidance.
Active ROP1 and exocytosis polarize at the tip of pollen tubes through positive and negative feedbacks and controls the extensibility of the cell wall. The external guidance signal activates ROP1 through promoting the positive feedback of ROP1. The presence of a gradient of guidance signal leads to an asymmetric distribution of active ROP1 and thereby asymmetric cell wall extensibility which changes the growth direction of pollen tubes.

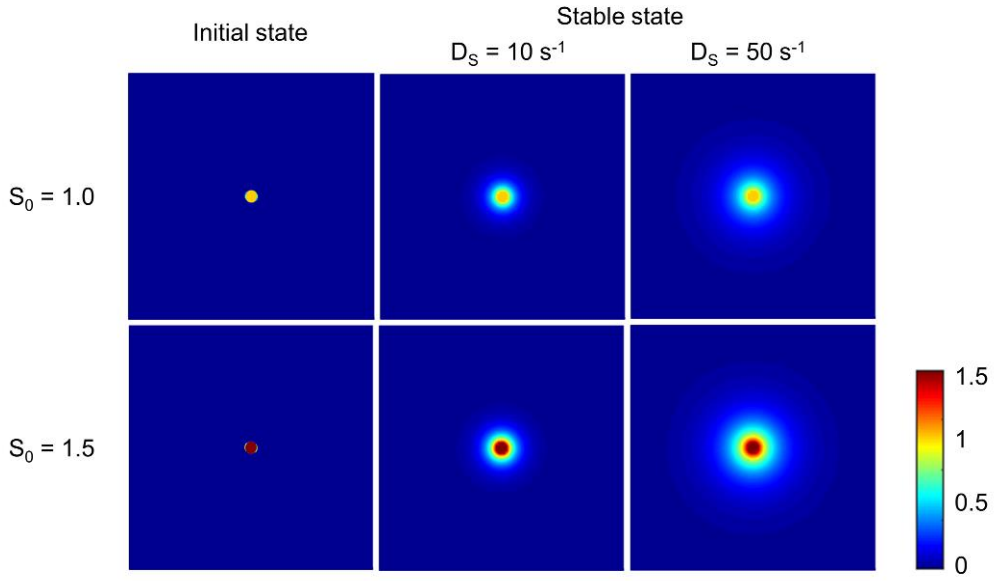

Figure 2-2. Simulated distribution of guidance signal.
The initial state and stable state of a guidance signal diffusing from a source. The concentration of the signal at the source is kept at a constant (S_0). Color shows the concentration of the guidance signal.

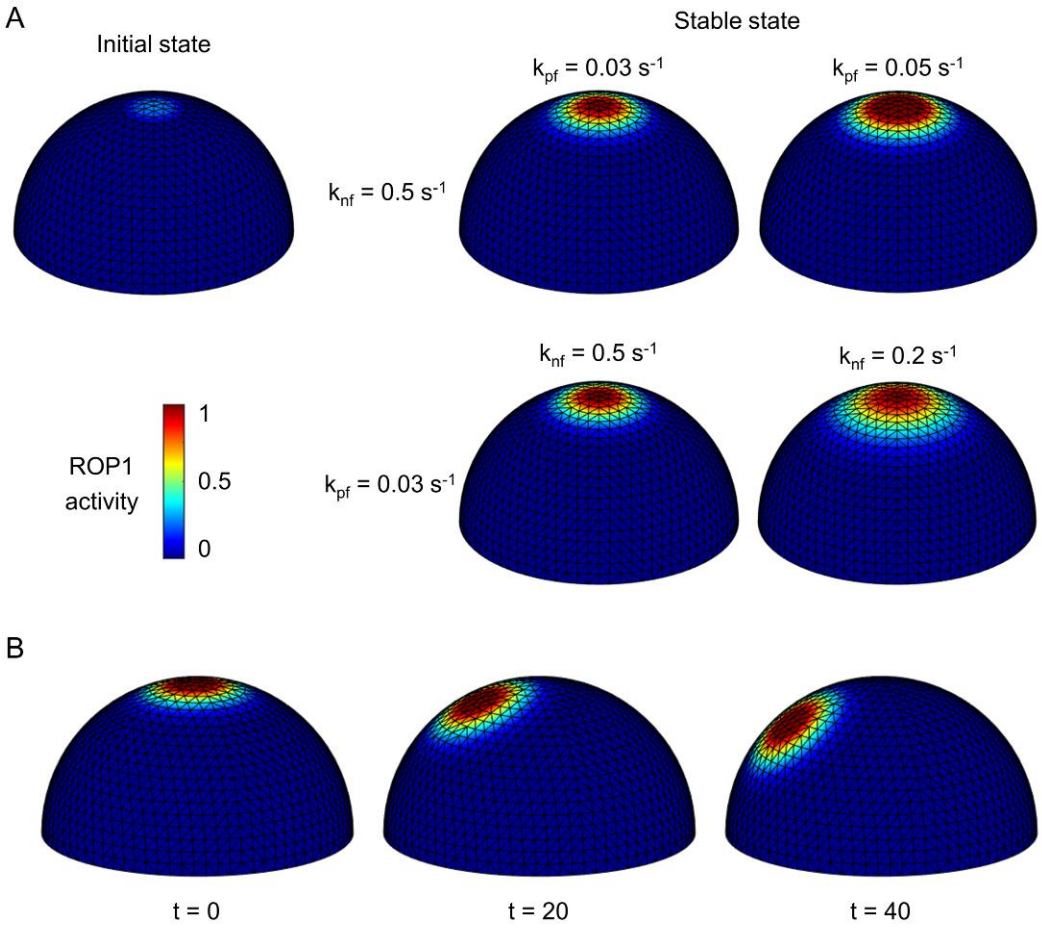

Figure 2-3. Simulation of the polarization of active ROP1 on a 3D surface.
(A) The initial state and stable state of active ROP1 distribution on the surface of a hemisphere. **(B)** The shifting of active ROP1 distribution when exposed to a guidance signal gradient. Color shows the concentration of active ROP1.

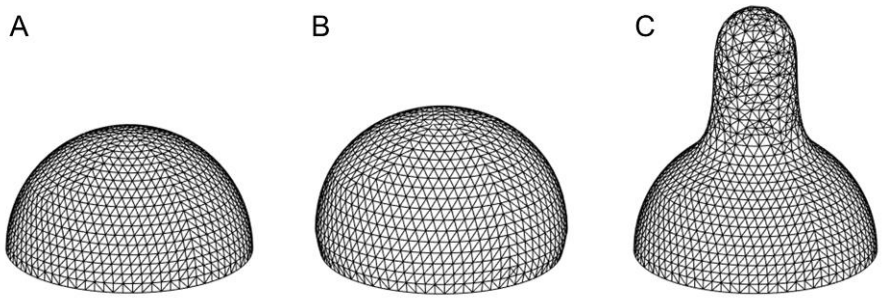

Figure 2-4. Geometry and meshing of the pollen cell wall.
The cell wall of a pollen is divided into interconnecting triangular elements. **(A)** The initial structure of the pollen cell wall before loading with turgor pressure. **(B)** The structure of the pollen cell wall with homogenous extensibility after one growth iteration. **(C)** The structure of the pollen cell wall after 100 growth iteration when the cell wall extensibility is linked to the active ROP1 distribution. The mesh is refined by inserting new nodes into existing elements.

Figure 2-5. Simulation of pollen tube tip growth and turning.
(A) Symmetric growth of a pollen tube in the absence of guidance signal. **(B)** Asymmetric growth of a pollen tube in the presence of an asymmetrically distributed guidance signal gradient. **(C)** Pollen tube makes turnings to follow the direction of the guidance signal gradient. Color in the background shows the concentration of the guidance signal. Color on the surface of the pollen tube shows the concentration of active ROP1.

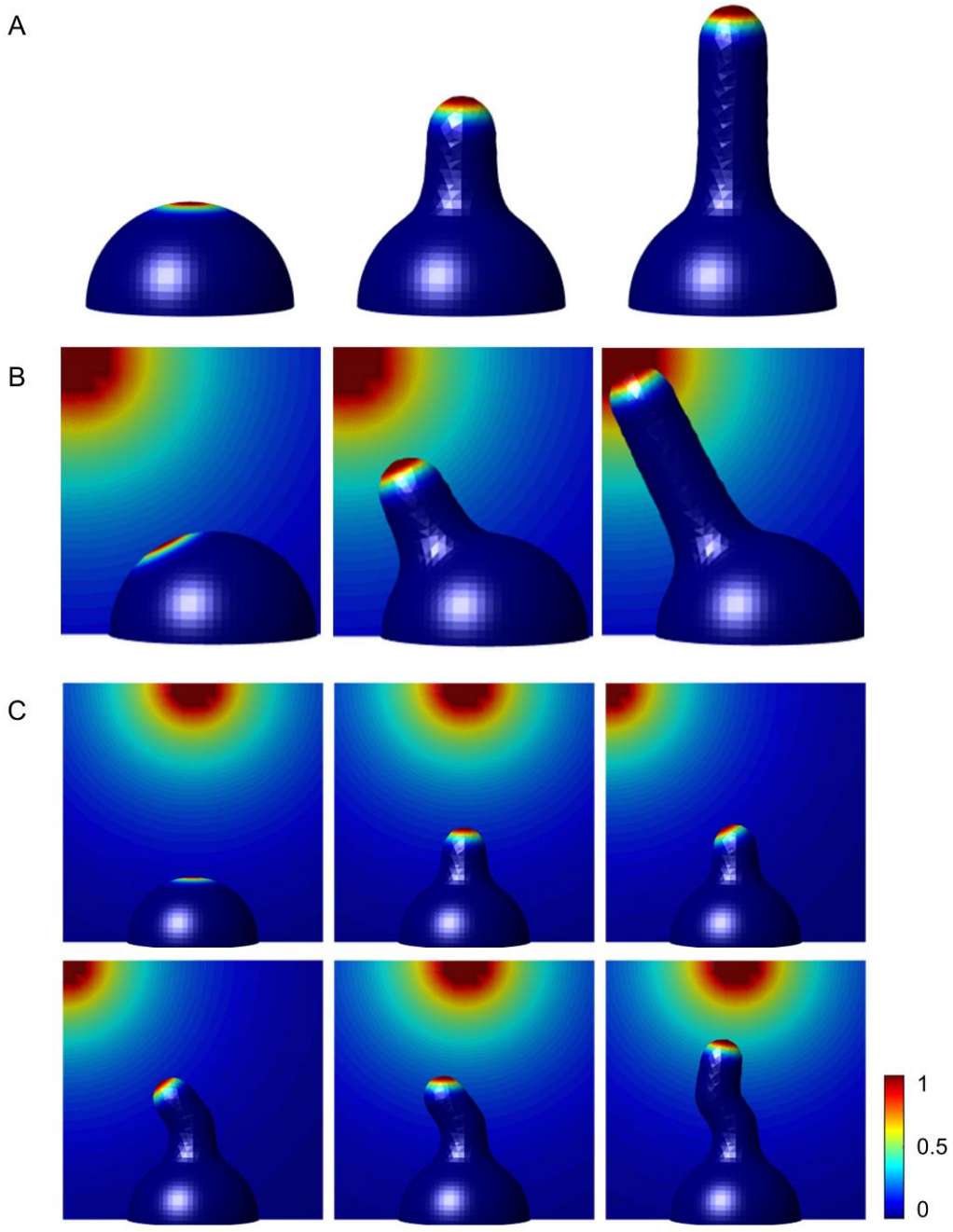
A
B
C
1
0.5
0

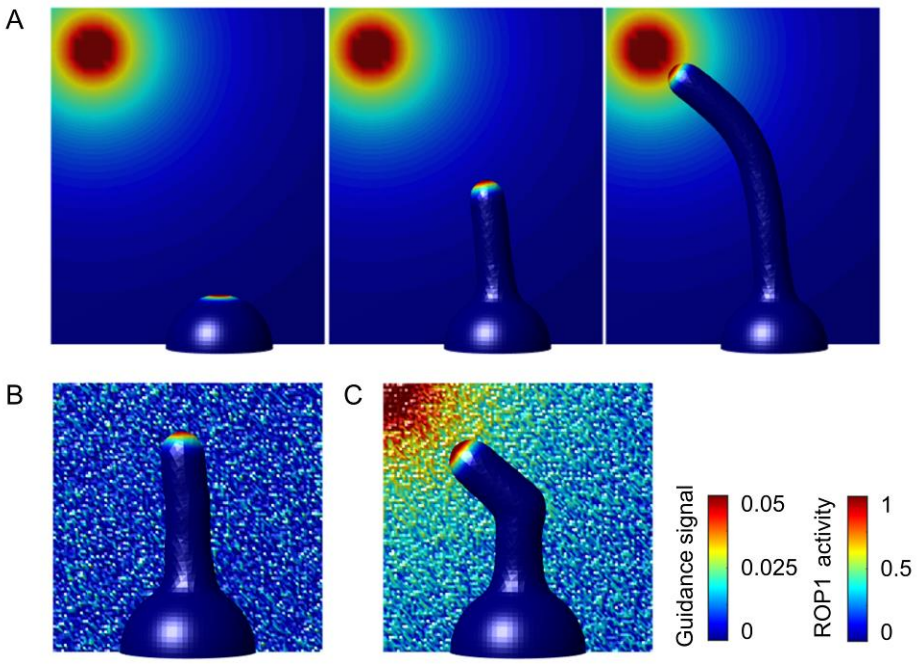

Figure 2-6. The simulated pollen tube is sensitive to guidance signal and robust against noises.
(A) Simulated pollen tube efficiently responds to and makes a graduate turning toward a low guidance signal. **(B)** Simulated pollen tube maintains a relatively stable growth direction with environmental noises of guidance signal. **(C)** Simulated pollen tube is highly sensitive to guidance signal gradient despite the high level of noise. Color in the background shows the concentration of the guidance signal. Color on the surface of the pollen tube shows the concentration of active ROP1.

Figure 2-7. Roles of different factors in pollen tube guidance.
The simulated pollen tubes initially germinate and grow in the absence of the guidance signal. When they reached the same length, they were exposed to a guidance signal gradient. **(A)** Concentration of guidance signal at the source (S_0), **(B)** positive feedback rate of ROP1 (k_{pf0}) and **(C)** coefficient linking ROP1 activity to cell wall extensibility (Φ_0) were altered to compare the behavior of pollen tubes. Upper panels show the morphology of pollen tubes during turning. Color in the background shows the concentration of the guidance signal. Color on the surface of the pollen tube shows the concentration of active ROP1. Lower panels show the dynamics of ROP1. Color shows the concentration of active ROP1.

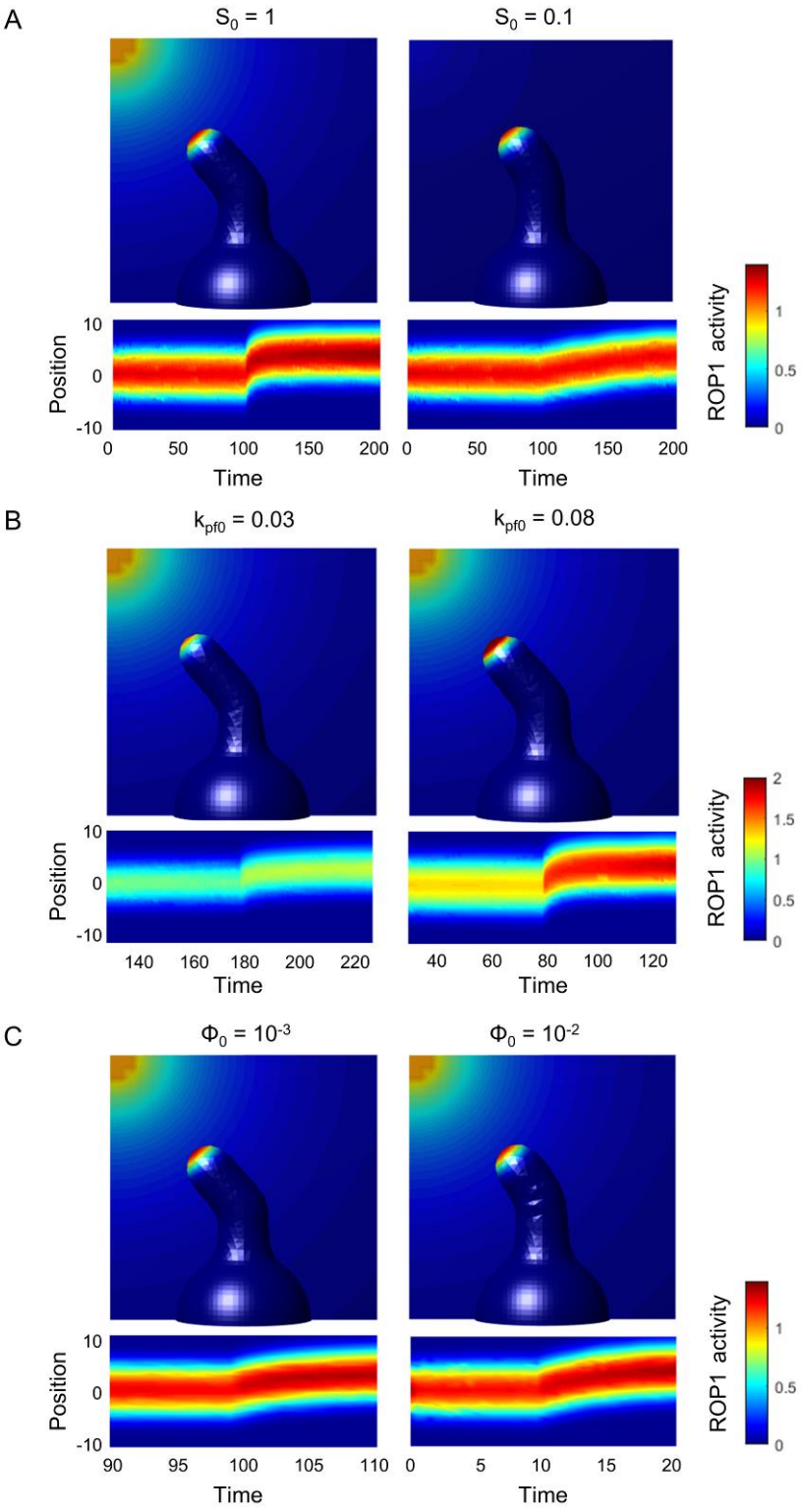
A
S_0 = 1
S_0 = 0.1
Position
10
0
-10
0
50
100
150
200
Time
ROP1 activity
1
0.5
0
B
k_{pf0} = 0.03
k_{pf0} = 0.08
140
160
180
200
220
40
60
80
100
120
2
1.5
C
$\Phi_0 = 10^{-3}$
$\Phi_0 = 10^{-2}$
90
95
100
105
110
5
10
15
20

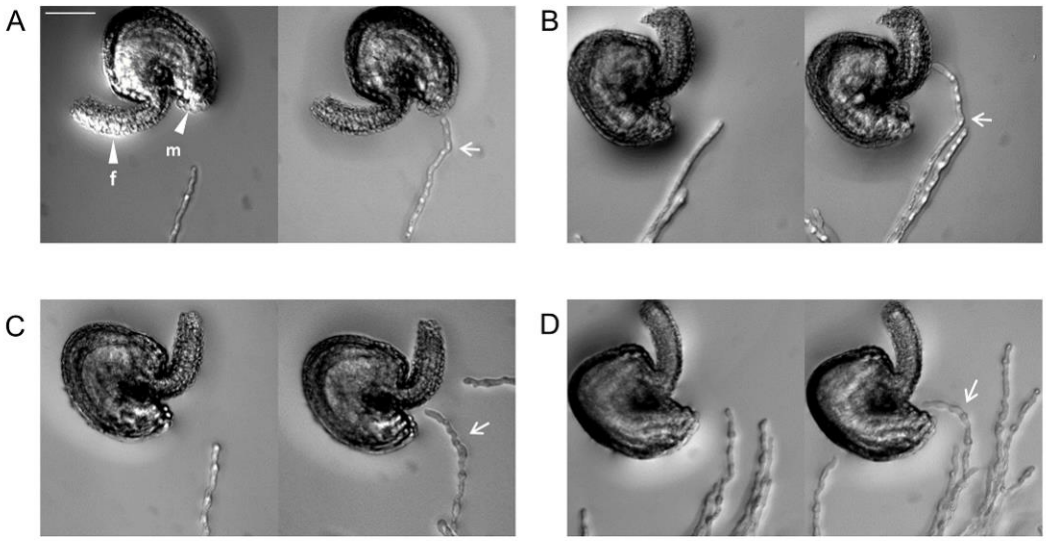

Figure 2-8. The cell morphology during the turnings of pollen tubes in semi-in vitro assay.
Arabidopsis pollen tubes make turnings towards ovules in the semi-in vitro assay. Both **(A, B)** sharp and **(C, D)** smooth turnings were observed. Arrowhead "f" indicates the funiculus and "m" indicates the micropyle of the ovule. Arrows indicate the turning points of the pollen tubes. Scale bar: 50 μm.

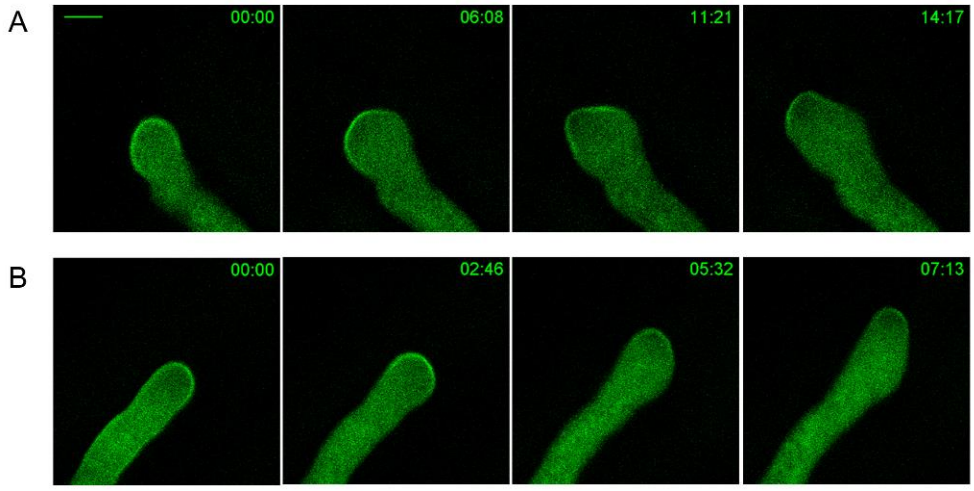

Figure 2-9. The dynamic distribution of active ROP1 during the turnings of pollen tubes.
Confocal images of Arabidopsis pollen tubes expressing CRIB4-GFP. The ovules were placed to the left of the pollen tube tip. Numbers show time (min:sec). Scale bars, 5 μm.

Table 2-1. Parameter setting for the model of pollen tube guidance

Constants	Definition	Value
S_0	Concentration of the guidance signal at the signal source	1
D_S	Diffusion coefficient of the guidance signal on the medium	10 $\mu m^2/s$
k_S	Degradation rate of the guidance signal	0.1 /s
k_{pf0}	Coefficient linking positive feedback rate to the concentration of guidance signal	0.03 /s
k_{nf}	Rate of exocytosis-mediated negative feedback	0.5 /s
R_{total}	Total ROP1 (including active and inactive ROP1)	100
α	Coefficient representing the degree of nonlinearity in the positive feedback	1.25
R_{max}	Maximum active ROP1 concentration in the PM	5
D	Diffusion coefficient of ROP1 in the PM	0.5 $\mu m^2/s$
Φ_0	Coefficient linking active ROP1 to cell wall extensibility	10^{-3}/(MPa·s)
ν	The Poisson's ratio	0.5
p	Turgor pressure	0.2 MPa
h	Thickness of the cell wall	0.2 μm

Chapter 3 Measuring Exocytosis Rate Using Corrected Fluorescence Recovery After Photoconversion

Abstract

Exocytosis plays crucial roles in regulating the distribution and functions of plasma membrane and extracellular matrix proteins. However, measuring the exocytosis rate of a specific protein by conventional methods is very difficult due to exocytosis-independent trafficking such as endocytosis, which also affects membrane protein distribution. Here we describe a novel method, corrected Fluorescence Recovery after Photoconversion, in which exocytosis-dependent and independent trafficking events are measured simultaneously to accurately determine exocytosis rate. In this method, the protein-of-interest is tagged with Dendra2, a green-to-red photoconvertible fluorescent protein. Following the photoconversion of plasma membrane-localized Dendra2, both the recovery of the green signal and the changes in the photoconverted red signal are measured, and the rate of exocytosis is calculated from the changing rates of these two signals.

Introduction

Exocytosis participates in a wide range of cellular processes such as cell growth, polarization and morphogenesis by targeting proteins to the plasma membrane (PM) and the extracellular matrix. The precise temporal and spatial regulation of exocytosis is critical for the localization and function of the cargo proteins. To visualize and measure exocytosis, a variety of methods have been developed, such as labeling exocytic vesicles using fluorescent dyes or marker proteins, monitoring the accumulation of vesicle cargo proteins

on the cell surface and various advanced microscopy techniques including DIC (Differential Interference Contrast), TIRF (Total Internal Reflection Fluorescence) and STED (Stimulated Emission Depletion) microscopy (Keighron et al., 2012; Allersma et al., 2004; Willig et al., 2006; Betz and Bewick, 1992; Zonia and Munnik, 2008), However, these methods are either not suitable for measuring the exocytosis of a specific membrane protein or rapid exocytosis of a large population of vesicles, and they require specific equipment and techniques that are often not accessible. Furthermore, the results obtained by measuring the amount of secreted proteins on the cell surface may be inaccurate due to the interference of exocytosis-independent trafficking processes such as endocytosis.

Pollen tubes elongate rapidly by tip growth, which relies on rapid exocytosis of a large population of vesicles to the apical region of the cells (Cheung and Wu, 2008; Bove et al., 2008; Parton et al., 2001), and thus provides a favorite system for the study of exocytosis. Most previous studies to visualize exocytosis in pollen tubes monitor the secretion of cargo molecules, including FM dyes, cell wall material, fluorescently labeled PM or cell wall proteins such as pectin methylesterase (PME) (McKenna et al., 2009; Zonia and Munnik, 2008; Bosch et al., 2005; Coelho and Malho, 2006; Camacho and Malho, 2003). These methods could conveniently reveal the distribution and dynamics of exocytosis, but lack quantitative power. A Fluorescence Recovery After Photobleaching (FRAP)-based method was developed to quantify exocytosis in pollen tubes (Lee et al., 2008; Bove et al., 2008; Yan and Yang, 2012; Moscatelli et al., 2012). FRAP is a commonly used technique to quantify protein movement, especially the lateral diffusion of membrane proteins (Axelrod

et al., 1976; Day et al., 2012): After photobleaching the fluorescently labeled protein-of-interest in a specific region of the PM (Region of interest, ROI), the fluorescent signal in the ROI recovers with time due to the movement of unbleached protein from the surrounding area. The time course of the recovery is used to compute the rate of movement (Day et al., 2012; Carnell et al., 2015). If the labeled molecule is targeted to the PM or the extracellular matrix by exocytosis, fluorescence intensity in the ROI recovers mainly due to the incorporation of the unbleached protein from the cytoplasm via exocytosis, and therefore, the rate of recovery represents the rate of exocytosis. However, this method failed to consider the internalization of the recovered fluorescent signal on the PM back to the cytoplasm via endocytosis. In addition, in growing cells the dilution caused by the insertion of nascent cell membrane will also reduce the fluorescent intensity in the ROI. Therefore, in conventional FRAP experiments, the observed fluorescence recovery rate may underestimate the actual rate of exocytosis.

Here we describe a FRAP-based novel method, **c**orrected **F**luorescence **R**ecovery **a**fter **P**hoto**c**onversion (cFRAPc), which is performed on an ordinary confocal laser scanning microscope, to measure rapid exocytosis of specific protein-of-interest. In this method, exocytosis-dependent and independent trafficking events are measured simultaneously, so the exocytosis rate can be accurately determined.

In cFRAPc, the protein-of-interest that is targeted to the PM via exocytosis is tagged with Dendra2, a green-to-red photoconvertible variant of GFP (Chudakov et al., 2007). Before

photoconversion, all of the Dendra2-tagged molecules in the cell emit green fluorescence when irradiated with a 488 nm laser. When a ROI on the PM is irradiated with a UV laser, the green fluorescence is irreversibly converted to red fluorescence. The red signal reduces with time due to endocytosis or dilution, which together are referred to as signal reduction factors from here onwards (Figure 3-1). The red signal will not be increased by exocytosis, since the concentration of red Dendra2 in the cytoplasmic pool remains nearly zero. Therefore, the fluorescent intensity of the ROI in the red channel serves as a real-time measurement of the rate of signal reduction on the PM. On the other hand, the green signal in the ROI is affected by two processes: Exocytosis that targets the unconverted green Dendra2 from the cytoplasm to the PM and the simultaneous reduction of the green Dendra2 on the PM due to the signal reduction factors (Figure 3-1). Since the rate of the latter is measured by the reduction of the red signal, the rate of exocytosis can be computed based on the time course of the green signal.

In this chapter, we describe the full procedure of the preparation, imaging and data analysis of cFRAPc experiments. To demonstrate and validate our method, we performed cFRAPc to measure the exocytosis rate of a transmembrane receptor-like kinase expressed in *Arabidopsis thaliana* pollen tubes, PRK1 (AT5G35390), which shows a strong PM signal and preferentially localizes to the tip of pollen tubes (Lee et al., 2008). The comparison of cFRAPc with other methods as well as its applications and limitations are discussed.

Results and Discussion

Experimental preparation

To prepare for the experiments, a construct encoding the protein-of-interest fused to Dendra2 needs to be introduced into cells or organisms of choice. The protein-of-interest can be a PM protein or an extracellular matrix protein. If the research is focused on the general level of exocytosis instead of a particular protein, constitutive PM proteins containing the PM-anchoring domains only could be considered. In this study, to measure the exocytosis rate of PRK1 in *Arabidopsis* pollen tubes, a construct with a pollen tube specific promoter, LAT52, and PRK1 fused with Dendra2 at the C terminus was transformed into *Arabidopsis*.

cFRAPc measures a relative rather than an absolute rate of exocytosis, therefore at least two parallel experiments should be performed for comparison. For example, to study exocytosis in different genetic backgrounds, the construct encoding the Dendra2-tagged protein needs to be introduced into both wild-type and mutant cells. In this study, to investigate the effects of drugs on exocytosis, pollen tubes treated with mock solutions were included as the control group; to analyze the spatial distribution of exocytosis in pollen tubes, results of cFRAPc performed on different regions of the PM were compared.

cFRAPc imaging

Arabidopsis pollen tubes expressing PRK1-Dendra2 construct were cultured on solid pollen tube medium for cFRAPc imaging using a confocal laser-scanning microscope. The

imaging involves three steps: (1) taking a pre-conversion image of a selected cell, (2) photoconverting PRK1-Dendra2 in a selected region on the PM and (3) taking post-conversion time-lapse images of this cell. The pre- and post-conversion images should be taken in both green and red channels, and the imaging settings of each channel should be kept the same throughout the experiment. The green state Dendra2 was excited by a 488 nm laser and detected with the commonly used GFP settings. Photoconversion of Dendra2 is efficiently induced by 405 nm UV light. Pilot experiments were performed to optimize the laser intensity and the scanning time to achieve maximum conversion without photo-toxicity or bleaching of the red signal. The photoconverted red Dendra2 was scanned by a 543 nm laser and detected at 550-670nm. The green and the red signals were detected separately using the sequential scanning mode to avoid crosstalk between these two channels. After photoconverting PRK1-Dendra2 at the pollen tube tip, the green signal recovered and the red signal reduced rapidly, indicating active exocytosis and endocytosis in this region (Figure 3-1).

To evaluate the possible photo-toxicity of UV in cFRAPc experiments, we observed 30 pollen tubes before and after UV irradiation using the same settings as in cFRAPc imaging. The growth rate and the cell width of pollen tubes reduced slightly after UV irradiation, but the difference is insignificant (Figure 3-2A, B). There is no observable change in the morphology of the cells (Figure 3-2C).

Factors that may bias the results of cFRAPc include lateral diffusion and photobleaching. Previous study showed that the lateral diffusion of membrane proteins in *Arabidopsis* pollen tubes was negligible (Lee et al., 2008). To evaluate the level of photobleaching, cFRAPc imaging with the same settings was performed on entire ungerminated pollen grains (Figure 3-3A). Based on the average time-courses of the fluorescent signal, the photobleaching rates in the green and the red channels were estimated to be 0.13% and 0.00% per second, respectively (Figure 3-3B). The signal loss due to photobleaching is added to the measured fluorescent signal when analyzing the cFRAPc data.

Image processing and quantification

The cFRAPc images were analyzed using ImageJ to obtain the data for calculation. Before being measured, images were enhanced using ImageJ processing functions including smoothing and background subtraction. For every frame in the image series, the average fluorescent intensity in the photoconverted PM region was measured to obtain the time courses of both the green and the red signals (Figure 3-4). According to the rationale of the calculations discussed below, the area of the photoconverted region and the average cytoplasmic green signal intensity were also measured.

Calculation of exocytosis rate

In exocytosis, proteins are transported from exocytic vesicles in the cytoplasm to the PM. The amount of protein (denoted by ΔP) being exocytosed to a certain region of the PM with an area of S during time period Δt is given by

$$\Delta P = N P_v S \Delta t, \quad [1]$$

where N is the number of vesicles fusing with the PM per unit area per unit time and P_v is the amount of protein carried by each vesicle. Here only N is dependent on the rate of exocytosis, therefore, we define the absolute rate of exocytosis as

$$R_{abs} = N, \quad [2]$$

or: the rate of exocytosis is the number of exocytic vesicles fusing with the PM per unit area per unit time. According to Equation [1],

$$R_{abs} = \Delta P/(P_v S \Delta t). \quad [3]$$

However, it is difficult to obtain the absolute rate of exocytosis, since we are not able to directly measure P_v, the protein amount in a single vesicle. Instead, since P_v is proportional to $\overline{P}_c$, which is the average concentration of this protein in the cytoplasm, we define the relative rate of exocytosis as

$$R_{ex} = \Delta P/(\overline{P}_c S \Delta t). \quad [4]$$

On the other hand, the amount of protein is proportional to the intensity of fluorescence (Furtado and Henry, 2002; Lorenzen and Kennedy, 1993). Therefore,

$$R_{ex} = \Delta g/(\overline{g}_{cyt} S \Delta t), \quad [5]$$

where Δg is the increase of total green fluorescence in the photoconverted region on the PM and $\overline{g}_{cyt}$ is the average green fluorescence of the cytoplasm.

The red signal of photoconverted Dendra2 on the PM decreases due to endocytosis and the dilution effect caused by membrane insertion. In all these processes the amount of reduced

fluorescence on the PM is proportional to the average fluorescence on the PM, so the rate of signal reduction, R_{red}, can be expressed by an equation similar with Equation [5]:

$$R_{red} = \Delta r/(\bar{r}_{mem} S \Delta t), \quad [6]$$

where Δr and $\bar{r}_{mem}$ are the reduction of total red fluorescence and the average red fluorescence in the photoconverted region on the PM. Therefore, we can calculate the signal reduction rate directly from the decreasing rate of the red signal. Note that the recycling of red Dendra2 back to the PM by exocytosis is negligible since the cytoplasm provides a much larger pool than the small area of PM photoconverted by UV, and the red signal in the cytoplasm remains nearly 0. In actual experiments, we measure the total red signal in the photoconverted area, r, and plot it against time. $\Delta r/\Delta t$ of a given time point is the slope of this curve at this time point (Figure 3-4). $\bar{r}_{mem}$ and S can be measured, so by Equation [6], we can obtain $R_{red}(t)$.

The green signal in the photoconverted area on the PM, however, is affected by both exocytosis and the signal reduction factors. The exocytosed amount minus the reduced amount represents the net increase of the protein on the PM. If we denote the increase of total green fluorescence due to exocytosis as Δg_{ex}, the decrease of total green fluorescence due to the signal reduction factors as Δg_{red}, and the net increase of total green fluorescence as Δg, we have

$$\Delta g = \Delta g_{ex} - \Delta g_{red}. \quad [7]$$

Equation [6] can be translated to the green channel and we have

$$R_{red} = \Delta g_{red}/(\bar{g}_{mem} S \Delta t),$$

or

$$\Delta g_{red} = R_{red}\bar{g}_{mem}S\Delta t. \quad [8]$$

According to Equation [5], the relative exocytosis rate, R_{ex}, is given by

$$R_{ex} = \Delta g_{ex}/(\bar{g}_{cyt}S\Delta t),$$

So we have

$$\Delta g_{ex} = R_{ex}\bar{g}_{cyt}S\Delta t. \quad [9]$$

Substitute [8] and [9] into [7], we have

$$\Delta g = R_{ex}\bar{g}_{cyt}S\Delta t - R_{red}\bar{g}_{mem}S\Delta t,$$

or

$$R_{ex} = [\Delta g/(S\Delta t) + R_{red}\bar{g}_{mem}] / \bar{g}_{cyt}. \quad [10]$$

Again, we can plot the total green signal in the photoconverted area, g, against time. The slope of this curve at time point t gives $\Delta g/\Delta t$ (Figure 3-4). $\bar{g}_{mem}$, $\bar{g}_{cyt}$ and S can be measured. Substitute $R_{red}(t)$ into Equation [10], we obtain $R_{ex}(t)$.

In conventional FRAP method, the signal reduction factors are not considered, therefore R_{red} in Equation [10] is ignored. For the same dataset obtained using PRK1-Dendra2 pollen tubes, we calculated the average exocytosis rates using cFRAPc method and the conventional FRAP method. As expected, the conventional FRAP method significantly underestimated the rate of exocytosis (Figure 3-5).

To validate our method, we first measured the exocytosis rate of pollen tubes treated with chemicals that disrupt exocytosis including Brefeldin A (BFA) and Latrunculin B (LatB)

(Figure 3-6). If calculated by the conventional FRAP method, the exocytosis rates of cells treated with drugs are negative (Figure 3-7). The results obtained by the cFRAPc method, however, suggest that treatment by 2 ng/ml BFA for 45 min or 5 nM LatB for 45 min significantly reduced the exocytosis rate in pollen tubes to 11% and 20% of that in DMSO-treated cells, respectively (Figure 3-7).

We then used this method to study the spatial distribution of exocytosis on the PM of pollen tubes. Results show that exocytosis at the extreme apex of pollen tubes is much more active than at the subapical region (Figure 3-8), agreeing with the reported apically-focused localization of exocytic machinery, the maximum cell wall thickness and strain rates at the tip, and the apical accumulation of PME in various pollen tubes (McKenna et al., 2009; Rojas et al., 2011; Bosch et al., 2005; Hala et al., 2008).

However, the results are in conflict with several previous reports. By pulse-chase labeling with FM dyes and DIC microscopy, Zonia and Munnik (2008) reported exocytic vesicle fusion events at the subapical region of pollen tubes, where the vesicles were relatively sparse (Zonia and Munnik, 2008). They also observed massive exocytic vesicles accumulated at the apex of pollen tubes. However it is unclear whether the dynamic events observed by DIC microscopy indeed reflected exocytic activities, because this light microscopy technique is unable to resolve the high density and small size of vesicles in the extreme apex. Bove and Vaillancourt et al., (2008) also proposed that exocytosis is located at the sub-apex, based on the results of FRAP analysis with FM dye-stained pollen tubes

(Bove et al., 2008). As discussed in our current work, active endocytosis and rapid cell membrane extension at the tip of pollen tubes may obscure the fluorescence recovery resulting from exocytosis. The rapid reduction of the red signal of photoconverted Dendra2 in cFRAPc experiments showed that this is indeed the case. Therefore, the results obtained by conventional FRAP may not be accurate.

Previous studies suggest that elevated membrane trafficking at the tip of pollen tubes is associated with higher growth rate and growth reorientation (Bove et al., 2008; Parton et al., 2001; Coelho and Malho, 2006). We plotted the exocytosis rate measured by cFRAPc versus the growth rate at the corresponding time points. Linear regression indicates that there is a positive correlation between the rate of exocytosis and growth, consistent with the role of exocytosis in delivering cell membrane and wall materials to the growing tip (Figure 3-9). However, the correlation is relatively weak, possibly resulting from roles of other factors in the regulation of pollen tube growth such as endocytosis that internalizes the secreted materials, and the time lag between the deposition and the expansion of cell wall.

Comparison with other methods

Other conventional methods for the quantification of exocytosis include electrophysiological approaches such as capacitance measurement and amperometric measurement, and optical approaches involving advanced microscopy techniques

(Keighron et al., 2012; Allersma et al., 2004; Willig et al., 2006; Thorn, 2012; Steyer et al., 1997).

Fusion of exocytic vesicles to the PM results in a stepwise increase of cell surface area, which is proportional to cell capacitance. Measurement of cell membrane capacitance using the patch-clamp technique can therefore be used to monitor vesicle fusion events (Penner and Neher, 1989; Fernandez et al., 1984). However, since the cell surface area is affected by endocytosis as well, the exocytosis rate measured by this method is biased. Additional bias could result from changes in capacitance independent of changes in the cell surface area. Another method, amperometry, detects the vesicle contents secreted to the medium using microelectrodes, but the major limitation of this method is that it requires the exocytosed substance to be electrochemically active and does not work for membrane proteins that are not discharged into the extracellular space (Albillos et al., 1997; Leszczyszyn et al., 1990; Wightman et al., 1991). These electrophysiological methods have high temporal resolution, but lack spatial information of exocytosis and are not suitable to measure the exocytosis of a specific membrane protein.

One category of optical techniques for studying exocytosis relies on the visualization of exocytic vesicles. Differential Interference Contrast (DIC) microscopy is suited to observe large secretory vesicles in systems such as acinar cells (Mooney et al., 2014; Campos-Toimil et al., 2000; Chen et al., 2005). But in most cell types, vesicles are too small to be observed by DIC microscopy and have to be labeled by fluorescent styryl dyes such as

FM1-43 (Betz and Bewick, 1992; Zonia and Munnik, 2008; Bove et al., 2008; Moscatelli et al., 2012), or by vesicular proteins with fluorescent tags (Bosch et al., 2005; Szumlanski and Nielsen, 2009). One of the commonly used fluorescent imaging techniques to observe exocytosis is Total Internal Reflection Fluorescence (TIRF) microscopy, which illuminates fluorescently labeled vesicles approaching the PM, and the abrupt disappearance of the vesicles indicates fusion events (Allersma et al., 2004; Steyer et al., 1997; Lang et al., 1997). Stimulated Emission Depletion (STED) microscopy with subdiffraction resolution far beyond that of conventional optical microscopy has recently been used to observe the components and behavior of exocytic vesicles in neuron cells (Willig et al., 2006; Sieber et al., 2007; Westphal et al., 2008). Since single exocytic events can be directly observed, these powerful techniques provide abundant information far beyond exocytosis rate and are used to reveal the molecular mechanisms of exocytosis.

Optical microscopy can also be used to observe the accumulation of cargo molecules from exocytic vesicles on the cell surface. For example, the secretion of fluorescently labeled PME to the cell wall was used to show exocytosis in the tip of pollen tubes (McKenna et al., 2009; Bosch et al., 2005). In pollen tubes, the thickness and the strain rates of cell wall also reflect the level of exocytosis, as it secrets wall material and enzymes that results in cell wall extension (McKenna et al., 2009; Rojas et al., 2011). In particular, a study has developed a method to calculate the number of exocytic events in pollen tubes and root hairs from the increase of cell wall volume and the volume of individual exocytic vesicles, which is measured from transmission electron microscopic (TEM) images (Ketelaar et al.,

2008). The main restriction of this method is that it can only be applied to walled-cells in which the cell wall materials are entirely secreted via exocytosis.

Comparing to methods developed in the previous studies, our method has several key advantages. Firstly, in addition to visualizing the process of exocytosis, our method is capable of accurately quantifying the rate of exocytosis. Very few of studies on exocytosis have developed algorithms to determine exocytosis rate from imaging data. Secondly, the results of other methods may be interfered by cellular activities that counterbalance the effect of exocytosis. For example, marker proteins of exocytic vesicles deposited to the cell surface may be internalized by endocytosis. In contrast, our method simultaneously visualizes these exocytosis-independent processes, thereby greatly improved the accuracy of the measurement. Thirdly, unlike the TIRF or STED-based method, the procedure of cFRAPc does not rely on detecting individual exocytic vesicles, and therefore can be used for measuring rapid exocytosis of a large population of vesicles. Finally, cFRAPc can be used to measure both the overall level of exocytosis in the cell and the exocytosis rate of a specific cell membrane protein or cell wall component.

Applications and limitations

In addition to accurate measurement of exocytosis, cFRAPc can be used to measure the endocytosis rate, if the reduction of the red Dendra2 signal caused by cell growth and lateral diffusion is proved to be negligible, in which case the signal reduction almost solely results from endocytosis. The dynamics of exocytosis and endocytosis measured simultaneously

from the same cell will help understanding how these two counteracting processes are coordinated.

This method could be applied to various cell types with suitable protein-of-interest. However, for cells displaying high lateral diffusion rates of membrane proteins, the results would be unreliable. Pilot experiments are therefore needed to assess the level of lateral diffusion. These can be performed by a cFRAPc experiment upon treatment of cells with membrane trafficking-blocking chemicals (Lee et al., 2008). In general, this method works better in plant cells than in animal cells, since lateral diffusion of PM proteins is more restrained in plant cells due to the presence of a cell wall (Martiniere et al., 2012).

The cFRAP method determines a relative value of exocytosis rate, which is related to the nature of the protein of interest itself; more specifically, the amount of this protein carried by each exocytic vesicle. Therefore, it cannot be used to compare the exocytosis rate of different proteins, but is suitable for studying the exocytosis of one protein at different regions of cell membrane, under different cell culture conditions or in different genetic backgrounds. For example, we used cFRAPc to measure the exocytosis rates of PRK1 in *Arabidopsis* pollen tubes in the presence and absence of drugs such as BFA and LatB to study their effect on exocytosis. However, caution should be taken when one draws conclusions from the exocytosis of one protein to the general level of exocytosis of the cell, since different cargo proteins might be carried by different populations of exocytic vesicles. If cells have mutations or are treated by chemicals that only affect one specific type of

exocytic vesicles, the changes in the overall exocytosis rate under these conditions cannot be represented by the measures obtained from a protein of interest by cFRAPc.

Materials and Methods

Generation of transgenic Arabidopsis plants

The cDNA of PRK1 [At5g35390, named RLK in (Lee et al., 2008)] was subcloned from pLAT52::RLK-GFP described in (Lee et al., 2008), and fused with Dendra2 (Chudakov et al., 2007) at the C terminus. The PRK1-Dendra2 fragment was then subcloned into a binary vector, pCL, which was constructed by inserting the pollen tube specific LAT52 promoter into pCAMBIA1300 using SalI and XbaI restriction sites. pCL::PRK1-Dendra2 was introduced to wild-type *Arabidopsis thaliana* Col-0 plants using Agrobacterium-mediated floral-dip method (Clough and Bent, 1998).

Pollen tube culture preparation

Transgenic *Arabidopsis thaliana* plants were grown at 22 ℃ in growth rooms under a light regime of 16h of light and 8 h of dark. Pollen tubes were germinated on a solid pollen culture medium containing 18% (w/v) sucrose (Sigma-Aldrich), 0.01% (w/v) boric acid (Fisher), 1 mM $CaCl_2$ (Sigma-Aldrich), 1 mM $Ca(NO3)_2$ (Sigma-Aldrich), 1 mM $MgSO_4$ (Sigma-Aldrich), and 0.5% (w/v) agar (Sigma-Aldrich). Pollen tubes were incubated at 28 ℃ for 3 hours before cFRAPc imaging. For drug treatment, BFA (Sigma-Aldrich) or LatB (Sigma-Aldrich) dissolved in DMSO was added to liquid pollen culture medium (same as solid pollen culture medium except without agar) to a final concentration of 2

ng/ml or 5 nM, respectively. The liquid medium with drugs was then added to pollen tubes 45 minutes before imaging.

cFRAPc imaging

cFRAPc imaging was performed on an inverted laser scanning confocal microscope (Leica TCS SP5 DMI6000) equipped with image acquisition software Leica LAS AF. The green form of Dendra2 was excited by a 488 nm Argon laser line with 5% laser power and detected at 500-535nm; the red form was excited by a HeNe 543 nm laser line with 40% laser power and detected at 555-620 nm. Photoconversion of Dendra2 was performed by scanning the region-of-interest with 3% UV laser twice. Post-conversion time-lapse videos were taken immediately after photoconversion, with 5.16 s time interval between frames.

Image quantification

Image quantification was performed using the ImageJ software (version 1.45s). Before quantification, the images were smoothed using the "Smooth" function of ImageJ. The cFRAPc image series acquired by confocal laser scanning microscope are imported into ImageJ and analyzed mostly in the form of "Image Sequence". To measure the average fluorescence intensity on the PM, a segmented line was drawn along the photoconverted PM region. To measure the average fluorescence intensity in the cytoplasm, a polygon was draw to cover most of the cytoplasm.

For each cell, the following quantities were measured: Firstly, the average background green and red signal intensity on the PM ($\bar{g}_{mem0}$, $\bar{r}_{mem0}$) were measured from the first frame of the post-conversion green channel image stack and the pre-conversion red channel image, respectively. Secondly, the length (L) and the average green and red signal intensity ($\bar{g}_{mem}$, $\bar{r}_{mem}$) of the photoconverted regions over time after photoconversion were measured from every frame of the post-conversion image stack. Finally, the average green signal intensity of the cytoplasm ($\bar{g}_{cyt}$) was measured from the first frame of the post-conversion green channel image stack.

Data processing and calculation

For small datasets, the calculation of exocytosis rate was performed in Excel by the following procedure:

- Calculating total GFP (g) and total RFP (r): at each time point, the total GFP and total RFP in the converted region on the PM are given by

$$g = (\bar{g}_{mem} - \bar{g}_{mem0})L$$

$$r = (\bar{r}_{mem} - \bar{r}_{mem0})L,$$

  where L, $\bar{g}_{mem}$ and $\bar{r}_{mem}$ are the corresponding values of each time point.

- Calculating the signal reduction rate at t_0: Plot the total RFP (r) versus time t. Obtain the slope of the curve at t_0, $k_r(t_0)$, by creating a regression line using the data points nearby t_0 in Excel. According to Equation [6],

$$R_{red}(t_0) = -k_r(t_0)/[\bar{r}_{mem}(t_0)L_0].$$

- Calculating exocytosis rate at t_0: Plot the total GFP (g) versus time t. Obtain the slope of the curve at t_0, $k_g(t_0)$, by creating a regression line using the data points nearby t_0 in Excel. According to Equation [10],

$$R_{ex}(t_0) = [k_g(t_0)/L_0 + R_{red}(t_0)\bar{g}_{mem}(t_0)] / \bar{g}_{cyt}.$$

High-throughput calculation for large datasets was performed in MatLab.

Figures

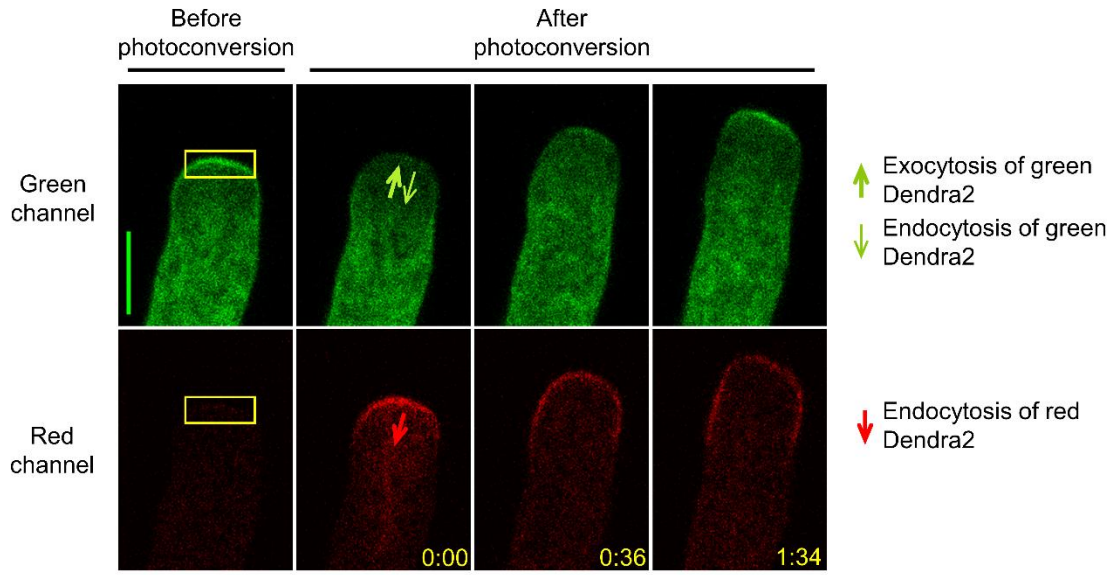

Figure 3-1. cFRAPc imaging of PRK1-Dendra2 in *Arabidopsis* pollen tubes.
Representative confocal images in a typical cFRAPc experiment with *Arabidopsis* pollen tubes expressing PRK1-Dendra2. The apical region of the pollen tube (shown by yellow boxes) is photoconverted from green to red. The arrows indicate the directions of membrane trafficking that affect each signal. Numbers show time after photoconversion (min:sec). Scale bars, 5 μm.

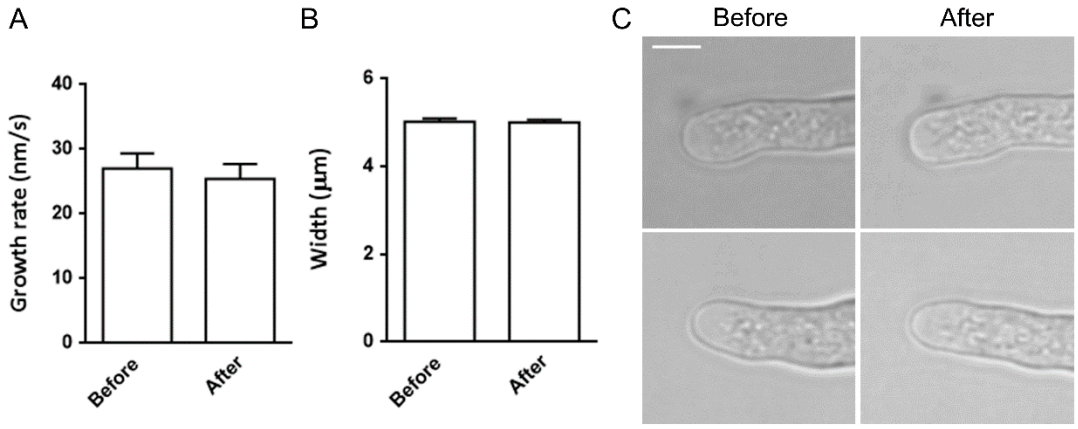

Figure 3-2. Evaluate the side effects of UV irradiation in cFRAPc imaging.
Videos of 30 growing pollen tubes were taken both before and after UV irradiation using the same settings in cFRAPc imaging. **(A)** Average growth rate of pollen tubes before and after UV irradiation. There was no significant difference ($p = 0.2124$, paired Student's t-test). **(B)** Average cell width of pollen tubes before and after UV irradiation. There was no significant difference ($p = 0.7593$, paired Student's t-test). Error bars show S.E.M.. **(C)** There was no evident change in the morphology of pollen tubes before and after UV irradiation. Scale bar, 5 μm.

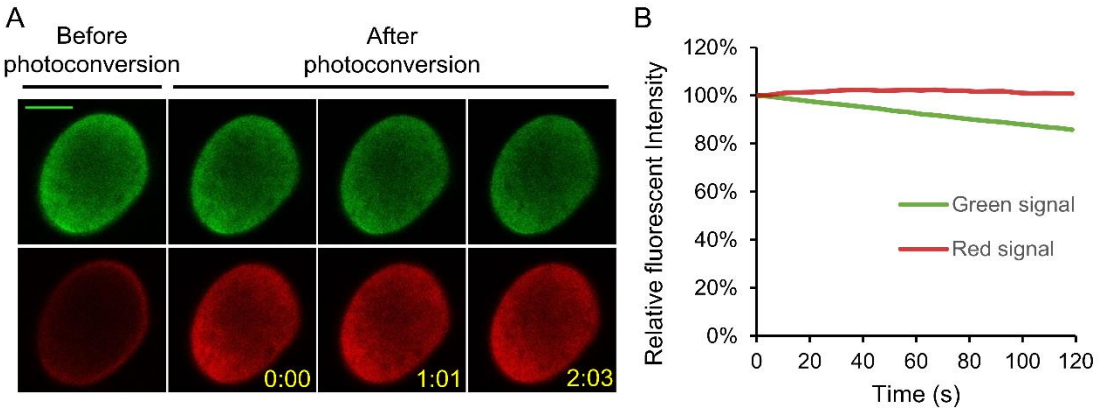

Figure 3-3. Estimating the photobleaching rate in cFRAPc imaging.
(A) Representative pre- and post-photoconversion images of pollen grains. The entire pollen grain was scanned by UV for photoconversion. Numbers show time after photoconversion (min:sec). Scale bars, 10μm. **(B)** The average time-courses of the green and the red signal in cFRAPc imaging conducted with 10 pollen grains to measure the rate of photobleaching. Shown is the percentage of the remaining fluorescent intensity relative to the initial intensity. The curves are fitted by $I(t) = e^{-kt}$, in which I is the fluorescent intensity, t is the time and k is the rate of photobleaching.

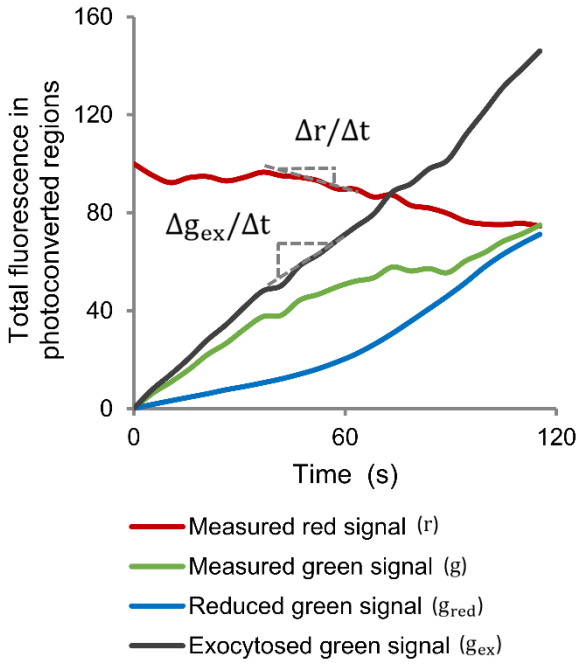

Figure 3-4. Data analysis of cFRAPc images of PRK1-Dendra2 in *Arabidopsis* pollen tubes.

Average time-courses of measured total red or green signal and calculated reduced or exocytosed green signal in the photoconverted regions of 21 cells. As shown in the graph, the changing rate of the total red signal ($\Delta r/\Delta t$) and the exocytosed green signal ($\Delta g_{ex}/\Delta t$) at a certain time point is obtained by calculating the slope of the corresponding curve.

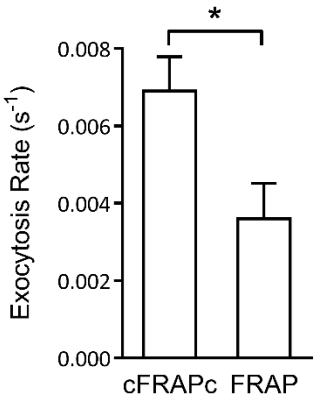

Figure 3-5. Comparison of average exocytosis rates of PRK1-Dendra2 in *Arabidopsis* pollen tubes calculated using cFRAPc method and the conventional FRAP method. Error bars show S.E.M.. * $P \leq 0.05$ (unpaired Student's t-test).

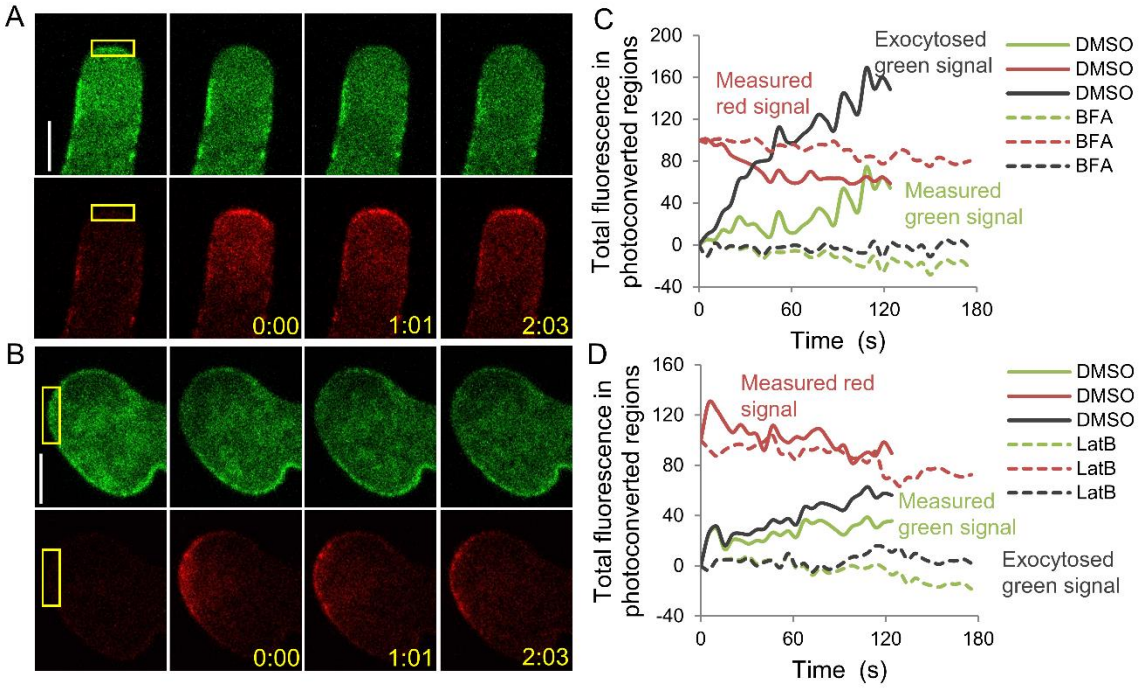

Figure 3-6. cFRAPc imaging of PRK1-Dendra2 in *Arabidopsis* pollen tubes treated with exocytosis-disrupting drugs.

Shown are results of pollen tubes treated with 2 ng/ml BFA for 45 min (A, C) or 5 nM LatB for 45 min (B, D). **(A, B)** Representative cFRAPc images of drug treated pollen tubes (control cells treated with DMSO were not shown). Numbers show time after photoconversion (min:sec). Scale bars, 5 μm. **(C, D)** Time-courses of measured total red signal, measured total green signal and exocytosed total green signal in the photoconverted regions of the representative cells in (A, B).

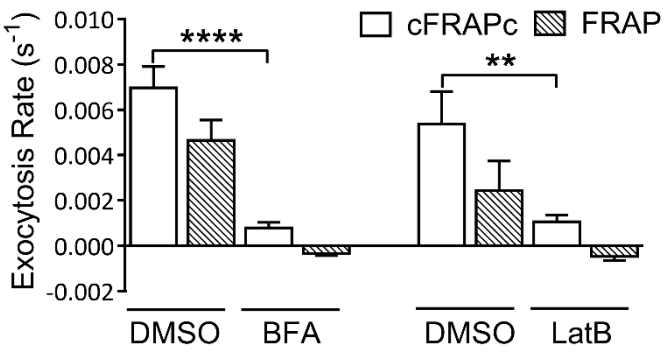

Figure 3-7. Average exocytosis rates of PRK1-Dendra2 in *Arabidopsis* pollen tubes treated with exocytosis-disrupting drugs.
Results obtained by cFRAPc method and the conventional FRAP method are compared. Error bars show S.E.M.. ** $P \leq 0.01$, **** $P \leq 0.0001$ (unpaired Student's t-test).

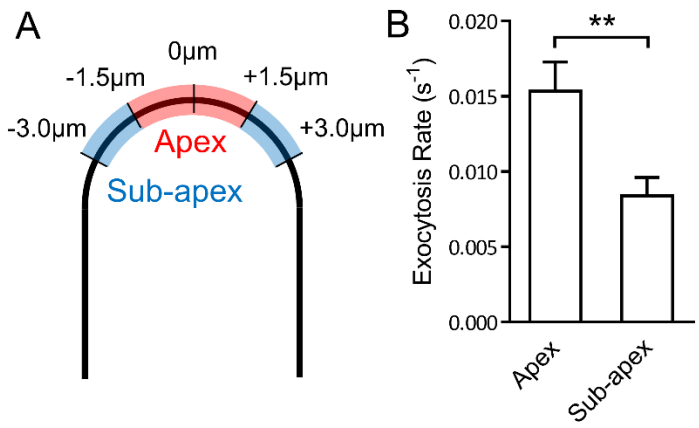

Figure 3-8. Average exocytosis rates of PRK1-Dendra2 at the apex and the sub-apical region of *Arabidopsis* pollen tubes.

(A) A schematic diagram defining of the apex and the sub-apex on the PM of the tip of a pollen tube. Numbers show the distance to the vertex of the pollen tube. **(B)** Average exocytosis rates of PRK1-Dendra2 at the apex and the sub-apex of 12 pollen tubes. ** $P \leq 0.01$ (unpaired Student's t-test).

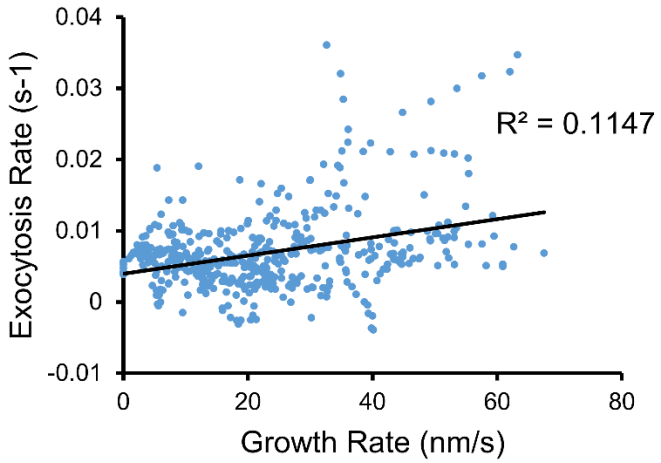

Figure 3-9. Positive correlation between the exocytosis rate and the growth rate of pollen tubes.

The exocytosis rate measured by cFRAPc of 21 wild-type pollen tubes and 23 time points were pooled together and plotted against the corresponding growth rate. Linear regression showed a weak positive correlation between the exocytosis rate and the growth rate of pollen tubes ($y = 0.0001x + 0.004$, $R^2 = 0.1147$).

Conclusions

The tip growth and growth guidance of pollen tubes are controlled by a highly coordinated orchestra of signaling pathways. Previous studies have revealed that ROP1 plays a crucial role in the growth of pollen tubes by regulating the polarity of exocytosis and the mechanical properties of the cell wall. However, how precisely this system works remains elusive due to its complexity. In this work, using combined mathematical modeling and biological experimentation, we addressed the following questions: How is the polarity of ROP1 signaling and exocytosis in pollen tubes established and maintained? How are the paradoxical roles of exocytosis in pollen tube tip growth coordinated? How do the polarity and the growth of pollen tubes response to extracellular signals?

In Chapter 1, we developed a comprehensive mathematical model of pollen tube growth that integrates intracellular signaling and trafficking with the mechanics of cell surface. Exocytosis is at the core of the model: On one hand, by mediating the positive and negative feedback loops of ROP1 activation, exocytosis is important for the polarization of active ROP1, which leads to the polarization of exocytosis itself. On the other hand, through the deposition of pectins and pectin modification enzymes, exocytosis relays the polarity of the intracellular signaling to the composition and properties of the cell wall. This model reproduced the polarized distribution of active ROP1 in the PM and pectins in the cell wall. When turgor pressure is loaded, it reproduced the stable tip growth of pollen tubes.

On the basis of the model for pollen tube tip growth, we developed a model for pollen tube guidance in Chapter 2. By linking the strength of the positive feedback of ROP1 to the concentration of guidance signal, the model reproduced the shifting of cell polarity followed by the redirection of growth in the presence of a signal gradient.

Pollen tubes are highly sensitive to guidance signals so that they can follow a long and precise path to the ovules, while in the absence of guidance signals, they elongate with a relatively steady rate and direction despite the environmental noises. The balance between the stability and the responsiveness of polarity has been captured by our models of pollen tube tip growth and guidance. Without guidance signals, the polarity of ROP1 and exocytosis forms spontaneously and stays at a stable state. In the presence of noises – the fluctuation of guidance signals in the environment, the polarity remains relatively stable. But when a gradient of guidance signal is present, the system responses highly efficiently even to a very shallow gradient.

In order to validate the mathematical models, we compared the predictions of the models with experimental observation. The model for pollen tube tip growth successfully predicted the phenotypes of mutants that are defective in the key links of the system: ROP1 signaling, exocytosis or cell wall composition. In particular, the model predicted that reducing exocytosis to different levels produces opposite effects on the morphology of pollen tubes, reflecting the complex roles of exocytosis in pollen tube growth. This prediction is consistent with the observation of exocytosis-defective mutant and drug-treated pollen

tubes, in which the rate of exocytosis has been accurately measured by Corrected Fluorescence Recovery after Photoconversion, a novel method we presented in Chapter 3. The model for pollen tube guidance, on the other hand, is tested by observing turnings of pollen tubes using the semi-in vitro guidance assay. It is observed that active ROP1 redistributes prior to the change of pollen tube growth direction, as shown by the model. Future experiments are needed to test the other predictions of the model, including the effects of guidance signal strength, growth rate and ROP1 activity on the efficiency of pollen tube guidance.

Our work has shown the value of applying mathematical modeling to studies of cell signaling and growth, and in the future, more mysteries of pollen tube growth will be solved by this approach. Additional pathways and mechanisms, including Calcium signaling, coordination of exocytosis and endocytosis, and oscillation of ROP1 activity, can be integrated into the framework of the current models to provide a more comprehensive understanding of plant cell polarity and morphogenesis.

References

Cole, R. A., Fowler, J. E. (2006). Polarized growth: maintaining focus on the tip. CURR OPIN PLANT BIOL 9**:** 579-588.

Lee, Y. J., Yang, Z. (2008). Tip growth: signaling in the apical dome. CURR OPIN PLANT BIOL 11**:** 662-671.

Lin, Y., Wang, Y., Zhu, J. K., Yang, Z. (1996). Localization of a Rho GTPase Implies a Role in Tip Growth and Movement of the Generative Cell in Pollen Tubes. PLANT CELL 8**:** 293-303.

Gu, Y., Li, S., Lord, E. M., Yang, Z. (2006). Members of a novel class of Arabidopsis Rho guanine nucleotide exchange factors control Rho GTPase-dependent polar growth. PLANT CELL 18**:** 366-381.

Hwang, J. U., Vernoud, V., Szumlanski, A., Nielsen, E., Yang, Z. (2008). A tip-localized RhoGAP controls cell polarity by globally inhibiting Rho GTPase at the cell apex. CURR BIOL 18**:** 1907-1916.

Wu, G., Gu, Y., Li, S., Yang, Z. (2001). A genome-wide analysis of Arabidopsis Rop-interactive CRIB motif-containing proteins that act as Rop GTPase targets. PLANT CELL 13**:** 2841-2856.

Gu, Y., Fu, Y., Dowd, P., Li, S., Vernoud, V., Gilroy, S., Yang, Z. (2005). A Rho family GTPase controls actin dynamics and tip growth via two counteracting downstream pathways in pollen tubes. J. CELL BIOL 169**:** 127-138.

Fu, Y., Wu, G., Yang, Z. (2001). Rop GTPase-dependent dynamics of tip-localized F-actin controls tip growth in pollen tubes. J. CELL BIOL 152**:** 1019-1032.

Lee, Y. J., Szumlanski, A., Nielsen, E., Yang, Z. (2008). Rho-GTPase-dependent filamentous actin dynamics coordinate vesicle targeting and exocytosis during tip growth. J. CELL BIOL 181**:** 1155-1168.

McKenna, S. T., Kunkel, J. G., Bosch, M., Rounds, C. M., Vidali, L., Winship, L. J., Hepler, P. K. (2009). Exocytosis precedes and predicts the increase in growth in oscillating pollen tubes. PLANT CELL 21**:** 3026-3040.

Rojas, E. R., Hotton, S., Dumais, J. (2011). Chemically mediated mechanical expansion of the pollen tube cell wall. BIOPHYS J. 101**:** 1844-1853.

Huang, W. J., Liu, H. K., McCormick, S., Tang, W. H. (2014). Tomato Pistil Factor STIG1 Promotes in Vivo Pollen Tube Growth by Binding to Phosphatidylinositol 3-Phosphate and the Extracellular Domain of the Pollen Receptor Kinase LePRK2. PLANT CELL.

Chang, F., Gu, Y., Ma, H., Yang, Z. (2012). AtPRK2 Promotes ROP1 Activation via RopGEFs in the Control of Polarized Pollen Tube Growth. MOL PLANT.

Zhang, Y., McCormick, S. (2007). A distinct mechanism regulating a pollen-specific guanine nucleotide exchange factor for the small GTPase Rop in Arabidopsis thaliana. Proc Natl Acad Sci U S A 104**:** 18830-18835.

Tang, W., Kelley, D., Ezcurra, I., Cotter, R., McCormick, S. (2004). LeSTIG1, an extracellular binding partner for the pollen receptor kinases LePRK1 and LePRK2, promotes pollen tube growth in vitro. PLANT J. 39**:** 343-353.

Keighron, J. D., Ewing, A. G., Cans, A. S. (2012). Analytical tools to monitor exocytosis: a focus on new fluorescent probes and methods. ANALYST 137**:** 1755-1763.

Allersma, M. W., Wang, L., Axelrod, D., Holz, R. W. (2004). Visualization of regulated exocytosis with a granule-membrane probe using total internal reflection microscopy. MOL BIOL CELL 15**:** 4658-4668.

Willig, K. I., Rizzoli, S. O., Westphal, V., Jahn, R., Hell, S. W. (2006). STED microscopy reveals that synaptotagmin remains clustered after synaptic vesicle exocytosis. NATURE 440**:** 935-939.

Betz, W. J., Bewick, G. S. (1992). Optical analysis of synaptic vesicle recycling at the frog neuromuscular junction. SCIENCE 255**:** 200-203.

Zonia, L., Munnik, T. (2008). Vesicle trafficking dynamics and visualization of zones of exocytosis and endocytosis in tobacco pollen tubes. J. EXP BOT 59**:** 861-873.

Benkert, R., Obermeyer, G., Bentrup, F. W. (1997). The turgor pressure of growing lily pollen tubes. PROTOPLASMA 198**:** 1-8.

Parre, E., Geitmann, A. (2005). Pectin and the role of the physical properties of the cell wall in pollen tube growth of Solanum chacoense. PLANTA 220**:** 582-592.

Jiang, L., Yang, S. L., Xie, L. F., Puah, C. S., Zhang, X. Q., Yang, W. C., Sundaresan, V., Ye, D. (2005). VANGUARD1 encodes a pectin methylesterase that enhances pollen tube growth in the Arabidopsis style and transmitting tract. PLANT CELL 17**:** 584-596.

Bosch, M., Hepler, P. K. (2005). Pectin methylesterases and pectin dynamics in pollen tubes. PLANT CELL 17**:** 3219-3226.

Fayant, P., Girlanda, O., Chebli, Y., Aubin, C. E., Villemure, I., Geitmann, A. (2010). Finite element model of polar growth in pollen tubes. PLANT CELL 22**:** 2579-2593.

Willats, W. G. T. (2001). Modulation of the Degree and Pattern of Methyl-esterification of Pectic Homogalacturonan in Plant Cell Walls. J. BIOL CHEM 276**:** 19404-19413.

Rockel, N., Wolf, S., Kost, B., Rausch, T., Greiner, S. (2008). Elaborate spatial patterning of cell-wall PME and PMEI at the pollen tube tip involves PMEI endocytosis, and reflects the distribution of esterified and de-esterified pectins. PLANT J. 53**:** 133-143.

Bosch, M., Cheung, A. Y., Hepler, P. K. (2005). Pectin methylesterase, a regulator of pollen tube growth. PLANT PHYSIOL 138**:** 1334-1346.

Nett, J., Andes, D. (2006). Candida albicans biofilm development, modeling a host-pathogen interaction. CURR OPIN MICROBIOL 9**:** 340-345.

Giraldo, M. C., Valent, B. (2013). Filamentous plant pathogen effectors in action. NAT REV MICROBIOL 11**:** 800-814.

Fan, L. M., Wang, Y. F., Wang, H., Wu, W. H. (2001). In vitro Arabidopsis pollen germination and characterization of the inward potassium currents in Arabidopsis pollen grain protoplasts. J. EXP BOT 52**:** 1603-1614.

Li, H., Lin, Y., Heath, R. M., Zhu, M. X., Yang, Z. (1999). Control of pollen tube tip growth by a Rop GTPase-dependent pathway that leads to tip-localized calcium influx. PLANT CELL 11**:** 1731-1742.

Yang, Z. (2008). Cell polarity signaling in Arabidopsis. Annu Rev Cell Dev Biol 24**:** 551-575.

Qin, Y., Yang, Z. (2011). Rapid tip growth: insights from pollen tubes. SEMIN CELL DEV BIOL 22**:** 816-824.

Cheung, A. Y., Wu, H. M. (2008). Structural and signaling networks for the polar cell growth machinery in pollen tubes. ANNU REV PLANT BIOL 59**:** 547-572.

Hepler, P. K., Rounds, C. M., Winship, L. J. (2013). Control of cell wall extensibility during pollen tube growth. MOL PLANT 6**:** 998-1017.

Guan, Y., Guo, J., Li, H., Yang, Z. (2013). Signaling in Pollen Tube Growth: Crosstalk, Feedback, and Missing Links. MOL PLANT 6**:** 1053-1064.

Riquelme, M. (2013). Tip growth in filamentous fungi: a road trip to the apex. ANNU REV MICROBIOL 67**:** 587-609.

Mendrinna, A., Persson, S. (2015). Root hair growth: it's a one way street. F1000Prime Rep 7**:** 23.

Bou, D. F., Geitmann, A. (2011). Actin is Involved in Pollen Tube Tropism Through Redefining the Spatial Targeting of Secretory Vesicles. TRAFFIC 12**:** 1537-1551.

Hwang, J. U., Gu, Y., Lee, Y. J., Yang, Z. (2005). Oscillatory ROP GTPase activation leads the oscillatory polarized growth of pollen tubes. MOL BIOL CELL 16**:** 5385-5399.

Kroeger, J., Geitmann, A. (2012). The pollen tube paradigm revisited. CURR OPIN PLANT BIOL.

Kroeger, J. H., Geitmann, A. (2012). Pollen tube growth: Getting a grip on cell biology through modeling. MECH RES COMMUN 42**:** 32-39.

Kroeger, J. H., Geitmann, A., Grant, M. (2008). Model for calcium dependent oscillatory growth in pollen tubes. J. THEOR BIOL 253**:** 363-374.

Fayant, P., Girlanda, O., Chebli, Y., Aubin, C. E., Villemure, I., Geitmann, A. (2010). Finite element model of polar growth in pollen tubes. PLANT CELL 22**:** 2579-2593.

Dumais, J., Shaw, S. L., Steele, C. R., Long, S. R., Ray, P. M. (2006). An anisotropic-viscoplastic model of plant cell morphogenesis by tip growth. INT J. DEV BIOL 50**:** 209-222.

Abenza, J. F., Couturier, E., Dodgson, J., Dickmann, J., Chessel, A., Dumais, J., Salas, R. E. (2015). Wall mechanics and exocytosis define the shape of growth domains in fission yeast. NAT COMMUN 6**:** 8400.

Layton, A. T., Savage, N. S., Howell, A. S., Carroll, S. Y., Drubin, D. G., Lew, D. J. (2011). Modeling vesicle traffic reveals unexpected consequences for Cdc42p-mediated polarity establishment. CURR BIOL 21**:** 184-194.

Campas, O., Mahadevan, L. (2009). Shape and dynamics of tip-growing cells. CURR BIOL 19**:** 2102-2107.

Rojas, E. R., Hotton, S., Dumais, J. (2011). Chemically mediated mechanical expansion of the pollen tube cell wall. BIOPHYS J. 101**:** 1844-1853.

Hill, A. E., Shachar-Hill, B., Skepper, J. N., Powell, J., Shachar-Hill, Y. (2012). An osmotic model of the growing pollen tube. PLOS ONE 7**:** e36585.

Klahre, U., Becker, C., Schmitt, A. C., Kost, B. (2006). Nt-RhoGDI2 regulates Rac/Rop signaling and polar cell growth in tobacco pollen tubes. PLANT J. 46**:** 1018-1031.

Cherfils, J., Zeghouf, M. (2013). Regulation of small GTPases by GEFs, GAPs, and GDIs. PHYSIOL REV 93**:** 269-309.

Kozubowski, L., Saito, K., Johnson, J. M., Howell, A. S., Zyla, T. R., Lew, D. J. (2008). Symmetry-breaking polarization driven by a Cdc42p GEF-PAK complex. CURR BIOL 18**:** 1719-1726.

Woods, B., Kuo, C. C., Wu, C. F., Zyla, T. R., Lew, D. J. (2015). Polarity establishment requires localized activation of Cdc42. The Journal of Cell Biology 211**:** 19-26.

Wedlich-Soldner, R., Altschuler, S., Wu, L., Li, R. (2003). Spontaneous cell polarization through actomyosin-based delivery of the Cdc42 GTPase. SCIENCE 299**:** 1231-1235.

Yan, A., Xu, G., Yang, Z. B. (2009). Calcium participates in feedback regulation of the oscillating ROP1 Rho GTPase in pollen tubes. Proc Natl Acad Sci U S A 106**:** 22002-22007.

Levchenko, A., Iglesias, P. A. (2002). Models of eukaryotic gradient sensing: application to chemotaxis of amoebae and neutrophils. BIOPHYS J. 82**:** 50-63.

Skupsky, R., Losert, W., Nossal, R. J. (2005). Distinguishing modes of eukaryotic gradient sensing. BIOPHYS J. 89**:** 2806-2823.

Sterling, J. D., Quigley, H. F., Orellana, A., Mohnen, D. (2001). The catalytic site of the pectin biosynthetic enzyme alpha-1,4-galacturonosyltransferase is located in the lumen of the Golgi. PLANT PHYSIOL 127**:** 360-371.

Dumais, J., Shaw, S. L., Steele, C. R., Long, S. R., Ray, P. M. (2006). An anisotropic-viscoplastic model of plant cell morphogenesis by tip growth. INT J. DEV BIOL 50**:** 209-222.

Lockhart, J. A. (1965). An analysis of irreversible plant cell elongation. J. THEOR BIOL 8**:** 264-275.

Mogilner, A., Allard, J., Wollman, R. (2012). Cell polarity: quantitative modeling as a tool in cell biology. SCIENCE 336**:** 175-179.

Marco, E., Wedlich-Soldner, R., Li, R., Altschuler, S. J., Wu, L. F. (2007). Endocytosis optimizes the dynamic localization of membrane proteins that regulate cortical polarity. CELL 129**:** 411-422.

Knox, J. P., Linstead, P. J., King, J., Cooper, C., Roberts, K. (1990). Pectin esterification is spatially regulated both within cell walls and between developing tissues of root apices. PLANTA 181**:** 512-521.

Vandenbosch, K. A., Bradley, D. J., Knox, J. P., Perotto, S., Butcher, G. W., Brewin, N. J. (1989). Common components of the infection thread matrix and the intercellular space identified by immunocytochemical analysis of pea nodules and uninfected roots. EMBO J. 8**:** 335-341.

Dardelle, F., Lehner, A., Ramdani, Y., Bardor, M., Lerouge, P., Driouich, A., Mollet, J. C. (2010). Biochemical and immunocytological characterizations of Arabidopsis pollen tube cell wall. PLANT PHYSIOL 153**:** 1563-1576.

Wilsen, K. L., Hepler, P. K. (2007). Sperm Delivery in Flowering Plants: The Control of Pollen Tube Growth. BIOSCIENCE 57**:** 835-844.

Hala, M., Cole, R., Synek, L., Drdova, E., Pecenkova, T., Nordheim, A., Lamkemeyer, T., Madlung, J., Hochholdinger, F., Fowler, J. E., et al. (2008). An exocyst complex functions in plant cell growth in Arabidopsis and tobacco. PLANT CELL 20**:** 1330-1345.

Savage, N. S., Layton, A. T., Lew, D. J. (2012). Mechanistic mathematical model of polarity in yeast. MOL BIOL CELL 23**:** 1998-2013.

Hwang, J. U., Wu, G., Yan, A., Lee, Y. J., Grierson, C. S., Yang, Z. (2010). Pollen-tube tip growth requires a balance of lateral propagation and global inhibition of Rho-family GTPase activity. J. CELL SCI 123**:** 340-350.

Brewbaker, J. L., Kwack, B. H. (1963). The essential role of calcium ion in pollen germination and pollen tube growth. Amer J Bot 50**:** 859.

Hepler, P. K., Winship, L. J. (2010). Calcium at the cell wall-cytoplast interface. J. INTEGR PLANT BIOL 52**:** 147-160.

Steinhorst, L., Kudla, J. (2012). Calcium - a central regulator of pollen germination and tube growth. Biochim Biophys Acta.

Heilmann, I., Ischebeck, T. (2015). Male functions and malfunctions: the impact of phosphoinositides on pollen development and pollen tube growth. PLANT REPROD.

Moscatelli, A., Idilli, A. I. (2009). Pollen tube growth: a delicate equilibrium between secretory and endocytic pathways. J. INTEGR PLANT BIOL 51**:** 727-739.

Takeuchi, H., Higashiyama, T. (2012). A species-specific cluster of defensin-like genes encodes diffusible pollen tube attractants in Arabidopsis. PLOS BIOL 10**:** e1001449.

Okuda, S., Tsutsui, H., Shiina, K., Sprunck, S., Takeuchi, H., Yui, R., Kasahara, R. D., Hamamura, Y., Mizukami, A., Susaki, D., et al. (2009). Defensin-like polypeptide LUREs are pollen tube attractants secreted from synergid cells. NATURE 458**:** 357-361.

Riquelme, M. (2013). Tip growth in filamentous fungi: a road trip to the apex. ANNU REV MICROBIOL 67**:** 587-609.

Molendijk, A. J., Bischoff, F., Rajendrakumar, C. S., Friml, J., Braun, M., Gilroy, S., Palme, K. (2001). Arabidopsis thaliana Rop GTPases are localized to tips of root hairs and control polar growth. EMBO J. 20**:** 2779-2788.

Jones, M. A., Shen, J. J., Fu, Y., Li, H., Yang, Z., Grierson, C. S. (2002). The Arabidopsis Rop2 GTPase is a positive regulator of both root hair initiation and tip growth. PLANT CELL 14**:** 763-776.

Brand, A. C., Morrison, E., Milne, S., Gonia, S., Gale, C. A., Gow, N. A. (2014). Cdc42 GTPase dynamics control directional growth responses. Proc Natl Acad Sci U S A 111**:** 811-816.

Park, S., Szumlanski, A. L., Gu, F., Guo, F., Nielsen, E. (2011). A role for CSLD3 during cell-wall synthesis in apical plasma membranes of tip-growing root-hair cells. NAT CELL BIOL 13**:** 973-980.

Akkerman, M., Franssen-Verheijen, M. A., Immerzeel, P., Hollander, L. D., Schel, J. H., Emons, A. M. (2012). Texture of cellulose microfibrils of root hair cell walls of Arabidopsis thaliana, Medicago truncatula, and Vicia sativa. J Microsc 247**:** 60-67.

Riquelme, M., Bartnicki-Garcia, S., Gonzalez-Prieto, J. M., Sanchez-Leon, E., Verdin-Ramos, J. A., Beltran-Aguilar, A., Freitag, M. (2007). Spitzenkorper localization and intracellular traffic of green fluorescent protein-labeled CHS-3 and CHS-6 chitin synthases in living hyphae of Neurospora crassa. EUKARYOT CELL 6**:** 1853-1864.

Kopecek, P., Raclavsky, V. (1999). Comparison of chitin content in the apical and distal parts of fungal hyphae in Basidiobolus ranarum, Neurospora crassa and Coprinus sterquilinus. Folia Microbiol (Praha) 44**:** 397-400.

Cosgrove, D. J. (2005). Growth of the plant cell wall. NAT REV MOL CELL BIO 6**:** 850-861.

Clough, S. J., Bent, A. F. (1998). Floral dip: a simplified method for Agrobacterium-mediated transformation of Arabidopsis thaliana. PLANT J. 16**:** 735-743.

Luo, N., Yan, A., Yang, Z. (2016). Measuring Exocytosis Rate Using Corrected Fluorescence Recovery After Photoconversion. TRAFFIC.

Cole, R. A., Synek, L., Zarsky, V., Fowler, J. E. (2005). SEC8, a subunit of the putative Arabidopsis exocyst complex, facilitates pollen germination and competitive pollen tube growth. PLANT PHYSIOL 138**:** 2005-2018.

Hachet-Haas, M., Converset, N., Marchal, O., Matthes, H., Gioria, S., Galzi, J. L., Lecat, S. (2006). FRET and colocalization analyzer--a method to validate measurements of sensitized emission FRET acquired by confocal microscopy and available as an ImageJ Plug-in. Microsc Res Tech 69**:** 941-956.

Chebli, Y., Kaneda, M., Zerzour, R., Geitmann, A. (2012). The cell wall of the Arabidopsis pollen tube--spatial distribution, recycling, and network formation of polysaccharides. PLANT PHYSIOL 160**:** 1940-1955.

Wengier, D., Valsecchi, I., Cabanas, M. L., Tang, W. H., McCormick, S., Muschietti, J. (2003). The receptor kinases LePRK1 and LePRK2 associate in pollen and when expressed in yeast, but dissociate in the presence of style extract. Proc Natl Acad Sci U S A 100**:** 6860-6865.

Guyon, V., Tang, W. H., Monti, M. M., Raiola, A., Lorenzo, G. D., McCormick, S., Taylor, L. P. (2004). Antisense phenotypes reveal a role for SHY, a pollen-specific leucine-rich repeat protein, in pollen tube growth. PLANT J. 39**:** 643-654.

Takeuchi, H., Higashiyama, T. (2016). Tip-localized receptors control pollen tube growth and LURE sensing in Arabidopsis. NATURE 531**:** 245-248.

Wang, T., Liang, L., Xue, Y., Jia, P., Chen, W., Zhang, M., Wang, Y., Li, H., Yang, W. (2016). A receptor heteromer mediates the male perception of female attractants in plants. NATURE 531**:** 241-244.

Onsum, M., Rao, C. V. (2007). A mathematical model for neutrophil gradient sensing and polarization. PLOS COMPUT BIOL 3**:** e36.

Levine, H., Kessler, D. A., Rappel, W. J. (2006). Directional sensing in eukaryotic chemotaxis: a balanced inactivation model. Proc Natl Acad Sci U S A 103**:** 9761-9766.

Narang, A. (2006). Spontaneous polarization in eukaryotic gradient sensing: A mathematical model based on mutual inhibition of frontness and backness pathways. J. THEOR BIOL 240**:** 538-553.

Sakumura, Y., Tsukada, Y., Yamamoto, N., Ishii, S. (2005). A Molecular Model for Axon Guidance Based on Cross Talk between Rho GTPases. BIOPHYS J. 89**:** 812-822.

Skupsky, R., Losert, W., Nossal, R. J. (2005). Distinguishing modes of eukaryotic gradient sensing. BIOPHYS J. 89**:** 2806-2823.

Levchenko, A., Iglesias, P. A. (2002). Models of eukaryotic gradient sensing: application to chemotaxis of amoebae and neutrophils. BIOPHYS J. 82**:** 50-63.

Arrieumerlou, C., Meyer, T. (2005). A local coupling model and compass parameter for eukaryotic chemotaxis. DEV CELL 8**:** 215-227.

Stewman, S. F., Jones-Rhoades, M., Bhimalapuram, P., Tchernookov, M., Preuss, D., Dinner, A. R. (2010). Mechanistic insights from a quantitative analysis of pollen tube guidance. BMC PLANT BIOL 10**:** 32.

Logan, D. (2012). A first course in the finite element method, 5th, (Stamford, CT : Cencage Learning).

Onate, E. (2013). Structural analysis with the finite element method. Volume 2, Beams, plates and shells, (Dordrecht ; London : Springer).

Okuda, S., Higashiyama, T. (2010). Pollen tube guidance by attractant molecules: LUREs. CELL STRUCT FUNCT 35**:** 45-52.

Higashiyama, T., Kuroiwa, H., Kawano, S., Kuroiwa, T. (1998). Guidance in vitro of the pollen tube to the naked embryo sac of torenia fournieri. PLANT CELL 10**:** 2019-2032.

Palanivelu, R., Preuss, D. (2006). Distinct short-range ovule signals attract or repel Arabidopsis thaliana pollen tubes in vitro. BMC PLANT BIOL 6**:** 7.

Bove, J., Vaillancourt, B., Kroeger, J., Hepler, P. K., Wiseman, P. W., Geitmann, A. (2008). Magnitude and Direction of Vesicle Dynamics in Growing Pollen Tubes Using Spatiotemporal Image Correlation Spectroscopy and Fluorescence Recovery after Photobleaching. PLANT PHYSIOL 147**:** 1646-1658.

Parton, R. M., Fischer-Parton, S., Watahiki, M. K., Trewavas, A. J. (2001). Dynamics of the apical vesicle accumulation and the rate of growth are related in individual pollen tubes. J. CELL SCI 114**:** 2685-2695.

Coelho, P. C., Malho, R. (2006). Correlative Analysis of [Ca](C) and Apical Secretion during Pollen Tube Growth and Reorientation. Plant Signal Behav 1**:** 152-157.

Camacho, L., Malho, R. (2003). Endo/exocytosis in the pollen tube apex is differentially regulated by Ca2+ and GTPases. J. EXP BOT 54**:** 83-92.

Yan, A., Yang, Z. (2012). FRAP-based analysis of Rho GTPase-dependent polar exocytosis in pollen tubes. Methods Mol Biol 827**:** 393-401.

Moscatelli, A., Idilli, A. I., Rodighiero, S., Caccianiga, M. (2012). Inhibition of actin polymerisation by low concentration Latrunculin B affects endocytosis and alters exocytosis in shank and tip of tobacco pollen tubes. Plant Biol (Stuttg) 14**:** 770-782.

Axelrod, D., Koppel, D. E., Schlessinger, J., Elson, E., Webb, W. W. (1976). Mobility measurement by analysis of fluorescence photobleaching recovery kinetics. BIOPHYS J. 16**:** 1055-1069.

Day, C. A., Kraft, L. J., Kang, M., Kenworthy, A. K. (2012). Analysis of protein and lipid dynamics using confocal fluorescence recovery after photobleaching (FRAP). Curr Protoc Cytom 2**:** t2-t19.

Carnell, M., Macmillan, A., Whan, R. (2015). Fluorescence recovery after photobleaching (FRAP): acquisition, analysis, and applications. Methods Mol Biol 1232**:** 255-271.

Chudakov, D. M., Lukyanov, S., Lukyanov, K. A. (2007). Using photoactivatable fluorescent protein Dendra2 to track protein movement. BIOTECHNIQUES 42**:** 553, 555, 557.

Furtado, A., Henry, R. (2002). Measurement of green fluorescent protein concentration in single cells by image analysis. ANAL BIOCHEM 310**:** 84-92.

Lorenzen, A., Kennedy, S. W. (1993). A fluorescence-based protein assay for use with a microplate reader. ANAL BIOCHEM 214**:** 346-348.

Thorn, P. (2012). Measuring calcium signals and exocytosis in tissues. Biochim Biophys Acta 1820**:** 1179-1184.

Steyer, J. A., Horstmann, H., Almers, W. (1997). Transport, docking and exocytosis of single secretory granules in live chromaffin cells. NATURE 388**:** 474-478.

Penner, R., Neher, E. (1989). The patch-clamp technique in the study of secretion. TRENDS NEUROSCI 12**:** 159-163.

Fernandez, J. M., Neher, E., Gomperts, B. D. (1984). Capacitance measurements reveal stepwise fusion events in degranulating mast cells. NATURE 312**:** 453-455.

Albillos, A., Dernick, G., Horstmann, H., Almers, W., Alvarez, D. T. G., Lindau, M. (1997). The exocytotic event in chromaffin cells revealed by patch amperometry. NATURE 389**:** 509-512.

Leszczyszyn, D. J., Jankowski, J. A., Viveros, O. H., Diliberto, E. J., Near, J. A., Wightman, R. M. (1990). Nicotinic receptor-mediated catecholamine secretion from individual chromaffin cells. Chemical evidence for exocytosis. J. BIOL CHEM 265**:** 14736-14737.

Wightman, R. M., Jankowski, J. A., Kennedy, R. T., Kawagoe, K. T., Schroeder, T. J., Leszczyszyn, D. J., Near, J. A., Diliberto, E. J., Viveros, O. H. (1991). Temporally resolved catecholamine spikes correspond to single vesicle release from individual chromaffin cells. Proc Natl Acad Sci U S A 88**:** 10754-10758.

Mooney, J., Thakur, S., Kahng, P., Trapani, J. G., Poccia, D. (2014). Quantification of exocytosis kinetics by DIC image analysis of cortical lawns. J Chem Biol 7**:** 43-55.

Campos-Toimil, M., Edwardson, J. M., Thomas, P. (2000). Real-time studies of zymogen granule exocytosis in intact rat pancreatic acinar cells. J Physiol 528 Pt 2**:** 317-326.

Chen, Y., Warner, J. D., Yule, D. I., Giovannucci, D. R. (2005). Spatiotemporal analysis of exocytosis in mouse parotid acinar cells. Am J Physiol Cell Physiol 289**:** C1209-C1219.

Szumlanski, A. L., Nielsen, E. (2009). The Rab GTPase RabA4d regulates pollen tube tip growth in Arabidopsis thaliana. PLANT CELL 21**:** 526-544.

Lang, T., Wacker, I., Steyer, J., Kaether, C., Wunderlich, I., Soldati, T., Gerdes, H. H., Almers, W. (1997). Ca2+-triggered peptide secretion in single cells imaged with green fluorescent protein and evanescent-wave microscopy. NEURON 18**:** 857-863.

Sieber, J. J., Willig, K. I., Kutzner, C., Gerding-Reimers, C., Harke, B., Donnert, G., Rammner, B., Eggeling, C., Hell, S. W., Grubmuller, H., et al. (2007). Anatomy and dynamics of a supramolecular membrane protein cluster. SCIENCE 317**:** 1072-1076.

Westphal, V., Rizzoli, S. O., Lauterbach, M. A., Kamin, D., Jahn, R., Hell, S. W. (2008). Video-rate far-field optical nanoscopy dissects synaptic vesicle movement. SCIENCE 320**:** 246-249.

Ketelaar, T., Galway, M. E., Mulder, B. M., Emons, A. M. (2008). Rates of exocytosis and endocytosis in Arabidopsis root hairs and pollen tubes. J Microsc 231**:** 265-273.

Martiniere, A., Lavagi, I., Nageswaran, G., Rolfe, D. J., Maneta-Peyret, L., Luu, D. T., Botchway, S. W., Webb, S. E., Mongrand, S., Maurel, C., et al. (2012). Cell wall constrains lateral diffusion of plant plasma-membrane proteins. Proc Natl Acad Sci U S A 109**:** 12805-12810.